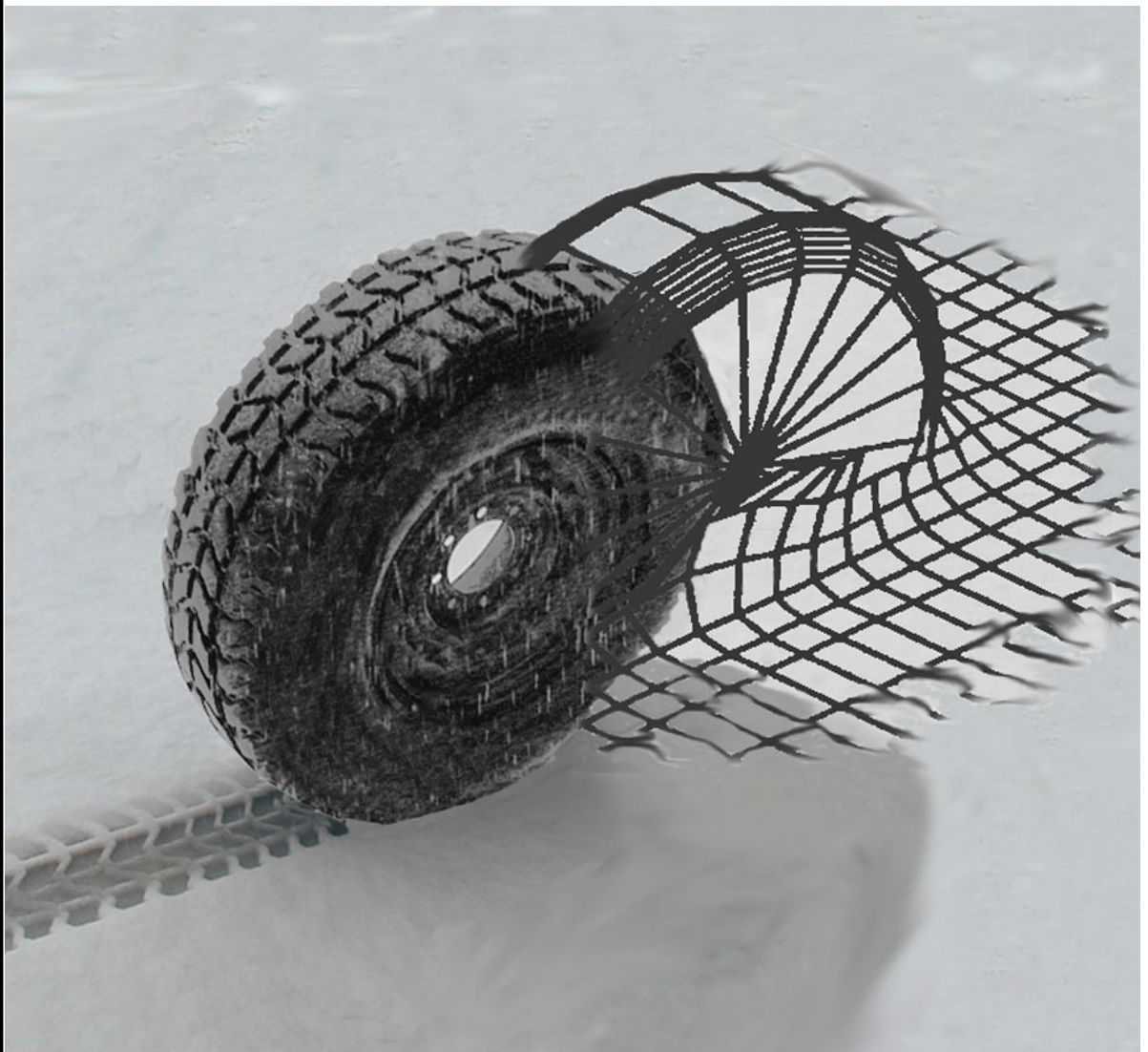


**US Army Corps
of Engineers®**
Engineer Research and
Development Center

Finite Element Modeling of Tire–Terrain Interaction

Sally A. Shoop

November 2001



Abstract: The desire to incorporate theoretical mechanics into off-road vehicle performance prediction has generated great interest in applying numerical modeling techniques to simulate the interaction of the tire and terrain. Therefore, a full three-dimensional model simulating a tire rolling over deformable terrain was developed. Tires were simulated using a rigid wheel, a deformable tire simplified with user-defined sidewall elements, and modal analysis tire models. Model comparisons with measured, hard-surface tire deformation and contact stress showed very good agreement. The simplified tire model was much more computationally efficient but the modal analysis model yielded bet-

ter contact stress distribution. Each of the tire models was then combined with rolling on deformable terrain. Fresh snow and compacted sand surfaces were modeled using critical-state plasticity models. The rigid wheel model was validated on snow using field measurements of tire forces and snow deformation and then compared to performance predictions using the NATO Reference Mobility Model. These comparisons indicate excellent agreement between the model and the measurements. Preliminary results of the modal analysis tire model on snow show very little deformation in the tire, indicating that the rigid wheel simplification may be a good approximation for soft terrain.

How to get copies of ERDC technical publications:

Department of Defense personnel and contractors may order reports through the Defense Technical Information Center:

DTIC-BR SUITE 0944
8725 JOHN J KINGMAN RD
FT BELVOIR VA 22060-6218
Telephone (800) 225-3842
E-mail help@dtic.mil
msorders@dtic.mil
WWW <http://www.dtic.mil/>

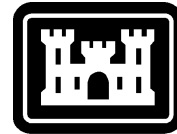
All others may order reports through the National Technical Information Service:

NTIS
5285 PORT ROYAL RD
SPRINGFIELD VA 22161
Telephone (703) 487-4650
(703) 487-4639 (TDD for the hearing-impaired)
E-mail orders@ntis.fedworld.gov
WWW <http://www.ntis.gov/index.html>

For information on all aspects of the Engineer Research and Development Center, visit our World Wide Web site:

<http://www.erdcl.usace.army.mil>

Technical Report
ERDC/CRREL TR-01-16



**US Army Corps
of Engineers®**
Engineer Research and
Development Center

Finite Element Modeling of Tire–Terrain Interaction

Sally A. Shoop

November 2001

Prepared for
OFFICE OF THE CHIEF OF ENGINEERS

Approved for public release; distribution is unlimited.

PREFACE

This report was prepared by Sally A. Shoop, Research Civil Engineer, Applied and Military Engineering Branch, U.S. Army Engineer Research and Development Center (ERDC), Cold Regions Research and Engineering Laboratory (CRREL), Hanover, New Hampshire.

This work was funded by the Office of the Chief of Engineers under work unit *Winter Terrain Effects on Army Simulations*.

The author thanks Ron Liston and George Ashton, CRREL, who provided financial and moral support; Paul Richmond, George Blaisdell, and Byron Young, CRREL, who assisted in gathering, providing, and analyzing experimental data; Robert Haehnel of CRREL and Ken Kestler, independent consultant, who did much of the snow modeling; Ian Darnell, University of Michigan, who helped in generating and debugging the Shoop-Darnell models; Jane Mason, Tom Vaughan, and Peter Keene, CRREL, for assistance with the graphics; and David Cate, Donna Harp, and John Severance for helping with finishing touches on the document. Mike Trinko at Goodyear and Paul Corcoran and Liqun Chi at Caterpillar provided many helpful discussions, and Dr. Roman Hryciw, University of Michigan, provided much encouragement and advice. Technical reviews were provided by Dr. Hryciw, Dr. Gregory Hulbert, and Dr. Kenneth Ludema, University of Michigan.

The contents of this report are not to be used for advertising or promotional purposes. Citation of brand names does not constitute an official endorsement or approval of the use of such commercial products.

CONTENTS

Preface	ii
Nomenclature	vi
Introduction	1
Background	1
Off-road vehicle performance prediction	1
Vehicle movement on snow	2
Tire–terrain modeling	2
Tire terminology	4
Terrain material models	5
General concepts for plasticity models	5
Modified Drucker–Prager cap model	10
Crushable foam model	12
Constitutive models for snow	12
Soil model	22
Tire models for a deformable substrate	24
Tire model construction	24
Evaluation of tire models on a rigid surface	35
Combined tire–terrain model	41
Modeling the tire–terrain contact interface	41
Rigid wheel on snow	42
Deformable tire on soil	51
Deformable tire on snow	54
Conclusions	54
Summary	54
Significant findings	55
Recommended applications and future research needs	56
Literature cited	56

ILLUSTRATIONS

Figure	
1. Sand deformation under a towed wheel moving to the right	2
2. Shallow and deep snow under a wheeled vehicle	2
3. Snow cross sections showing pressure bulb formation	3
4. Two-dimensional modeling of tire–terrain interaction by Aubel (1993)	4
5. Modeling of the effect of lug design on tread–terrain interaction in two dimensions by Fervers (1994)	4
6. Tire direction convention	4
7. Construction components of a radial ply tire	5
8. Measurement of tire dimensions	5
9. Modified Drucker–Prager yield surface in deviatoric space	7
10. Yield surfaces in deviatoric space	7
11. Common yield surfaces along the hydrostatic axis in principal stress space	7
12. Three-dimensional view of critical state yield surface	8
13. Cap contraction or expansion reflecting the softening or hardening of the material	8
14. Exponential hardening law for material in hydrostatic compression	9
15. Piecewise linear modeling of the hardening law	9
16. Isotropic and kinematic hardening	10

Figure

17. Modified Drucker–Prager cap yield surface in the p - t plane	11
18. Modified Drucker–Prager cap flow potential in the p - t plane	11
19. Yield surface for the crushable foam model	12
20. Plastic flow surface for the crushable foam model	12
21. Compilation of Young’s modulus and Poisson’s ratio measurements on snow	13
22. Calculated c' and ϕ' using measurements from the CRREL Instrumented Vehicle and the ring shear device and predicted using the Shallow Snow Model	14
23. Compilation of uniaxial strength data	15
24. Compression of natural snow at 0° to –3°C	16
25. Compression of undisturbed snow and ice	17
26. Pressure–volume data from compression tests of Abele and Gow (1975)	17
27. Comparison of model and experimental data for uniaxial compression tests on low-density snow	18
28. Deformed meshes for field plate sinkage simulations	19
29. Comparison of modeled and measured plate sinkage test for laboratory and field tests	20
30. Modeled snow density of plate sinkage test for Drucker–Prager cap material	21
31. Measured displacement and snow density in laboratory plate sinkage test	21
32. Deformation of fresh snow under a plate	22
33. Grain size curves for McCormick Ranch sand and Lebanon sand	22
34. Validation of McCormick Ranch sand Drucker–Prager cap model with uniaxial strain test data	23
35. National Tire Modeling Program model of a radial tire	24
36. Tires used in experiments	25
37. Deflection measurements for the tires used in the experiments	26
38. Comparison of measured contact area for the three test tire at 241 kPa	27
39. Construction elements of the Darnell tire model	28
40. Cut tire sections used to determine composite tire properties	28
41. Tire geometric parameters for the sidewall model	29
42. Shoop–Darnell tire model	30
43. Modal analysis tire model with smooth tread	32
44. Modal analysis tire model with ribbed tread	33
45. Measured deflection for three tire pressures	35
46. Comparison of measured and modeled deflection for the Shoop–Darnell, smooth tread, and ribbed tread models for three inflation pressures	35
47. Comparison of all measured and modeled deflections at 241 kPa inflation pressure	36
48. Measured contact areas at three inflation pressures	36
49. Comparison of measured and modeled contact areas at three inflation pressures .	37
50. Comparison of Shoop–Darnell model results with measured contact areas	38
51. Comparison of the smooth and ribbed modal analysis tire models with measured contact areas	38
52. Measured and modeled contact stress distribution for half carcass on a hard surface	39
53. Irregular stress contours generated by the Shoop–Darnell model on a rigid surface	39
54. Close-up view of contact for the ribbed tire model	39
55. Measured and modeled sidewall profiles for the Shoop–Darnell tire model	40
56. Model of wheel rolling on 20 cm of fresh snow	43
57. Comparison of standard mesh and ALE mesh	43
58. The CRREL Instrumented Vehicle	44
59. Configuration of speed sensors and axle-mounted load cells on the CIV	44
60. Parameters used to predict motion resistance using the NRMM algorithm	46

Figure

61. Modeled resistance force in coefficient form (longitudinal/vertical) and vertical displacement of the wheel hub in 20-cm snow	47
62. Finite element model, measured data, and NRMM predictions for sinkage and motion resistance in fresh snow	47
63. Finite element simulations at zero slip and at unlimited slip and NRMM motion resistance predictions for 240-kg/m ³ snow	48
64. Marking the snow to observe snow deformation after vehicle passage	49
65. Comparison of measured displacement to modeled displacement and deviatoric stress in the longitudinal direction	50
66. Comparison of measured and modeled displacement in a cross section transverse to the direction of travel	50
67. Comparison of measured and modeled densities in the cross section transverse to the direction of travel	51
68. Rolling tire on an elastic material (sand).	52
69. Rolling Shoop–Darnell tire on a Drucker–Prager cap model of the McCormick Ranch sand	53
70. Deformed mesh of modal analysis tire model in snow after 8 cm of sinkage	54
71. Close-up of a tire after sinking 8 cm into the snow at the beginning of roll	54

TABLES

Table

1. Initial material model parameters	15
2. Pressure–volume data calculated from the Abele and Gow (1975) data set for 200- to 220-kg/m ³ snow at 0° to –3°C	16
3. Hardening table for fresh snow with a density of 200 kg/m ³	18
4. Material constants for Drucker–Prager cap model of McCormick Ranch sand	23
5. Hardening model for McCormick Ranch sand (HKS, 1996)	23
6. Tire characteristics for test tires at an average vertical load of 6227 N	25
7. Bending stiffness of tire sections	29
8. Properties of sidewall elements and tire model components	29
9. Features of the modal analysis models with smooth and straight ribbed tread	34
10. Qualitative summary of runtime analysis	41
11. Measured sinkage and resistance in snow	45

NOMENCLATURE

a	arclength in contact with snow
c	cohesion
c'	apparent cohesion
d	Drucker–Prager material cohesion
e	void ratio
E	Young’s modulus
E_1	tread longitudinal shell modulus
E_2	tread lateral shell modulus
F_c	cap failure surface for compactive–dilatant failure
F_{foam}	foam model failure surface
F_s	shear failure surface
F_t	transitional failure surface
g	flow potential surface for crushable foam model
G_s	flow potential shear surface
G_c	flow potential cap surface
G	shear modulus defining recoverable shear strains
h	snow depth
i	slip
I	moment of inertia
I_i	invariants of normal stress
j	relative slip distance between the wheel and the terrain
J_i	invariants of deviatoric or shear stress
k	constant in equation defining friction as a function of slip distance (eq 26)
K	flow stress ratio (related to shape of yield surface in deviatoric plane)
K_0	coefficient of earth pressure
l	beam length
M	slope of the critical state line in the effective stress plane
ncl	normal compression line
csl	critical state line
p	mean (total) normal stress
p'	mean effective normal stress
p_a	defines the evolution of the hardening and softening of the cap (location of Drucker–Prager cap along the mean pressure axis)
p_b	hydrostatic compression yield stress (Drucker–Prager model)
p_c	hydrostatic compression strength (foam model)
$p_{c 0}$	initial value of hydrostatic compressive stress (foam model)
p_{max}	maximum contact pressure
p_t	hydrostatic tensile yield stress
p_t^{el}	elastic tensile limit
q	deviatoric stress
r	tire radius
R	cap eccentricity parameter (controlling the shape of the cap)
R_s	motion resistance force
s_i	component of stress deviation ($\sigma_i - p$)
t	stress deviator parameter, $t = q$ when $R = 1$
t_{beam}	thickness of the beam
T	temperature
u	pore water pressure
v	specific volume
v_w	wheel speed

v_v	vehicle speed
w	maximum tire width
w_{beam}	width of the beam
W	applied load on the end of the beam
y_{max}	maximum deflection at the free end of the beam
z	sinkage
α	parameter to smooth the transition between the shear and cap failure
β	Drucker–Prager material angle of friction
$\epsilon_{\text{vol}}^{\text{in}}$	volumetric plastic strain
$\epsilon_{\text{vol}0}^{\text{in}}$	initial value of volumetric plastic strain
κ	elastic slope on the pressure–volume curve
λ	plastic slope on the pressure–volume curve
μ	coefficient of friction
ρ	density
ρ_0	initial density
σ_0	initial yield stress in uniaxial compression
σ_h	horizontal stress
σ	normal stress
σ_i	normal stress in the i direction, where $i = x, y, z$ (principal stress when $i = 1, 2, 3$)
σ_{oct}	octahedral normal stress
σ_v	vertical stress
τ	shear stress
τ_{ij}	shear stress, where $i, j = x, y, z$
τ_{oct}	octahedral shear stress
ν	Poisson’s ratio
ϕ	friction angle
ϕ'	apparent friction angle

Finite Element Modeling of Tire–Terrain Interaction

SALLY A. SHOOP

INTRODUCTION

Vehicle mobility on unpaved surfaces is important to the military as well as to agriculture, forestry, mining, and construction industries. The problems can be grouped into two major categories: predicting vehicle performance on various terrains (will it get stuck; how much traction or pull is available to climb or pull) and estimating the consequences of the vehicle passage (rut formation, shearing/tearing of roots, soil compaction, and the effects of these on vegetation and erosion).

The objective of this project is to produce a three-dimensional finite element model of tire-terrain interaction that can be used to explore the effects of tire and terrain variables on vehicle mobility (traction and motion resistance) and terrain deformation (rut formation and shearing). Such a model would enable detailed analysis of the complex interactions resulting from contact friction and would further the understanding of off-road vehicle mobility by defining critical mechanisms involved in vehicle traction and motion resistance. Ultimately the model generated would be used for tire design and specification for off-road vehicles (for construction, mining, and recreation), for vehicle performance prediction, and for terrain damage prediction and reduction of the environmental impact of off-road travel. Previously a three-dimensional simulation of contact between a deformable tire and deformable terrain had been too difficult and computationally time consuming. Recent advancements in the contact formulations of general-purpose finite element codes (e.g. ABAQUS, HKS 1998) and increases in computer processing speeds have brought such a model into the realm of possibility.

The originality of this research lies in accounting for the deformable nature of both the tire and the terrain in a fully three-dimensional model. Both tire and

terrain are highly deformable. A rigid approximation of either is an oversimplification of the problem and would yield erroneous contact conditions, which are critical to obtaining correct solutions. The incorporation of the third (lateral) dimension is similarly necessary, as the lateral movement of the terrain (in addition to deformation in front and beneath the tire) is readily apparent for most soft terrain materials (soils and snow). The effect of the lateral dimension is also evident in equations for rolling resistance, which is a function of the width of the rolling object (Bowden and Tabor 1964, Ludema 1996a). Similarly, empirical sinkage and motion resistance equations by Bekker (1969) for soil and Richmond (1995) for snow include the tire or track width, indicating the impact of the third dimension on the performance of the tire or track.

The details of the tire–soil modeling problem are divided into three topic areas: 1) material models for the terrain material, 2) tire models for use on a deformable substrate, and 3) the combined tire–terrain model and the treatment of the interface. These are presented after a brief historical perspective on tire–terrain interaction.

BACKGROUND

Off-road vehicle performance prediction

Off-road vehicle performance analysis is a three-dimensional, nonlinear, dynamic problem. Major early efforts were led by Bekker, at the University of Michigan and the U.S. Army Land Locomotion Laboratory (Bekker 1956, 1960, 1969), and his contemporaries at the National Tillage Laboratory at Auburn, Alabama (Gill and Vanden Berg 1967). Karafiath and Nowatzki (1978) extended the state of the art to include modeling of soil deformation under the wheel or track based on theoretical soil mechan-

ics using plasticity theory. They developed a two-dimensional finite difference model of tire–terrain interaction that simulated the plastic soil deformation under a tire, accurately reproducing the experimental measurements of sand deformation under a rigid wheel by Wong and Reece (1967), as shown in Figure 1. More-recent seminal books on the subject are those by Yong et al. (1984), which includes some of the early finite element modeling of tire–terrain interaction, and Wong (1989), who approaches numerical modeling of tracked vehicles based on Bekker’s semi-empirical representation of the terrain.

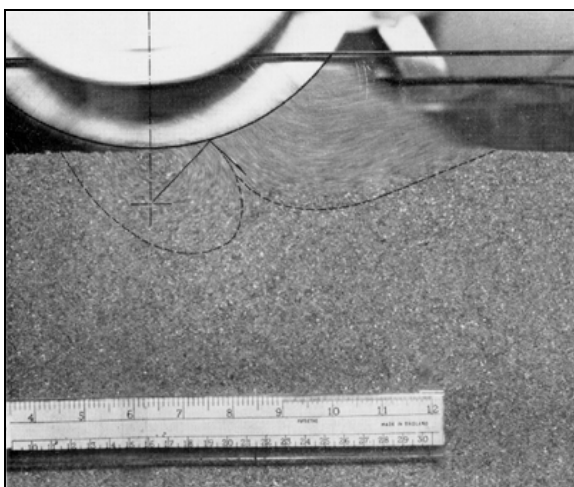


Figure 1. Sand deformation under a towed wheel moving to the right. Dashed lines show the soil failure zones. (From Wong and Reece 1967.)

Because vehicle–terrain interaction is complicated, comprehensive modeling of off-road mobility is usually done using empirical algorithms based on large data sets, such as the NATO Reference Mobility Model (Ahlin and Haley 1992). These are supplemented with high-fidelity simulations using sophisticated vehicle dynamics models, but in the future these simulations will use vehicle–terrain numerical models.

Vehicle movement on snow

Vehicle mobility on snow has some unique characteristics and terminology. The performance of a vehicle in snow is usually limited by the bearing strength of the snow, which controls the amount of sinkage. Sinkage is a function of the compressibility and shear strength of the snow in response to the vehicle load. Since snow strength is difficult to measure in the field on a routine basis, vehicle performance is often related to index parameters that are easier to measure, such as the snow depth and density.

In this study, only fresh snow within a limited range of initial density (less than 250 kg/m^3) was modeled. The snow depth, however, ranged from “shallow” to “deep.” Shallow snow is defined as snow where the “pressure bulb” (the snow compacted due to the weight of the vehicle) intersects a rigid interface. In deep snow the pressure bulb does not intersect a rigid interface below the snow (Fig. 2).

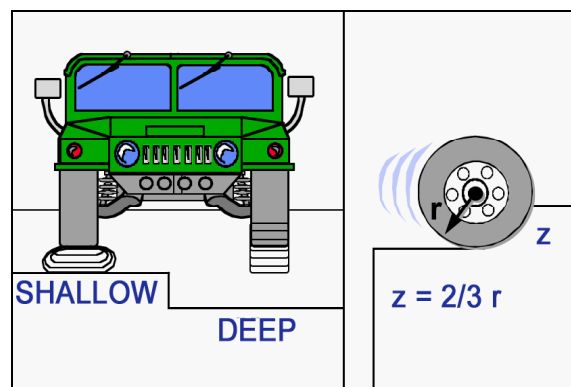
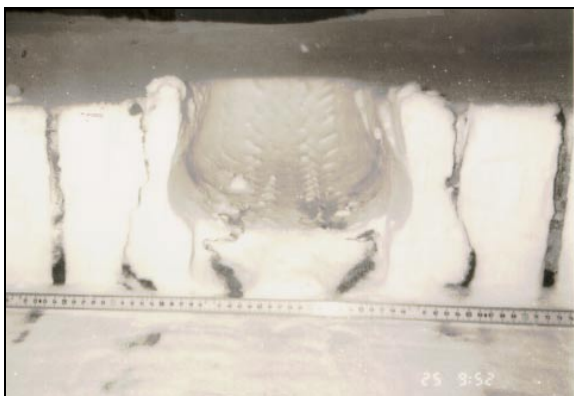


Figure 2. Shallow and deep snow under a wheeled vehicle.

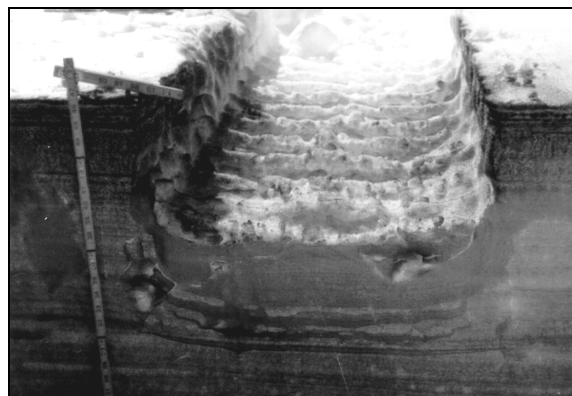
Since the pressure bulb forms in response to a load on the snow, the classification of deep or shallow snow is vehicle dependent and therefore is a function of the vehicle’s weight, load distribution, tire or track geometry, tire pressure, etc. Nonetheless, a rule of thumb is that snow deeper than two thirds of the wheel radius is usually “deep” snow. Except for very specialized vehicles, greater snow depths will impede wheeled vehicle travel because of excessive sinkage. Generally, tracked vehicles with low ground contact pressure are used to traverse deep snow. Figure 3 shows cross sections of the pressure bulb under a vehicle for shallow and deep snow.

Tire–terrain modeling

Because of the complexities involved in vehicle–terrain interaction and the desire to incorporate more of the physics into performance models, there is great interest in applying numerical modeling techniques. Several researchers have produced numerical models simulating tire–terrain interaction over the last 20 years. Many of the models are two-dimensional simulations of a rigid wheel on a deformable surface. Yong and Fattah (1976) and Yong et al. (1978) introduced the first finite element models of tire–terrain interaction using a two-dimensional rigid tire on deformable terrain and then progressing to an elastic tire and calculating the contact using Hertz contact theory. This model was difficult to use, as it needed the



a. Snow deformation under a Jeep Cherokee (2.7 ton, 24 kN) in 19-cm “shallow” snow.



b. Snow deformation under a BV202 (a 3.5-ton, 31-kN, articulated tracked vehicle) in a 122-cm “deep” snow cover. (From Harrison 1975.)

Figure 3. Snow cross sections showing pressure bulb formation.

contact displacements or stresses as input values. Nevertheless, it was a major advance in applying numerical methods to tire–terrain interaction. Modeling the interface between a deformable soil and a deformable wheel has been both problematic and computationally time consuming. Pi (1988) modeled a two-dimensional elastic wheel (connected springs) on a viscoelastic soil for high-speed landing of aircraft on soil. Others have used estimates of the contact stress distribution predefined on the soil surface (Saliba 1990, Chi and Tessier 1995). This approach simplifies the problem and is suitable for analyzing different terrain parameters but has the major disadvantage of requiring an estimate of the contact displacements or stresses *a priori* when this is nearly impossible to predict and very difficult to measure.

Continued advances in computing capabilities and in general-purpose finite element codes have enabled researchers to concentrate on the physics of the model rather than on code development. Sophisticated two-dimensional models of a rigid wheel on deformable soil have been described by Liu and Wong (1996) and Foster et al. (1995). Models have recently been extended to three dimensions by Chi,* Chiroux et al. (1997), and Shoop et al. (1999).

To date, the most realistic representation of a pneumatic tire on deformable soil was done in two dimensions at IKK (Automotive Research Institute) in Hamburg, Germany (Aubel 1993, 1994) (Fig. 4). Fervers (1994) extended Aubel’s model to study the effect of lug design on tire performance (Fig. 5). A good review of the tire–terrain research program at

IKK, including the developments by Aubel and Fervers, is given in Schmid (1995). Fervers further developed his model to a pseudo-three-dimensional representation and used it in several applications, including travel over rough surfaces, soil compaction beneath a rolling tire, and the influence of tread design and slip on tire performance (Fervers 1997, 1999a, 1999b).

Current efforts toward the development of a three-dimensional model of a deformable tire on deformable terrain are being undertaken by 1) the U.S. Army Cold Regions Research and Engineering Laboratory (CRREL), Goodyear, and Caterpillar through a Cooperative Research and Development Agreement; 2) Tordesillas (1996), using a mathematical contact mechanics approach at the University of Melbourne; and 3) Shoop, using the Darnell tire model at the University of Michigan, Automotive Research Center, and CRREL (Mousseau and Hulbert 1996, Darnell et al. 1997, Alvarez Sanz 1999, Darnell, in progress). The Automotive Research Center (IKK) in Hamburg, Germany, and the Transport Technology Research Laboratory, Carleton University, Ottawa, Canada, may also be continuing their research. Researchers at the Virtual Proving Ground at the National Automotive Dynamic Simulator in Iowa have recently begun to pursue this area as well. The research described in this report uses the Darnell tire model, which is efficient enough to make simulations of a rolling tire achievable in near-real time, so the addition of a deformable terrain is computationally feasible. This study also includes the development of a terrain material model for snow.

* Personal communication, L. Chi, Caterpillar, Inc., Peoria, IL, 1996.

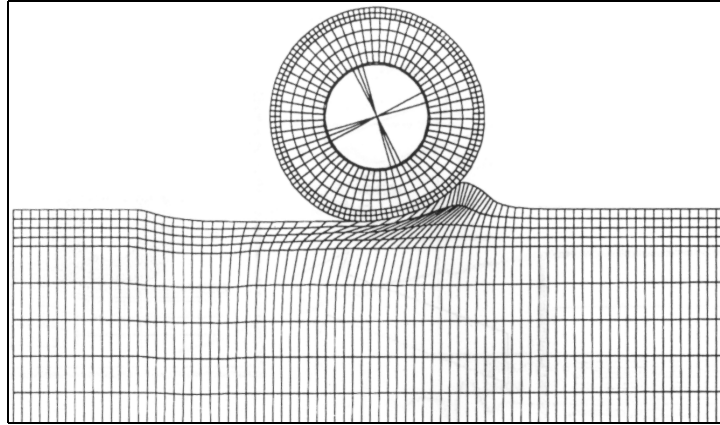


Figure 4. Two-dimensional modeling of tire-terrain interaction by Aubel (1993).

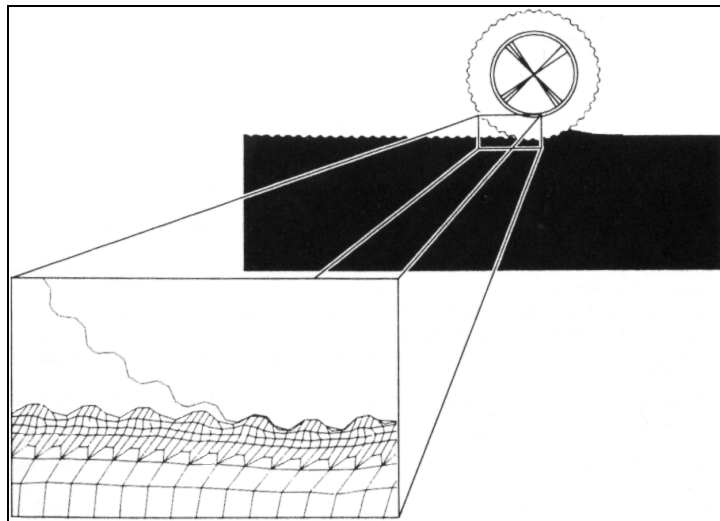


Figure 5. Modeling of the effect of lug design on tread-terrain interaction in two dimensions by Fervers (1994).

Tire terminology

Because of the interdisciplinary nature of this work, some of the tire terminology and conventions are presented here, as they are used throughout the text. The tire direction convention is based on the SAE (Society of Automotive Engineers) standard definitions for vehicle dynamics. Since the tire-terrain models are currently formulated for straight-ahead rolling (zero slip angle), the tire longitudinal axis is in the direction of travel and the lateral or transverse direction is perpendicular to travel (in the horizontal plane), as shown in Figure 6.

The tires modeled are modern radial tires, which are constructed with numerous components, as shown in Figure 7. Each of these elements contributes to the structural behavior of the tire and is considered either individually or *en masse* when creating deformable tire models.

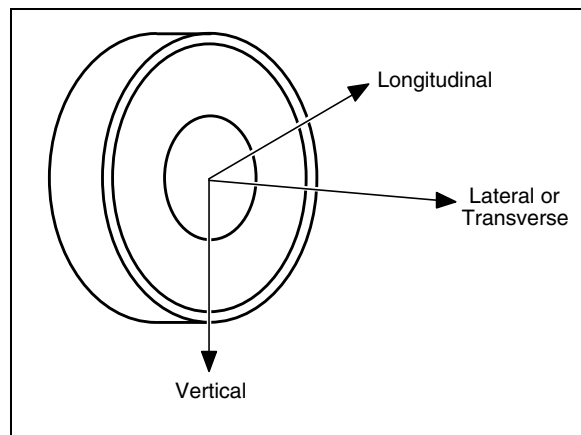


Figure 6. Tire direction convention.

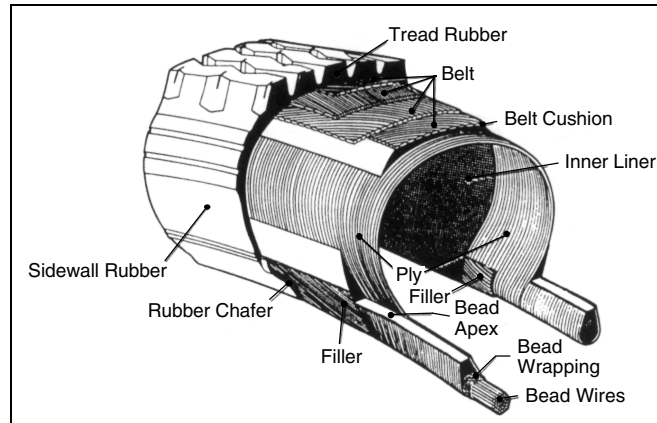


Figure 7. Construction components of a radial ply tire.
(After Goodsell 1995.)

Tire deflection is a primary measure of the tire structural response to load and is often reported based on inflation pressure and vertical load. Deflection is the difference between the unloaded and the loaded section height (and is sometimes reported in percentage, normalized by the unloaded section height). The tire cross section and the deformation of the cross section under load are illustrated in Figure 8. A thorough discussion of tire mechanics is given in Clark (1981).

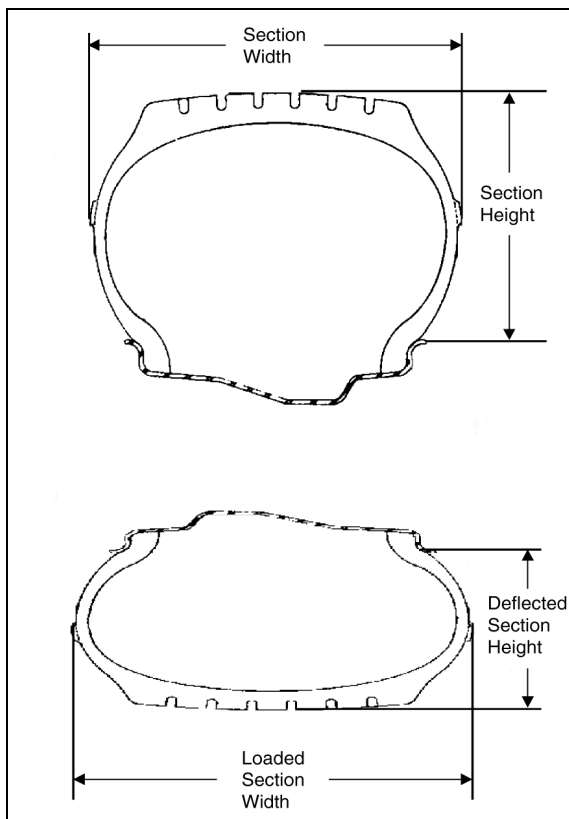


Figure 8. Measurement of tire dimensions.

TERRAIN MATERIAL MODELS

Terrain substrate subjected to vehicle loads has been represented using a wide variety of material models, including elastic, non-linear elastic, visco-elastic (Pi 1988), and elastic-viscoplastic (Saliba 1990). Recent studies have concentrated on using either cap Drucker–Prager plasticity (Aubel 1993, 1994, Fervers 1994) or critical state models such as the Bailey and Johnson (1989) soil compaction model implemented by Foster et al. (1995) or a new critical state model (similar to Lade and Kim 1995) implemented by Liu and Wong (1996). Comparisons between the Drucker–Prager and Cam–clay models for tire–terrain interaction have been published by Meschke et al. (1996) for snow and by Chi and Tessier (1995) for soil. Although the Cam–clay model is perhaps the most widely used soil model, both of the above studies comment on convergence problems when using Cam–clay. The choice of material model is based on balancing the type of behavior desired in the model with the information available to determine model parameters. The terrain materials simulated in this study were fresh snow and compacted sandy soil. The two material models used were a modified Drucker–Prager with a cap, and a critical state, crushable foam model. Both models were considered suitable for capturing the highly compressible behavior of natural fresh snow. The compacted sand was modeled using the modified Drucker–Prager cap only. A description of these models, model parameter determination, and validation of the material models with test data follows.

General concepts for plasticity models

The purpose of a plasticity model is to define the permanent deformation of a plastic material. This is

done with the following basic components (Wood 1990):

- Elastic properties to define the recoverable deformation;
- A mathematical surface to define the yield boundary between elastic behavior and plastic material behavior;
- A plastic flow potential to mathematically define the plastic deformation (also called a plastic flow law); and
- A hardening/softening rule defining the movement (expansion or contraction) of the yield surface during plastic deformation.

A good overview of the development of plasticity theory and constitutive modeling of soil is given in Scott (1985). Schofield (Schofield and Wroth 1968) extended plasticity theory to the critical state concept, defining either contractile or dilatant deformation of porous material as a function of its specific volume or void ratio. In critical state theory this rule is developed around the concept of a “critical state,” where the plastic shearing deformation occurs at a constant volume. Perhaps the most famous critical state model, the Cam–clay model, was developed based on the behavior of clays. The concepts are equally applicable to defining the shearing and volumetric behavior of granular materials such as granular soils or snow (Wood 1990). Although the concepts are applicable for both cohesive and granular materials, the behavior of the granular materials has not been explored as thoroughly, particularly regarding the influence of deviatoric stress on the yield surface, which is less clearly defined in soils but may take on a much different shape than the yield surface of metals. Wood (1990) considers this a difference in detail rather than a difference in concept.

The critical state class of model used in this study is the crushable foam model, specifically designed for highly compressible materials, in which a characteristic of fresh snow. The modified Drucker–Prager cap model also has the features of a critical state model (i.e. regions of constant volume shear deformation, and compactive–dilatant flow). Both models use non-associative flow (i.e. the flow potential is not associated with the yield surface), except on the cap surface of the Drucker–Prager model.

Yield surface

The yield surface for both material models is described in terms of stress invariant functions of the normal σ_i and shear stress τ_{ij} , where i and j are directions x , y , and z and represent principal stresses when $i = 1, 2$, or 3 . Based on elasticity theory (Timoshenko

and Goodier 1970; Jaeger and Cook 1969), the stress invariants are:

I_i = invariants of normal stress:

$$I_1 = \sigma_x + \sigma_y + \sigma_z = \sigma_1 + \sigma_2 + \sigma_3 \quad (1)$$

$$I_2 = -(\sigma_y \sigma_z + \sigma_z \sigma_x + \sigma_x \sigma_y) + \tau_{yz}^2 + \tau_{zx}^2 + \tau_{xy}^2 = -(\sigma_2 \sigma_3 + \sigma_3 \sigma_1 + \sigma_1 \sigma_2) \quad (2)$$

$$I_3 = \sigma_x \sigma_y \sigma_z + 2\tau_{yz} \tau_{zx} \tau_{xy} - \sigma_x \tau_{yz}^2 - \sigma_y \tau_{zx}^2 - \sigma_z \tau_{xy}^2 = \sigma_1 \sigma_2 \sigma_3 \quad (3)$$

J_i = invariants of deviatoric or shear stress:

$$J_1 = s_x + s_y + s_z \quad (4)$$

$$J_2 = \frac{1}{6} \left[(\sigma_y - \sigma_z)^2 + (\sigma_z - \sigma_x)^2 + (\sigma_x - \sigma_y)^2 \right] + \tau_{yz}^2 + \tau_{zx}^2 + \tau_{xy}^2$$

$$= \frac{1}{6} \left[(\sigma_2 - \sigma_3)^2 + (\sigma_3 - \sigma_1)^2 + (\sigma_1 - \sigma_2)^2 \right] \quad (5)$$

$$= (I_1^2 + 3I_2)/3$$

$$J_3 = s_x s_y s_z + 2\tau_{yz} \tau_{zx} \tau_{xy} - s_x \tau_{yz}^2 - s_y \tau_{zx}^2 - s_z \tau_{xy}^2 \quad (6)$$

$$= (2I_1^3 + 9I_1 I_2 + 27I_3)/27$$

where the components of stress deviation s_i are

$$s_i = \sigma_i - p \quad \text{for } i = x, y, z, \text{ and } i = 1, 2, 3. \quad (7)$$

Model parameters are defined in either the pressure–deviatoric plane (also called the meridional, p – q , or p – t plane) or the pressure–volume plane (v – p or v – $\ln p$ plane) according to the following definitions.

1. Mean (total) normal stress, also called equivalent pressure stress, or the octahedral normal stress, which determines uniform compression or dilation:

$$p = \sigma_{\text{oct}} = \frac{1}{3} I_1. \quad (8)$$

For soils, p is often taken as the mean effective stress p' , taking into account the pore water pressure, u :

$$p' = p - u. \quad (9)$$

2. Deviatoric stress, also called the Mises equivalent stress, or the octahedral shear stress, which determines distortion:

$$q = \tau_{\text{oct}} = \sqrt{\frac{2}{9}(I_1^2 + 3I_2)} = \sqrt{\frac{2}{3}J_2} \quad (10)$$

3. An additional deviatoric stress measure, t (HKS 1998):

$$t = \frac{q}{2} \left[1 + \frac{1}{K} - \left(1 - \frac{1}{K} \right) \left(\frac{J_3}{q} \right)^3 \right] \quad (11)$$

where K is a material parameter (between 0.778 and 1.0) that controls the yield dependence on the third stress invariant and defines the shape of the yield surface in the deviatoric plane. The K value allows for different stress failures in tension and compression. For $K = 1$, the yield surface is circular (von Mises yield), as shown in Figure 9, and the failure stress is the same in tension and compression. K is limited to values of 0.778 or greater for the surface to remain convex. Some of the more common failure surfaces are shown in Figure 10 in deviatoric space and in Figure 11 in principal stress space.

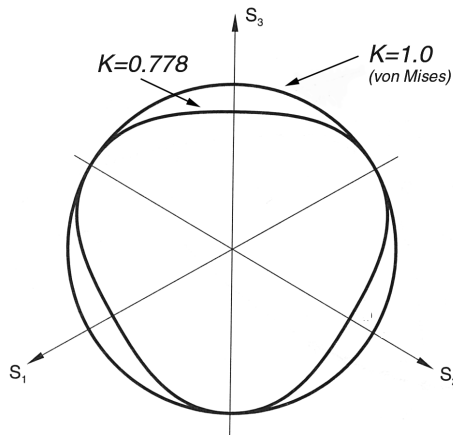


Figure 9. Modified Drucker-Prager yield surface in deviatoric space. (After HKS 1998.)

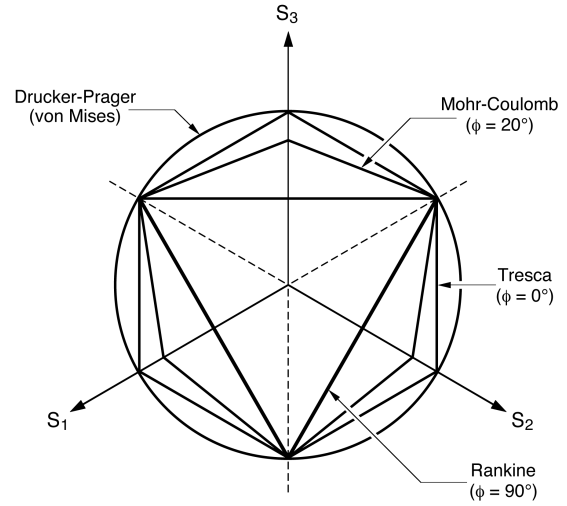


Figure 10. Yield surfaces in deviatoric space. (After HKS 1998.)

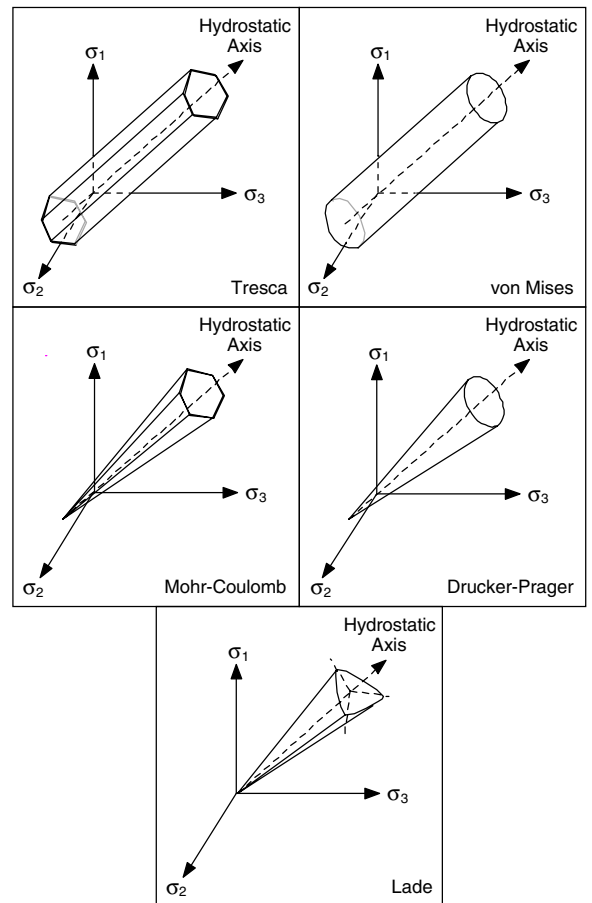


Figure 11. Common yield surfaces along the hydrostatic axis in principal stress space. Caps defining compressive failure are not shown. (After Shen and Kushwaha 1998.)

Cap plasticity models incorporate both the compression and shearing of the material. Critical state models are a type of cap model where a critical state line (*csl*) is located at the peak of the yield surface and divides material yield by compaction on one side and yield by dilation on the opposite side. The material deforms at a constant volume at the critical state. The critical state line (curve) in three-dimensional space defined by normal compressive stress p' , deviatoric (shear) stress q , and specific volume v is shown in Figure 12. For simplicity in gathering the model parameters, the yield surface is generally viewed in planar form in the compressive plane (v - p or v - $\ln p$) or the deviatoric plane (p' - q or p - t).

Hardening law

The cap on the yield surface defines the compressive-dilatant behavior of the material failure as the cap expands and contracts (Fig. 13). The cap is generally spherical or ellipsoidal, and the material either hardens or softens by expanding or contracting the cap. This behavior is defined in the pressure-volume relationship called a hardening law. The pressure-volume relationship is often exponential and therefore can be modeled using an exponential hardening

law (Fig. 14). In cases where exponential hardening is not a good fit, as is common in soils, the hardening law can also be represented in a piecewise linear approach using the experimental data (Fig. 15).

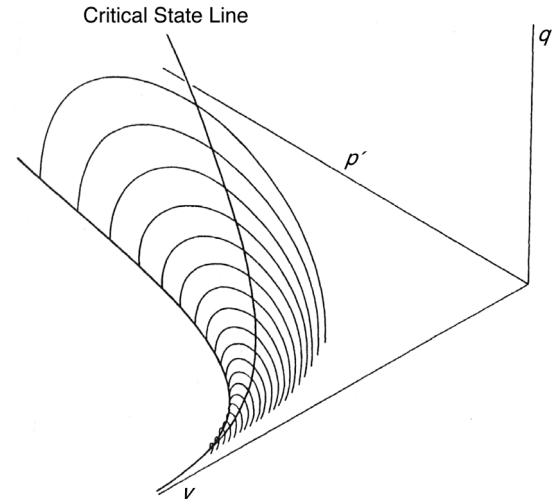


Figure 12. Three-dimensional view of critical state yield surface. The critical state line defines failure at constant volume. (After Wood 1990.)

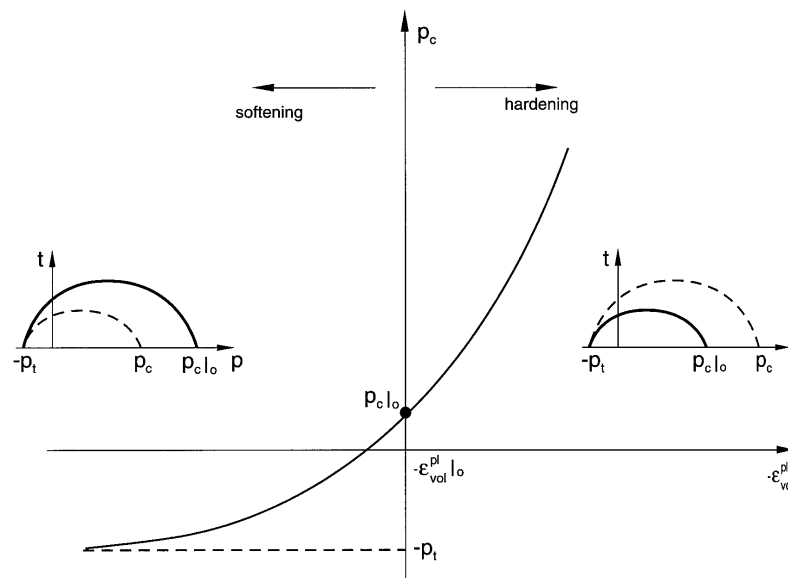


Figure 13. Cap contraction or expansion reflecting the softening (left) or hardening (right) of the material. (After HKS 1998.)

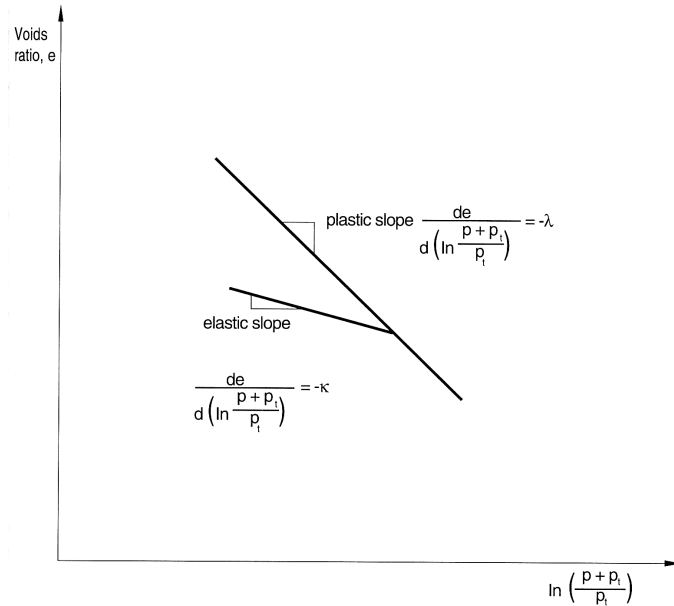


Figure 14. Exponential hardening law for material in hydrostatic compression.

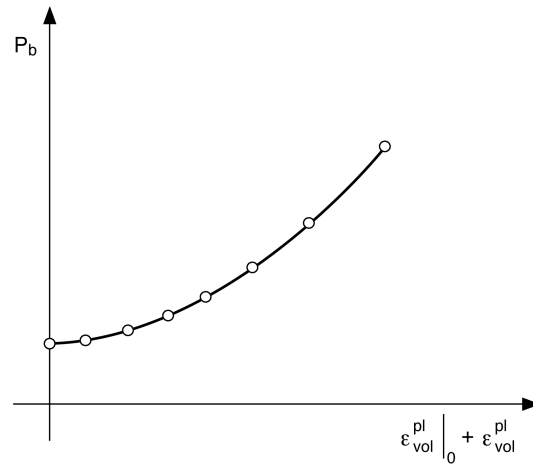


Figure 15. Piecewise linear modeling of the hardening law. (After HKS 1998.)

Hardening can be modeled as isotropic hardening, where the yield surface grows equally in all directions, or as kinematic hardening, where the yield surface moves as a rigid body in principal stress space (Fig. 16). Kinematic hardening is more accurate for modeling cyclic loading of soils but is more computationally intensive. A combination of the two types of hardening is probably the best representation for cyclic loading of soil. The Multi-Mechanical Model (MMM) proposed by Peters (1991)* implements

some of these features without the cumbersome tracking of yield surfaces by engaging a series of yield surfaces (failure mechanisms). The MMM concept has been successfully applied to modeling the cyclic loading of pavements by Smith (2000). This constitutive model is still under development and is currently being calibrated for loose, thawing soil behavior for future applications to tire-terrain modeling. The material models implemented in this study use isotropic hardening, which is considered a reasonable approximation for monotonic loading (one pass of the wheel).

* Also personal communication, Geotechnical and Structures Laboratory, ERDC, Vicksburg, MS, 1999.

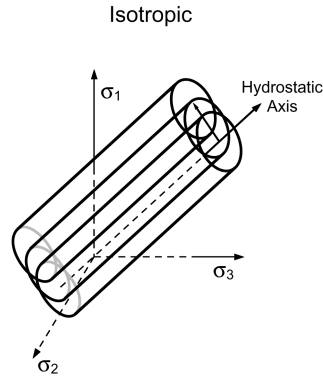
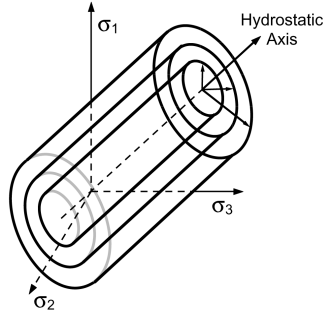


Figure 16. Isotropic and kinematic hardening. (After Shen and Kushwaha 1998.)

Parameters

A relatively small number of parameters are needed for these material models. Although more detailed models may provide a more accurate solution, the parameters needed to define the model become prohibitively numerous and are often unavailable. The objective of any model is to capture the most important material behaviors without being unduly cumbersome. The following descriptions of the material parameters are based on the models as implemented in ABAQUS (HKS 1998). Additional information on soil plasticity and critical state soil mechanics is given in Wood (1990).

The model parameters used in this study are:

- d = Drucker–Prager material cohesion
- β = Drucker–Prager material angle of friction
- λ and κ = slopes of the loading (compression) and unloading (elastic) lines in the compression plane as indicated in Figure 14. This hardening or softening of the material can also be defined in a piecewise manner (Fig. 15).

- M = slope of the critical state line in the p – q plane, which controls the shape of the yield ellipse
- E = Young’s modulus of elasticity defining recoverable strain
- ν = Poisson’s ratio.

The following sections explain the Drucker–Prager cap model and the crushable foam model in more detail.

Modified Drucker–Prager cap model

For the modified Drucker–Prager cap model used in this study, the yield surface is a modified von Mises yield (i.e., the material constant $K = 1.0$), which is circular in the deviatoric plane (Fig. 9). In the p – t plane the yield surface has two major segments: the Drucker–Prager shear portion of the curve (analogous to the Mohr–Coulomb line) defines shear deformation, and the cap portion of the surface defines the intersection with the pressure axis (Fig. 17). The following equations define the yield criteria in each section of the yield surface.

For the Drucker–Prager shear or distortional failure:

$$F_s = t - p \tan \beta - d = 0. \quad (12)$$

For the cap region of compactive–dilatant failure:

$$F_c = \sqrt{(p - p_a)^2 + \left[\frac{Rt}{(1 + \alpha - \alpha / \cos \beta)} \right]^2} - R(d + p_a \tan \beta) = 0 \quad (13)$$

where α is a transition parameter, ranging typically from 0.0 to 0.05, that smooths the transition between the shear failure and the cap failure, R is a material parameter controlling the cap eccentricity, and p_a defines the evolution of the cap along the pressure axes (via p_b – ϵ_{vol} hardening law) according to

$$p_a = \frac{p_b - Rd}{(1 + R \tan \beta)}. \quad (14)$$

The transition between the shear and the cap failure is

$$F_t = \sqrt{(p - p_a)^2 + \left[t - \left(1 - \frac{\alpha}{\cos \beta} \right) (d + p_a \tan \beta) \right]^2} - \alpha(d + p_a \tan \beta) = 0. \quad (15)$$

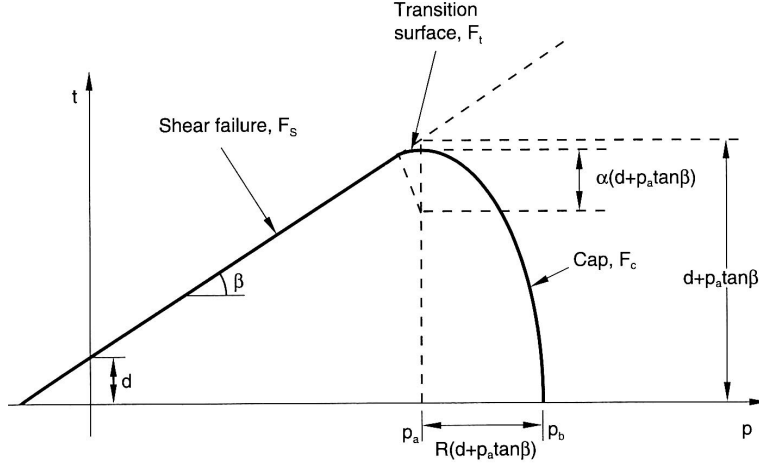


Figure 17. Modified Drucker-Prager cap yield surface in the p - t plane. (After HKS 1998.)

The pressure-volume relationships define both hardening and softening through volume changes based on how the cap portion of the yield surfaces expands and contracts. The hardening of the cap can be defined as an exponential relationship in the pressure-volume space as shown in Figure 14, or it is entered in a piecewise fashion (Fig. 15) as a table of p_b and ϵ_{vol}^{pl} pairs. The piecewise approach is recommended by HKS (1998) for a better fit to the data and better model performance. Both methods were used in this study.

The plastic flow is defined by an elliptical potential surface (Fig. 18). Flow is associative (nor-

mal to the surface) in the cap region; therefore, the equation for the flow surface is identical to the equation for the cap yield surface. In the transition and shear regions, the flow is non-associative (the flow potential is not perpendicular to the failure surface) and is defined by the following equation for the flow potential:

$$G_s = \sqrt{\left[(p_a - p) \tan \beta\right]^2 + \left[\frac{t}{1 + \alpha - \alpha / \cos \beta}\right]^2}. \quad (16)$$

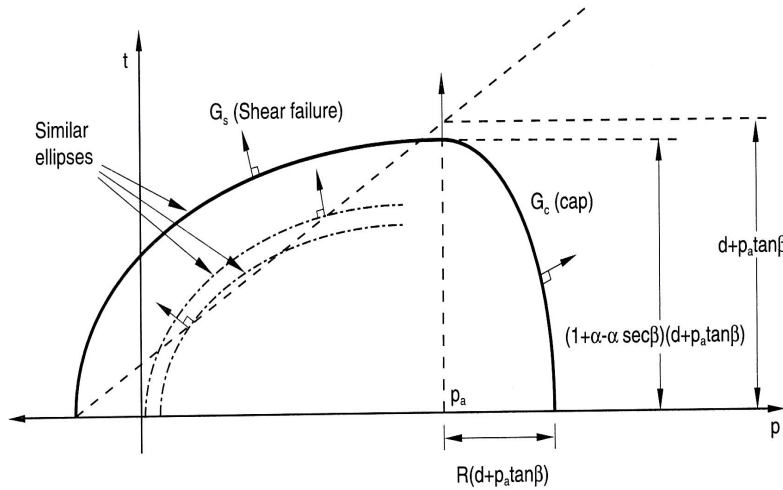


Figure 18. Modified Drucker-Prager cap flow potential in the p - t plane. (After HKS 1998.)

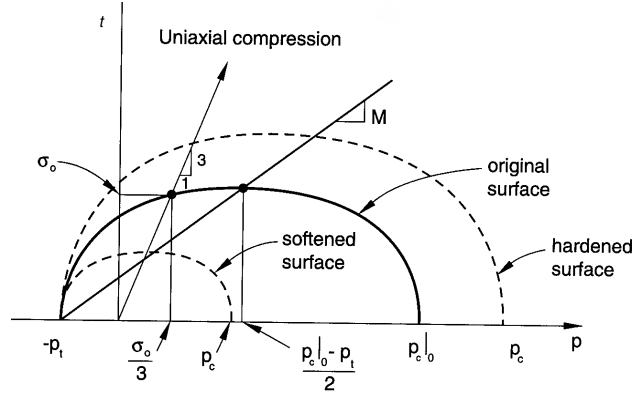


Figure 19. Yield surface for the crushable foam model. (After HKS 1998.)

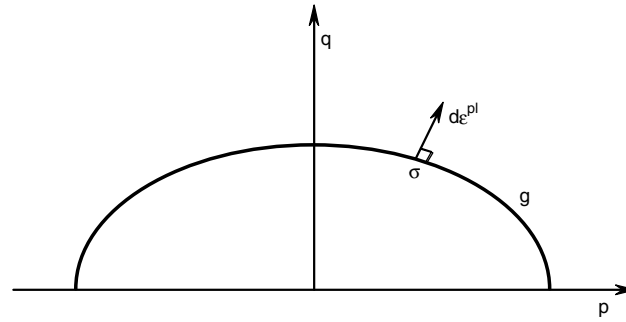


Figure 20. Plastic flow surface for the crushable foam model.

Crushable foam model

The crushable foam model is a class of critical state model and has many similarities to the form of the Drucker–Prager cap model. The crushable foam model, however, has a single ellipse forming the yield surface (Fig. 19), defined by (HKS 1998)

$$F_{\text{foam}} = f - f_0 = \left[\left(\frac{p_t - p_c}{2} + p \right)^2 + \left(\frac{t}{M} \right)^2 \right]^{1/2} - \frac{p_c + p_t}{2} \quad (17)$$

where p_t is the material strength in hydrostatic tension, p_c is the material yield stress in hydrostatic compression, and M is the slope of the critical state line in p – t plane. As indicated in Figure 19, the yield surface hardens and softens with yield but the p_t is assumed constant (isotropic hardening).

In the crushable foam model the plastic flow is non-associative and perpendicular to the flow surface g (Fig. 20):

$$g = \sqrt{\frac{9}{2} p^2 + q^2} \quad (18)$$

This assumes a flow direction identical to the stress direction for stress paths along the p axis, which suggests that loading in any principal direction results in insignificant deformation in the other directions (HKS 1998). The validity of this assumption for snow was examined as part of this study.

The hardening law takes the same form as the hardening law for the Drucker–Prager cap model.

Constitutive models for snow

Two material models were judged to have performance characteristics most similar to natural fresh snow: a Drucker–Prager cap plasticity model and a critical state plasticity, crushable foam model. Liu (1994) used the Drucker–Prager plasticity model for modeling the sliding of rubber blocks on snow. Mundl et al. (1997) extended Liu’s work using a multi-surface plasticity model to optimize the snow behavior under both shear and compression. Their intent, however, was to simulate shearing forces on compacted snow on roads (with a density of 500 kg/m³), which is a significantly different material than encountered during cross-country mobility on fresh snow (with a density of 200–300 kg/m³). For

this study the plasticity model used was the well-documented Drucker–Prager cap.

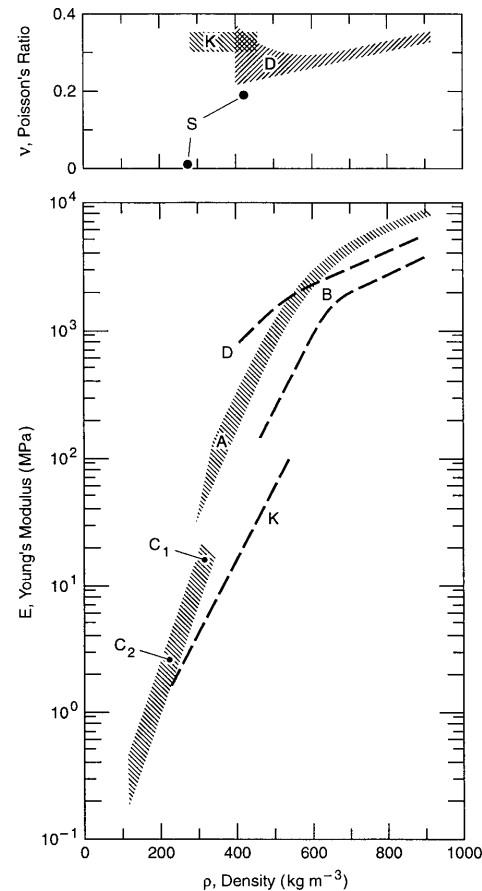
The second material model, a crushable foam model, was chosen based on work by Johnson et al. (1992), where a crushable foam model was successfully applied to natural snow. Johnson used PRONTO, an explicit finite element code from Sandia National Lab, to simulate shock wave propagation in one dimension. For tire–snow interaction, however, the model must simulate snow deformation in a three-dimensional stress field. Initial simulations using the ABAQUS crushable foam model showed that no lateral deformation resulted from an axial load. This issue prompted questions regarding the deformation behavior of snow under a purely vertical load and whether the predicted response from a crushable foam model was suitable for snow in a three-dimensional stress state. Experiments measuring the lateral deformation of snow under a purely vertical load were conducted in cooperation with the Keweenaw Research Center in Houghton, MI (Shoop and Alger 1998). Results indicate that vertical loading of non-sintered snow causes primarily vertical deformation. Fukue (1979) performed experiments that showed that lateral deformation was minimal for high load rates. Both of these studies support our choice of crushable foam models for vehicle loading.

Material parameter determination

Extreme changes in snow properties with time, temperature gradients, applied load, and deformation prohibit model parameter acquisition from the same snow. Therefore, approximations were made by estimating parameters using test data from snow of similar characteristics (density, age, snow type, and location). The type of snow modeled was a fresh snow with a density of 200–250 kg/m³ at moderate temperatures (between –10° and –1°C). Test data were gathered from the field and from the literature to match this snow type as closely as possible. Because data were gathered from several studies, the snow was not exactly the same in crystal structure, but this effect is minimized in fresh snow where sintering (bonding between snow grains) has not occurred. Also, most of the tests were performed on “lake effect” snow from the Keweenaw Peninsula in the Upper Peninsula of Michigan, which is a fairly consistent snow type under normal winter conditions. A discussion of selecting the initial values of the material parameters follows.

Elastic properties. For snow deformation under a tire, the plastic deformation is much greater than the elastic deformation; however, the elastic deformation contributes to energy losses during rolling resistance. The basic elastic parameters, Young’s modulus E and

Poisson’s ratio ν , were estimated based on data compiled by Mellor (1975) and expanded on by Shapiro et al. (1997) (Fig. 21). Since the elastic modulus is a strong function of density, varying over four orders of magnitude, the elastic modulus should ideally be modeled as a function of the density as a state variable. For this study, however, Young’s modulus was held constant at a value equivalent to snow with a density of 300–400 kg/m³. At snow densities less than this, the elastic contribution will be minimal.



- A** = Pulse propagation or flexural vibration at high frequencies, –10° to –25°C
- B** = Uniaxial compression, strain rate approximately 3×10^{-3} to $2 \times 10^{-2} \text{ s}^{-1}$, temperature –25°C
- C₁** = Uniaxial compression and tension, strain rate approximately 8×10^{-6} to $4 \times 10^{-4} \text{ s}^{-1}$, –12° to –15°C
- C₂** = Static creep test, –6.5° to –19°C
- D** = Complex modulus, 10³ Hz, –14°C
- K** = Static Young’s modulus and quasi-static Poisson’s ratio
- S** = Quasi-static measurements of Poisson’s ratio

Figure 21. Compilation of Young’s modulus and Poisson’s ratio measurements on snow. [After Mellor (1975) and Shapiro et al. (1997)]

Porous elasticity accounts for the elastic properties of materials that undergo large volume changes, such as fresh snow. To implement a porous elasticity model, the additional parameters needed are the slope of the elastic portion of the pressure–volume curve (during an unload–reload event, as illustrated in Figure 14); κ , representing the elastic portion of compaction; and the elastic tensile limit, p_t^{el} . The elastic compaction value was not available since compaction tests were performed under monotonic loading (no unloading), so κ was chosen to provide realistic elastic behavior within the stress ranges of the simulations. The elastic tensile limit p_t^{el} was chosen to be the same as the same as tensile limit p_t used to define the yield surface.

Yield surface. The parameters defining the shear portion of the yield surface for the Drucker–Prager model can be calculated from the Mohr–Coulomb cohesion c and the internal angle of friction ϕ , assuming plane strain response and non-dilatant flow. Although non-dilatant flow can be assumed for the

compaction beneath the tire, a plane strain response may be more appropriate for deep snow than for shallow snow, as illustrated in the snow deformation measurements in Figure 3. The Drucker–Prager material cohesion d and the Drucker–Prager material angle of friction β can be calculated from

$$\tan \beta = 1.73 \sin \phi \quad (19)$$

$$d = c \cdot 1.73 \cos \phi. \quad (20)$$

Acquiring apparent values for cohesion c' and friction angle ϕ' from shear loading of snow under a vehicle tire and from a ring shear device is discussed by Blaisdell et al. (1990) and Alger and Osborne (1989). Both methods were applied to field measurements on undisturbed snow with a density ranging from 60 to 250 kg/m³ and temperatures from –2° to –16°C. The results are shown in Figure 22, along with the values used in the CRREL Shallow Snow Model (SSM 1.0) (Blaisdell et al. 1990).

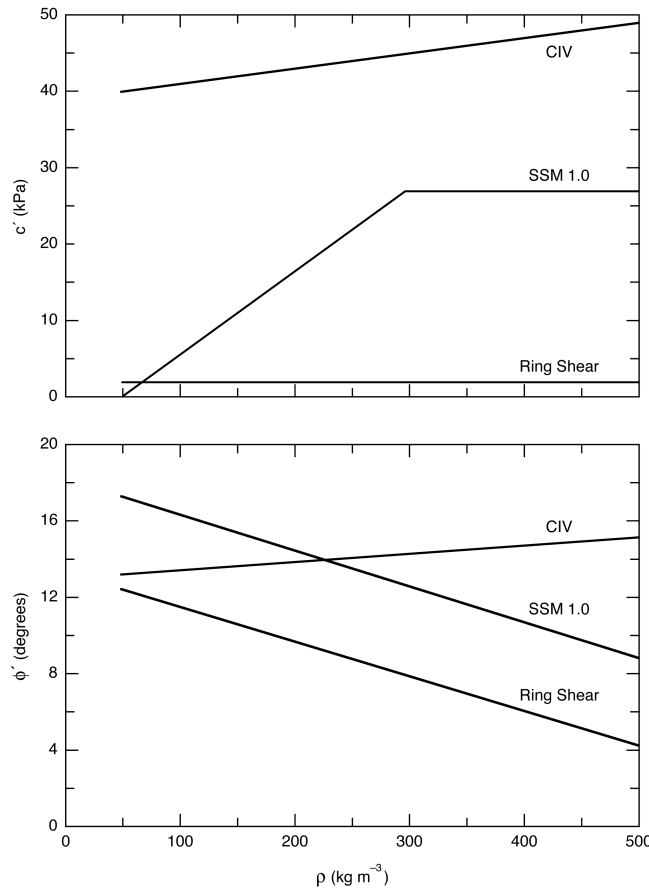


Figure 22. Calculated c' and ϕ' using measurements from the CRREL Instrumented Vehicle (CIV) and the ring shear device and predicted using the Shallow Snow Model, SSM 1.0. (From Blaisdell et al. 1990.)

Using these graphs, for a snow density of 200 kg/m³, values ranged from $c' = 2.14$ kPa and $\phi' = 8.98^\circ$ for the ring shear device to $c' = 43$ kPa and $\phi' = 14^\circ$ using the CIV. Because of the nature of the test, these values may be more representative of the interface shear. However, similar values of cohesion (approximately 20–30 kPa) were reported in Shapiro et al. (1997). These values yield a Drucker–Prager β ranging from 15.2° to 22.5° and a d ranging from 3.7 to 72 kPa.

Parameters describing the shape of the cap were adjusted based on model response. The flow stress ratio K (ratio of tensile strength to compressive strength) was held at 1.0. This agrees with data presented in Mellor (1975) and Shapiro et al. (1997), indicating nearly equal values of compressive and tensile strength for low-density snow (data set **M** in

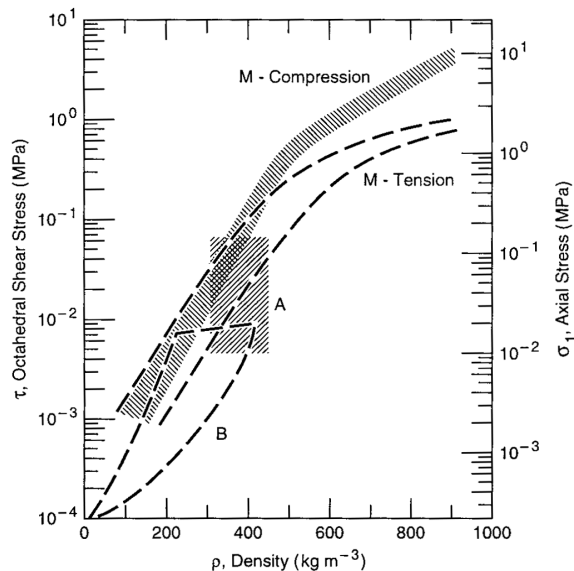
Fig. 23). The cap eccentricity parameter R was chosen based on typical values for earth materials having a very steep compaction cap ($R = 0.02$ to 0.0001). The transition surface radius α was set to 0.0 for no transition. The initial cap yield surface position $\varepsilon_{vol}^{pl}|_0$ was arbitrarily set to 0.001 to allow initial softening.

For the foam model the initial yield stress in uniaxial compression σ_0 was based on data in Shapiro et al. (1997). The initial yield surface position in hydrostatic compression $p_{c|0}$ (for exponential hardening) was chosen to allow for initial softening or hardening (about half the value of σ_0). The hydrostatic tensile strength p_t was selected as 10% of $p_{c|0}$ as a general rule for foam materials. M is calculated from the other input parameters.

These material parameters were refined based on model response and are presented in Table 1.

Table 1. Initial material model parameters.

Drucker–Prager cap	Foam	Elastic
$d = 5,000$ to $30,000$ Pa	$\lambda = 0.35$	$\kappa = 0.005$
$\beta = 22.53^\circ$	$p_{c 0} = 113.76$ Pa	$\nu = 0.3$
$R = 2.2E-2$ to $1.1E-4$	$-\varepsilon_{vol}^{pl} _0 + \varepsilon_{vol}^{pl} ^+ = 0.0005$	$p_t^{el} = 11.376$ Pa
$\varepsilon_{vol}^{pl} _0 = 0.001$	$p_{c 0} + p_t = 113.76$ Pa	$E = 13.79$ MPa
$\alpha = 0.0$	$p_t = 11.376$ Pa	
$K = 1.0$	$\sigma_0 = 275.79$ Pa	
	$K = 1.0$	



- A** = Strain rates greater than $5 \times 10^{-4} \text{ s}^{-1}$
B = In-situ tensile strength
M = Uniaxial compressive and tensile strength under rapid loading

Figure 23. Compilation of uniaxial strength data.
[After Mellor (1975) and Shapiro et al. (1997).]

Hardening. Two methods were used to handle the hardening data: 1) using an exponential hardening function and 2) using tabular data. For exponential hardening, the slope of pure hydrostatic compression behavior λ is obtained by plotting the void ratio against $\ln[(p + p_t)/p_t]$, as shown in Figure 14, where p is the hydrostatic pressure and p_t is the strength in hydrostatic tension. For the snow pressure–volume relationship, void ratio was plotted against $\ln(p)$ since p_t was not precisely known. For snow, p_t is a very small quantity and only the slope is required, which is minimally affected when $p \gg p_t$. These plots were generated using the compression test data published in Abele and Gow (1975).

Values for the logarithmic hardening modulus were calculated using three different compression tests of similar snow density, along with values calculated from the final pressure–density pairs of an additional 21 tests, all from Abele and Gow (1975). Since the measurements are from one-dimensional compression or consolidation (oedometer) tests by application of a vertical load to a sample within a rigid cylinder (i.e. uniaxial strain), the calculation of the mean hydrostatic pressure p is not straightforward. One approximation calculates the horizontal

stresses σ_h based on earth pressure theory assuming that they are related to the vertical stress σ_v by a factor of K_0 , known in soil mechanics as the earth pressure coefficient, where

$$\sigma_h = K_0 \sigma_v. \quad (21)$$

The earth pressure factor can be calculated from the friction angle using

$$K_0 = 1 - \sin \phi. \quad (22)$$

Based on Alger's shear measurements (Alger 1988, Alger and Osborne 1989), the average K_0 value is approximately 0.12. Assuming that the maximum principal stress is vertical (as would be expected in uniaxial compression tests on undisturbed snow) and using equations 8 and 21:

$$p = \frac{1}{3}(\sigma_1 + \sigma_2 + \sigma_3) = \frac{1}{3}(1 + 2K_0)\sigma_1 \quad (23)$$

which, for $K_0 = 0.12$, reduces to

$$p = 0.413 \sigma_1. \quad (24)$$

Using this expression to calculate the mean stress from individual uniaxial consolidation tests with a density of 200–390 kg/m³ (Abele and Gow 1975, tests 3, 10, and 29) results in a range of λ between 0.223 and 0.454.

An additional data set was obtained using the combined data from 21 consolidation (oedometer) tests on snow with initial densities of 200–220 kg/m³ and temperatures of 0° to –3°C. These data are shown in Figure 24 and fall within the expected range of stress–density data for snow shown in Figure 25. Selected points from the best-fit line of these data were used to calculate the values in Table 2 and are plotted in Figure 26 to obtain an average λ of 0.33.

The hardening table data were taken from an average of Abele and Gow tests on warm, 200-kg/m³ snow (tests 10 and 29) and are given in Table 3.

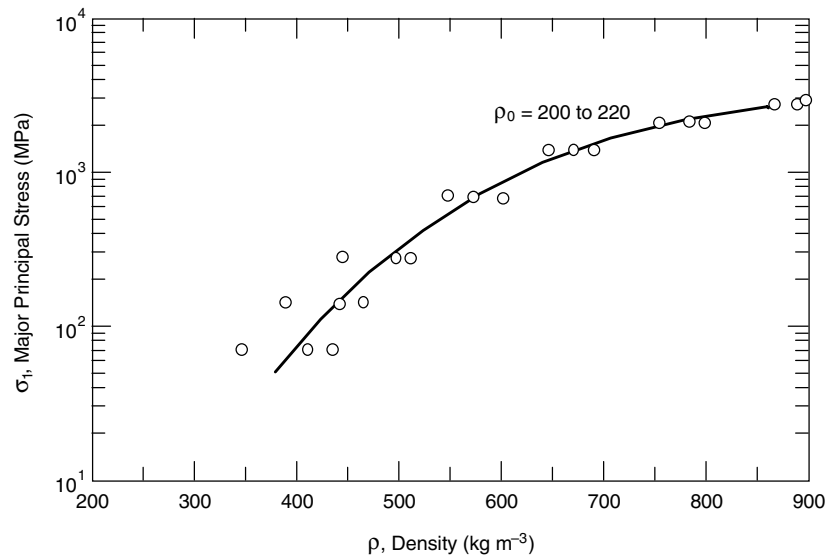
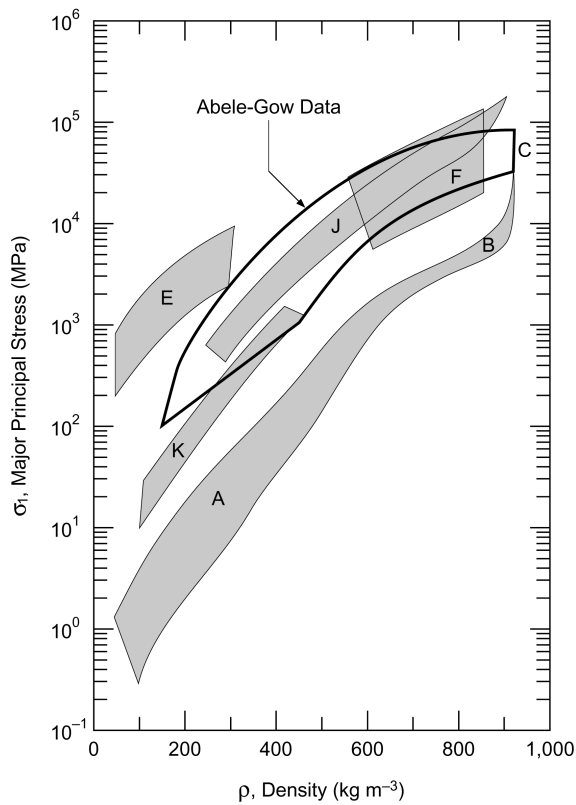


Figure 24. Compression of natural snow at 0° to –3°C. (After Abele and Gow 1975.)

Table 2. Pressure–volume data calculated from the Abele and Gow (1975) data set for 200- to 220-kg/m³ snow at 0° to –3°C.

ρ (kg/m ³)	σ_1 (MPa)	$p = 0.413 \sigma_1$ (MPa)	$\ln p$	Void ratio, e
900	2.8	1.16	0.15	0.00
770	2	0.83	0.19	0.17
620	1	0.41	0.88	0.45
540	0.5	0.21	–1.58	0.67
470	0.2	0.08	–2.49	0.91
410	0.1	0.04	–3.19	1.20
380	0.05	0.02	–3.88	1.37



- A** = Natural densification of snow at -1° to -48°C
- B** = Slow natural compression of dense firn and porous ice (from polar caps)
- C** = Slow compression of solid ice
- E** = Calculated values from plane wave impact at 20–40 m/s
- F** = Hugoniot data for explosively generated shock waves with impact velocity of 1–12 m/s at temperatures of -7° to -18°C
- J** = Compression at strain rate 10^{-4} s^{-1} at -7° to -18°C
- K** = Compression in uniaxial strain with incremental loading at -2° to -3°C
- Solid Lines** = Abele and Gow data, $T = 0^{\circ}$ to -34°C , $\rho_0 = 90$ to 270 kg/m^3

Figure 25. Compression of undisturbed snow and ice. (After Abele and Gow 1975.)

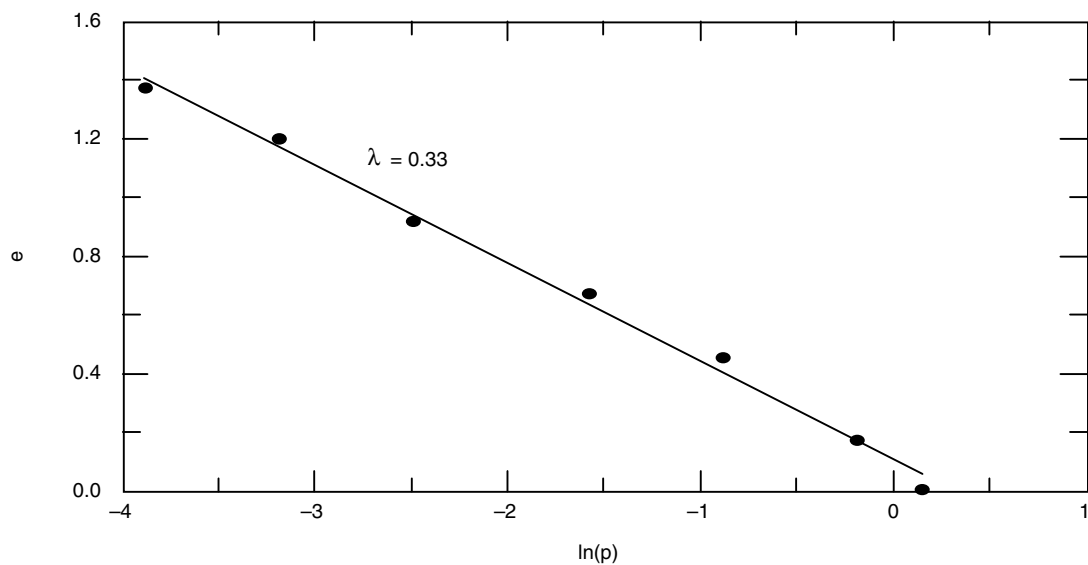


Figure 26. Pressure–volume data from compression tests of Abele and Gow (1975).

Table 3. Hardening table for fresh snow with a density of 200 kg/m³.

$p = 1/3 \sigma_1$ (Pa)	$p = 0.413 \sigma_1$ (Pa)	$p = \sigma_1$ (Pa)	ε_{vol}^{pl}
37.92	46.98	113.76	0
0.017E6	0.021E6	0.05E6	0.593
0.033E6	0.041E6	0.1E6	0.669
0.067E6	0.083E6	0.2E6	0.806
0.167E6	0.207E6	0.5E6	0.944
0.333E6	0.413E6	1.0E6	1.083
0.667E6	0.826E6	2.0E6	1.299
0.933E6	1.156E6	2.8E6	1.455
1.083E6	1.342E6	3.25E6	1.475
2.0E6	2.478E6	6.0E6	1.50
2.0E7	2.478E7	6.0E7	1.514

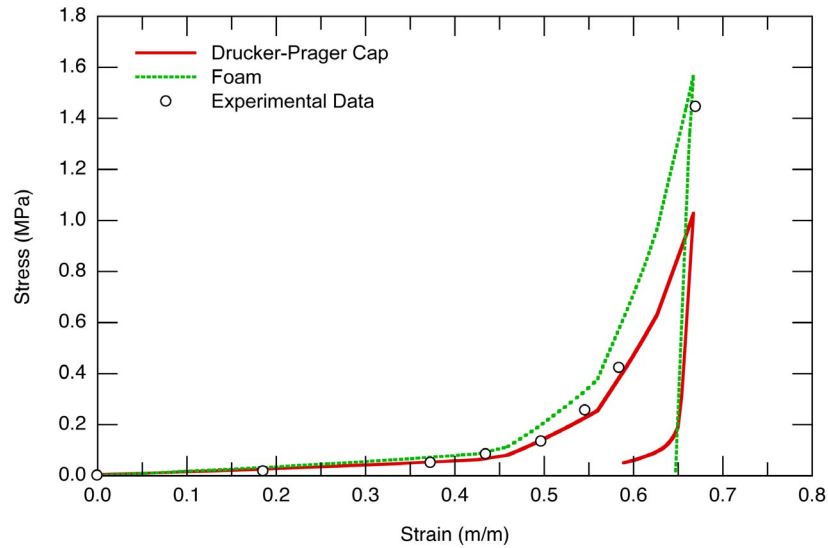


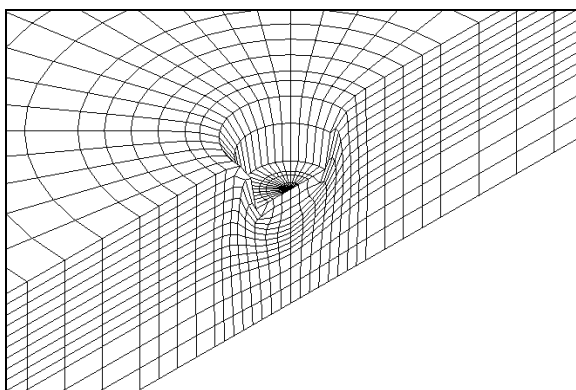
Figure 27. Comparison of model and experimental data for uniaxial compression tests on low-density snow.

Model calibration against laboratory strength tests. A finite element model simulating the uniaxial confined compression tests was used to refine the material properties shown in Tables 1 and 3. A single element model was determined to be adequate after multi-element models gave the same results. The uniaxial compressive test data used for calibration were from the best-fit line for fresh snow of density 200–220 kg/m³ and temperatures of 0° to –3°C from Figure 24. A comparison between the experimental data and model results is given in Figure 27. The agreement between modeled and measured material behavior is good for both the Drucker–Prager cap model and the crushable foam model.

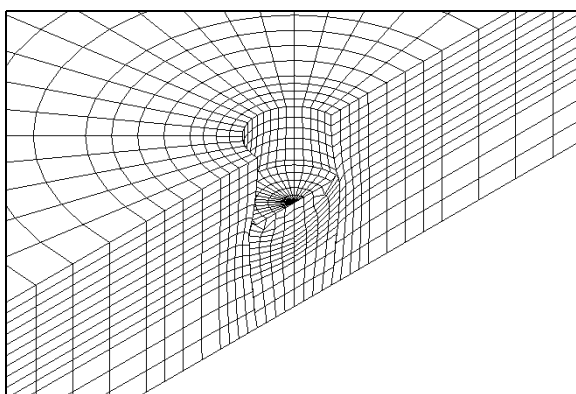
Material model validation with plate sinkage tests

The initial model parameters were applied to a plate sinkage test for snow of similar age and density.

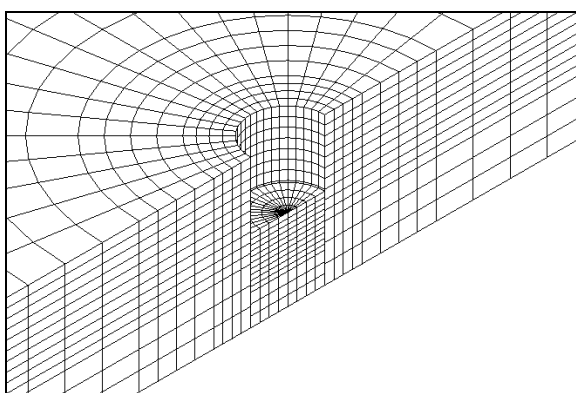
Two different plate sinkage tests were used in the comparisons. The field test consisted of pushing a 20-cm- (8-in.-) diameter rigid plate, originally at the surface, into 40 cm (16 in.) of fresh snow with average density of 200 kg/m³ (Alger and Osborne 1989). The laboratory test pushed a 23-cm- (9-in.-) diameter rigid plate into a cube of snow 60 × 60 × 50 cm deep with an average initial density just under 200 kg/m³. Three different models were used to simulate the plate sinkage tests: 1) a Drucker–Prager cap material, 2) a Drucker–Prager cap material with vertical shear surfaces along the snow–plate interface, and 3) a crushable foam material model with shear surfaces along snow–plate interface. The vertical frictional surfaces allowed these elements to slide, reducing element distortion, which more closely mimicked the shear surfaces observed in the field. The slide planes were modeled using a contact surface with Coulomb friction of $\mu = 0.3$.



a. Drucker-Prager cap material.



b. Drucker-Prager cap with vertical shear contact surface.



c. Crushable foam with shear contact surface.

Figure 28. Deformed meshes for field plate sinkage simulations.

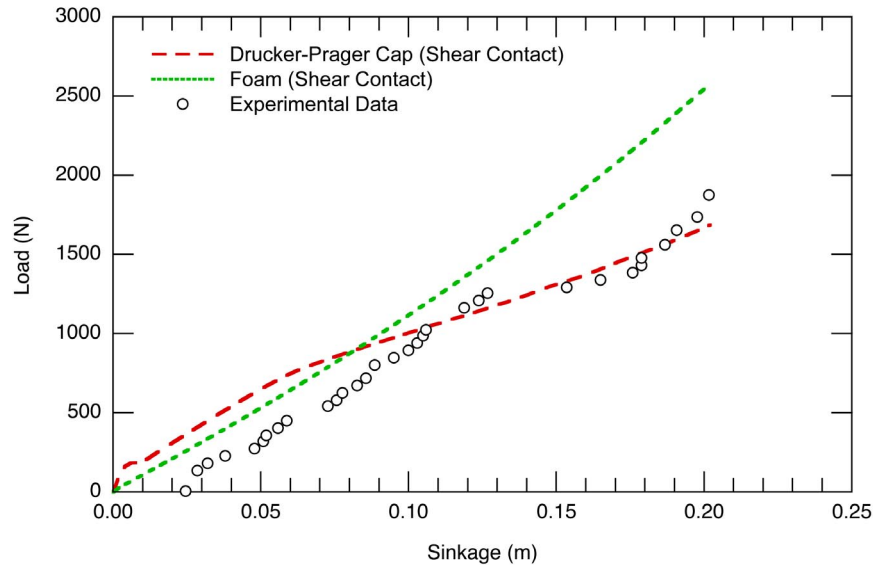
The plate was lowered by constraining the surface nodes radially while displacing them into the snow, effectively creating a no-slip contact between the

plate and snow. The deformed meshes for each of the models of the field test are shown in Figure 28. Figure 28b clearly shows the effect of the shear surface on the sides of the plate, with the model deforming similarly to field observations, compared to the undesirable element distortion along the sides of the plate when these elements are not allowed to slide (Figure 28a). In future models, adaptive meshing, where the mesh adjusts to accommodate large distortions, should help alleviate the problem of excessive distortion without the use of the shear contact surface. Also clearly seen in Figure 28 is the lateral deformation of the snow beneath the plate in the Drucker-Prager cap models (Fig. 28a and b), but no lateral deformation is seen in the crushable foam model (Fig. 28c).

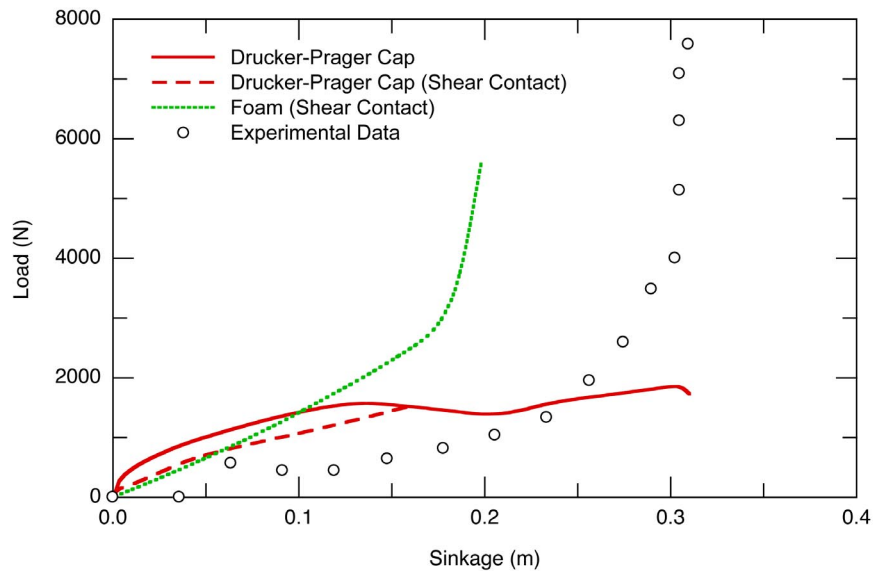
The force-displacement curves for the plate moving into the snow are compared to the experimental measurements in the laboratory and field in Figure 29. The model matches the controlled laboratory test well, particularly for the Drucker-Prager cap model. In the field test the hardening behavior was difficult to simulate. The laboratory test was not run to maximum resistance and would be similar to a “deep snow” condition, while the plate in the field test was pushed to ultimate resistance, causing compaction equivalent to a “shallow” snow condition.

Snow density can be calculated from the modeled volumetric plastic strain using the hardening tables and the pressure-volume relationships in Tables 2 and 3. The snow density values from the models are shown in Figure 30. These densities can be compared to snow densities measured under the plate, as shown in Figure 31. The maximum volumetric inelastic strain in the plate sinkage model occurred in isolated locations adjacent to the plate at values of approximately 0.5, which is equivalent to a snow density of 420 kg/m^3 , whereas very dense snow ($440\text{--}520 \text{ kg/m}^3$) was measured up to 5 cm below the plate (Fig. 31). These values correspond to a strain of 0.5 m/m or greater (assuming primarily vertical deformation) on the uniaxial stress-strain model calibration curve (Fig. 27). The divergence of the models and data at strains greater than 0.5 m/m (Fig. 26) would account for density discrepancies in the plate sinkage measurements and models in high strain areas. On the whole, however, most of the strain occurs at levels of 0.4 or less, so the model provides a good fit to the overall plate sinkage behavior.

The laboratory tests were also used to evaluate the lateral deformation of the snow, since field observations show lateral deformation under a vehicle load. On closer examination of the literature, however, few examples were available where the snow had been



a. Laboratory tests.



b. Field tests.

Figure 29. Comparison of modeled and measured plate sinkage test for laboratory and field tests.

marked in a way that would enable the observation of lateral movement.

In addition, the nature of loading from vehicles is not strictly vertical. Therefore, an experiment was devised to mark several snow samples both vertically and horizontally and subject them to purely vertical loading. The snow in Figure 31 was one such experiment, clearly indicating no lateral deformation, since the vertical marks remained vertical throughout

the deformation (Shoop and Alger 1998). Fukue (1979) reported similar observations in light snow (120 kg/m^3) as a function of penetration speed, as shown in Figure 32. This substantiates the use of the crushable foam model to represent fresh snow. However, dense or bonded snow does show lateral deformation (Shoop and Alger 1998), as does snow subjected to slow loading (Fukue 1979) (Fig. 32a).

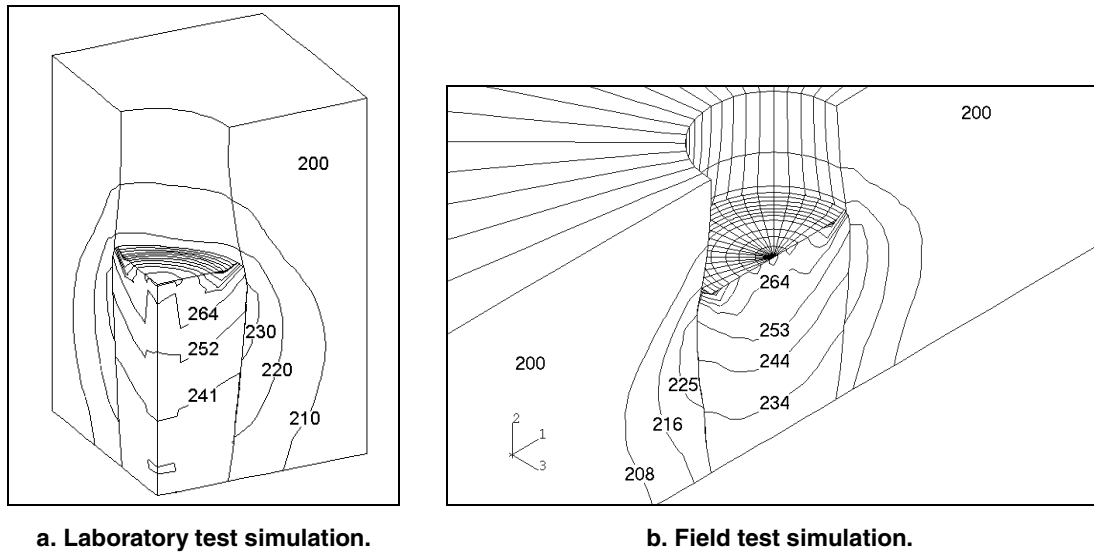


Figure 30. Modeled snow density (kg/m^3) for plate sinkage test for Drucker-Prager cap material.

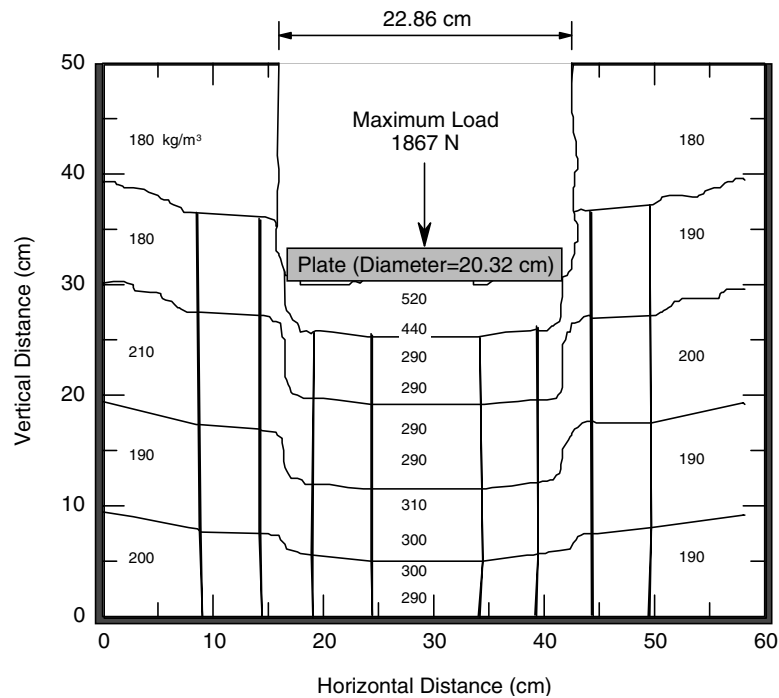
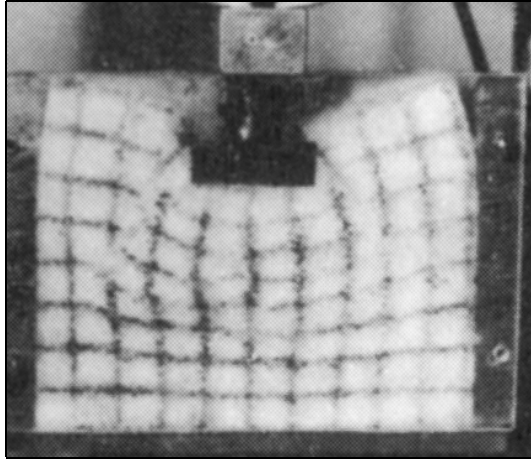
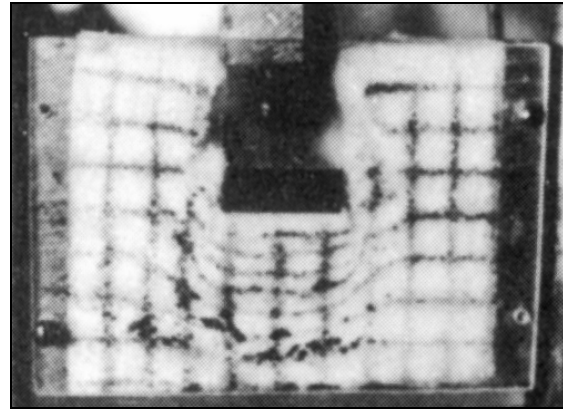


Figure 31. Measured displacement and snow density in laboratory plate sinkage test. (From Shoop and Alger 1998.)



a. At 0.097 mm/s.



b. At 0.98 mm/s.

Figure 32. Deformation of fresh snow under a plate. (From Fukue 1979.)

Soil model

The material model used for the wheel-on-soil simulation was also a Drucker–Prager cap plasticity model. Initially a very soft thawing soil was to be simulated, but the testing of the soil parameters became quite extensive and will be completed in the future. A compacted sand material called McCormick Ranch sand was used for initial modeling. McCormick Ranch sand is a clayey sand, classified as SC, from Albuquerque, New Mexico, and is similar in grain size distribution to the Lebanon sand used in mobility experiments on frozen and thawing soils at CRREL (Fig. 33). The McCormick Ranch sand was tested in a compacted state, whereas soils that have been subjected to freeze–thaw are usually loose

and wet. However, the compacted McCormick Ranch sand model is useful for simulating a vehicle on an unpaved secondary road under good (summer) road conditions.

The mechanical behavior of the McCormick Ranch sand was documented by Mazanti and Holland (1970a, 1970b), and material parameters for a modified Drucker–Prager cap model were developed in DiMaggio and Sandler (1971) and implemented in ABAQUS (HKS 1996). The material parameters are given in Table 4, and the cap hardening–softening behavior is defined using the piecewise linear approach given in Table 5. The material model yields excellent comparison to uniaxial strain test results (Fig. 34).

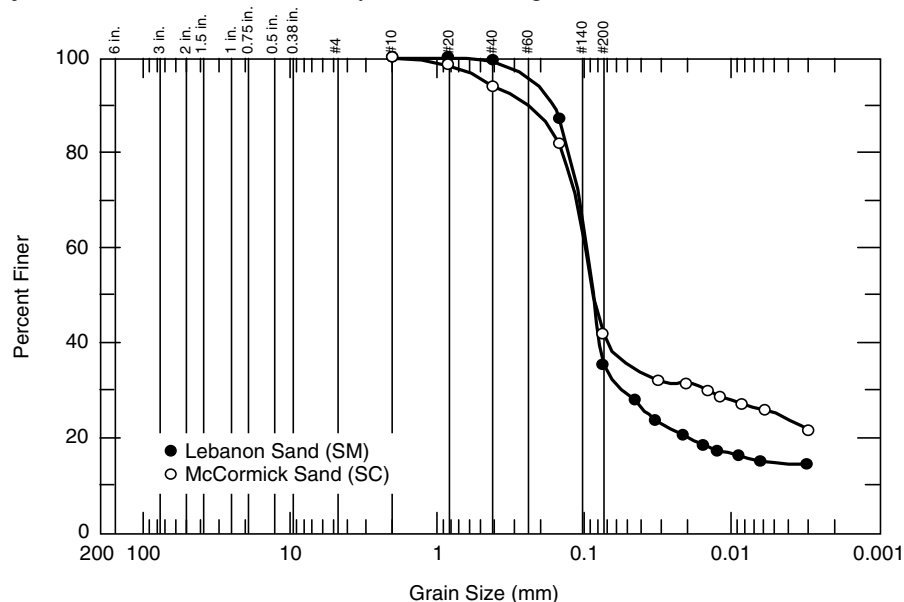


Figure 33. Grain size curves for McCormick Ranch sand (Mazanti and Holland 1970a) and Lebanon sand (Shoop 1990, 1993a).

Table 4. Material constants for Drucker–Prager cap model of McCormick Ranch sand (HKS 1996).

<i>Material parameter</i>	<i>Value</i>
Young's modulus, E	689 Mpa (100000 psi)
Poisson's ratio, ν	0.25
Drucker-Prager material angle of friction, β	14.56°
Drucker-Prager material cohesion, d	1.194 MPa (173.2 psi)
Cap eccentricity parameter, R	0.1
Initial value of volumetric plastic strain, $\varepsilon_{vol}^{pl} _0$	0.001
Flow stress ratio, K	1.0

Table 5. Hardening model for McCormick Ranch sand (HKS 1996).

<i>Hydrostatic stress, P_b (MPa)</i>	<i>Volumetric plastic strain, ε_{vol}^{pl}</i>
0.138	0
0.172	0.005
0.434	0.01
0.896	0.02
1.655	0.03
2.758	0.04
4.137	0.05
6.895	0.06
13.447	0.10

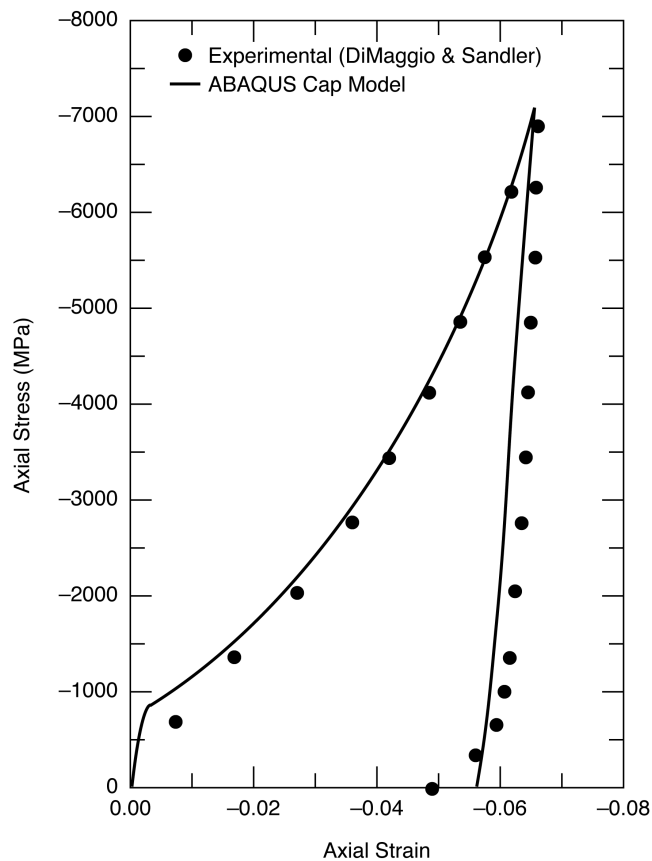


Figure 34. Validation of McCormick Ranch sand Drucker–Prager cap model with uniaxial strain test data from DiMaggio and Sandler (1976). (After HKS 1996.)

TIRE MODELS FOR A DEFORMABLE SUBSTRATE

Tire model construction

Background

To apply a tire model to deformable terrain, a model is needed that is efficient yet accurately portrays the tire structural behavior. Specifically, an accurate model of the contact patch is critical for simulating the impact of deformable terrain on tire performance. Models commonly used for tire design purposes very accurately predict deformation of the complete tire, including the interaction of the internal components. However, since our concern is only the deformation as it relates to the contact region and its ability to roll across a surface, simpler models can be employed for better computational efficiency. To this purpose, several tire models were evaluated for efficiency and comparison to measured tire mechanical response, particularly deformation and stress related to contact.

Modern tires are structurally complex, consisting of layers of belts, plies, and bead steel imbedded in rubber (Fig. 7). Materials are often anisotropic, and rubber compounds vary through the tire structure. Models developed for tire design are extremely detailed, modeling each material within the tire (belts, plies, rubber) for internal tire stress analysis, wear, and vibration modal analysis. For these types of models, the tire may consist of shell, continuum, and rebar elements. The simulation consists of mounting the tire on the rim, inflating it, lowering the tire onto a rigid surface, and applying various loading conditions. Such models are extremely large and take many hours to run. The tire properties and associated modeling details for tire models used by industry are extremely difficult to obtain. Among the more notable published contributions to tire modeling are numerous publications by Joseph Padovan at the University of Akron (Padovan 1977, Padovan et. al 1992, Padovan and Padovan 1993, 1994a, 1994b) and models of agricultural tires by Hu and Abeels (1994). An example of such a model is the National Tire Modeling Program (NTMP) radial automobile tire shown in Figure 35. The NTMP is a generic model used for calibrating modeling programs across the tire industry. Prior to 1997 this type of model required over 15 CPU hours on a SUN SPARCstation 10 for inflation and no-slip contact on a rigid surface (i.e. no rolling).

In this research project, four types of tire models were evaluated for suitability to rolling on deformable terrain: 1) a rigid tire, 2) a simplified tire model

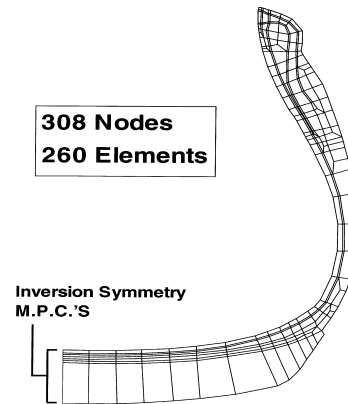


Figure 35. National Tire Modeling Program (NTMP) model of a radial tire. (After Danielson and Noor 1997.)

using methodology developed by Darnell at the University of Michigan for use in vehicle dynamics, 3) a tire model of the type used for harmonic vibration modal analysis, with a smooth tread, and 4) a tire model similar to model 3 except with a straight (longitudinal) ribbed tread. The modal analysis models were provided by Goodyear through a Cooperative Research and Development Agreement and required only minor modifications to accommodate surface contact and rolling. All of the models were built to represent the tires used in the experimental test program for comparison to measured tire behavior in terms of deflection, contact area, deflected sidewall profile, contact stress distribution, and performance on deformable terrain (snow and soil).

Tires simulated

Three tires were involved in the data collection phase of the project. The first tire was a Michelin XCH4 235/75 R15. This tire was used in several experiments on snow and soil under various moisture, compaction, and temperature conditions. The second tire, a Goodyear Wrangler AT 235/75 R15, was chosen to be similar to the first in construction and behavior. The third was a highway tire with a ribbed tread pattern, the Goodyear Wrangler HT 235/75 R15. The three tires were similar in size, construction, deflection, and contact area characteristics, and data from all three were used in the following comparisons. Although the tread patterns and compounds varied (Fig. 36), which would strongly influence traction, this study focused on the tire deformation and rolling resistance, so the tires can be considered equivalent. The dimensions of the test tires are given in Table 6.



Figure 36. Tires used in the experiments: Goodyear Wrangler HT, Michelin XCH4, and Goodyear Wrangler AT.

Table 6. Tire characteristics for the test tires at an average vertical load of 6227 N (1400 lb). The XCH4 tire data were used to represent the average values.

<i>Inflation pressure</i>		<i>Contact area (cm²)</i>	<i>Deflection</i>		<i>Max. deflected section width (cm)</i>
<i>(kPa)</i>	<i>(psi)</i>		<i>(cm)</i>	<i>(%)</i>	
103	8	509.7	6.3	38	27.9
138	15	419.4	5.4	33	25.9
179	26	364.5	4.6	28	26.0
241	35	281.7	3.1	19	25.1

Unloaded tire diameter: 73.7 cm

Unloaded section width: 22.9 cm

Unloaded section height: 16.4 cm

Tread width: 15.7 cm

Ratio of voids to tread contact area: 0.44

Inflated overall section width: 24.9 cm

Inflated diameter: 74.7 to 75.3 cm

All three tires were evaluated for their deformation characteristics on a rigid surface. A comparison of the deflection and contact area measurements collected from various sources is given in Figures 37 and 38. All of the data were collected after a tire break-in period of operation of at least 160 km. Contact area is calculated from a static contact “perimeter” area without accounting for voids due to tread pattern so that comparisons can easily be made be-

tween the different tires and models. Based on the good match in the measured tire deformations on a rigid surface (deflection and contact area), the tires were assumed to be sufficiently similar for interchangeable use in comparing to model results. The normal operating pressure for the tires is 241 kPa (35 psi), and that is where the similarity between models and data is best.

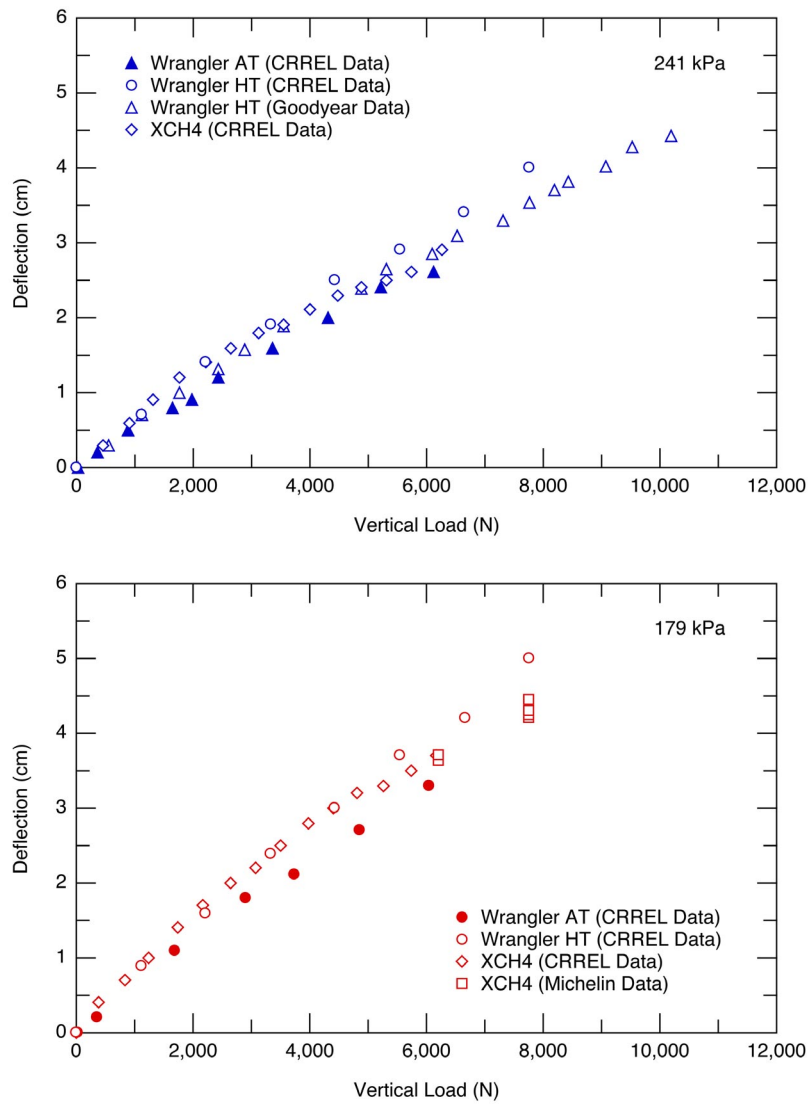


Figure 37. Deflection measurements for the tires used in the experiments at inflation pressures of 241 kPa (35 psi) and 179 kPa (26 psi).

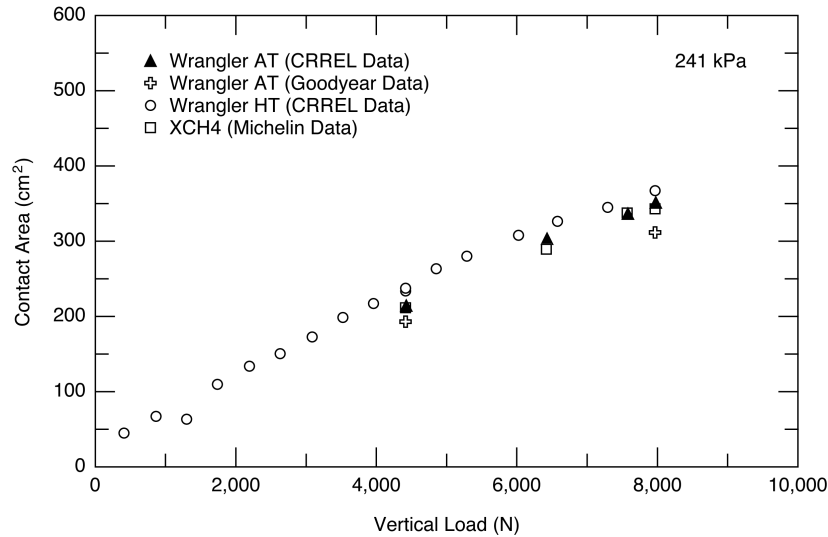


Figure 38. Comparison of measured contact area for the three test tires at 241 kPa (35 psi).

Rigid tire model

If the deformable material is very soft, as in fresh snow, the tire can be approximated as a rigid wheel. The rigid wheel is modeled as a rigid analytical surface 0.74 m in diameter and 0.272 m wide (for a full wheel), with a 0.051-m radius of curvature on the tire shoulder. An unsprung mass of 636 kg is placed at the axle to simulate the weight of the tire and the load of the vehicle on the tire (6240 N); the rotational inertia of the wheel was set to 2.15 kg m².

Darnell tire model

To adequately model the dynamics of a rolling tire, a very efficient tire model is needed. Thus, the tire model developed by Darnell and Hulbert at the University of Michigan is a promising alternative. The Darnell tire model (Darnell et al. 1997, Darnell, in progress) is an extension of a two-dimensional tire modeling concept developed by Mousseau (Mousseau and Hulbert 1996) for interfacing with vehicle dynamics simulations. The tire is modeled using material properties for the composite material rather than the individual components. The composite properties were obtained by sectioning the tire and performing laboratory tests on each of the major section components (tread, sidewall, and shoulder). A similar approach was also developed at the University of Birmingham in the UK for tire modal analysis (Burke and Olatunbosun 1997a, 1997b, 1997c). Additional work on the Darnell model has been toward paramet-

ric analysis and refinement of the code (Alvarez Sanz 1999).

The objectives of the Darnell tire model are similar to those needed for this study: an efficient, accurate, three-dimensional model to predict spindle (axle) forces but not the internal stresses in the tire. The contact forces are calculated in the process, so the model is also suitable for efficient modeling of the tire-terrain interaction, where accurate modeling of the contact stress distribution is imperative.

The tire is simulated with three modeling elements: the tread elements are six-degree-of-freedom shell elements (S4R); the sidewall elements are three-node, user-defined elements based on pre-calculated results from a sidewall model; and the contact is modeled using a “hard” contact, penalty method (HKS 1998). The roadway is modeled as a rigid surface.

The sidewall model is a special-purpose finite element code that generates a lookup table of sidewall forces (and geometry) using ten equal-length, non-extensible beam elements with inflation pressure as a follower load. The sidewall model is generated from the geometry of the uninflated sidewall, the bending and shear stiffness for each element, and the tire inflation pressure. The results of the sidewall model are implemented in the tire model through the user-defined element, which attaches to the tread section with rotational springs (Fig. 39).

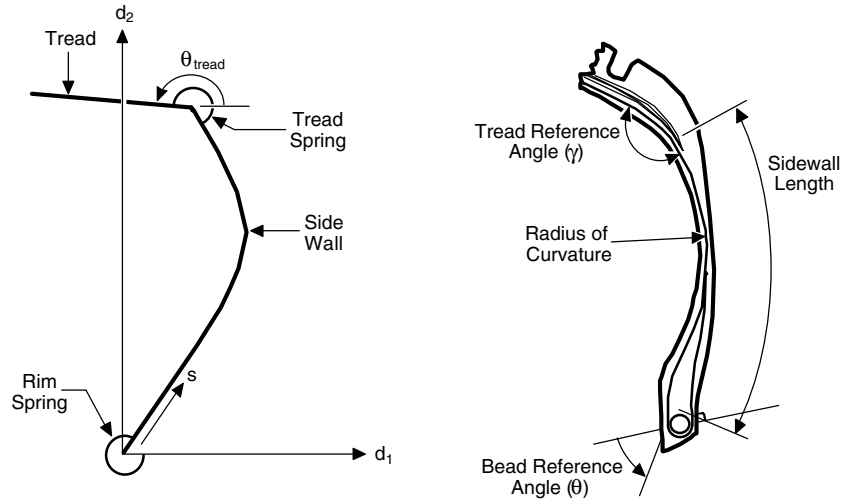


Figure 39. Construction elements of the Darnell tire model. (After Darnell et al. 1997.)

The Darnell tire model was validated for a Ford Taurus tire for lateral forces and deflection on a smooth surface and while rolling over an angled vertical step (Darnell et al. 1997) and for slip angle and aligning moment.* The model results sufficiently mimic tire behavior while being computationally efficient, indicating its potential for simulations of a tire on deformable terrain. Some alteration in the sidewall model may be necessary to account for the interaction of the sidewall with the deformable terrain if sinkage is substantial.

The same tire used to gather motion resistance data on various terrain (snow, freezing and thawing ground) was cut into four sections: sidewall, lateral tread, longitudinal tread, and shoulder (Fig. 40). The sidewall was further dissected into smaller sections for future work expanding the sidewall model. The sections were tested in the laboratory to determine the beam stiffness (EI) by clamping an end of the test section onto a workbench to form a cantilever beam. Deflections were measured for a range of loads, and stiffness was calculated using the equation for a cantilever beam with a point load on the free end:

$$y_{\max} = \frac{1}{3} \frac{Wl^3}{EI} \quad (25)$$

where y_{\max} = maximum deflection at the free end of the beam
 W = applied load
 E = Young's modulus of the beam

* Personal communication with I. Darnell, University of Michigan, 1997.



Figure 40. Cut tire sections used to determine composite tire properties.

I = moment of inertia
 l = beam length.

Young's modulus (E) is calculated from EI using $I = w_{\text{beam}} t_{\text{beam}}^3 / 12$, where w_{beam} and t_{beam} are the width and thickness of the tire samples, respectively. The test results are summarized in Table 7.

The sidewall was divided into ten equal-length beam elements in a special-purpose finite element code. This code generates the sidewall force and geometry table for the user-defined element representing the sidewall in the tire model. The stiffness and curvature of the sidewall model are given in Table 8 and illustrated in Figure 41.

Additional measurements needed for the model are sidewall curvature, tread hoop stiffness, rotational spring constants, reference angles, tire and rim geo-

Table 7. Bending stiffness of tire sections.

	Width (cm)	Length (cm)	Thickness (cm)	EI ($N\ m^2$)
Sidewall section A1	5.2	3.3	1.3	0.1564
Sidewall section A2	5.2	2.0	1.3	0.0287
Sidewall section A1+A2	5.2	5.3	1.3	0.1521
Sidewall section B	5.8	6.1	0.6	0.0459
Sidewall section C	7.0	2.1	1.1	0.0172
Lateral tread section	7.0	16.5*	1.7	0.1550
			(0.9 w/o tread)	
Longitudinal tread section	12.5	27.2	1.7	0.5137
			(0.9 w/o tread)	
Shoulder		33.5 cm along tread		

* 23.4 cm including shoulders

Table 8. Properties of sidewall elements and tire model components.

Element	Curvature (1/m)	Stiffness per unit width (N m)
1 (Bead end)	0.01	2 (rigid)
2	6.76	1.5
3	7.63	0.15
4	9.95	0.04
5	8.62	0.04
6	9.71	0.04
7	9.01	0.04
8	9.09	0.15
9	14.49	0.5
10 (Tread end)	17.54	1.0

Total length of sidewall = 16.1 cm, each element $L = 1.6$ cm

Tread attachment angle = 133°

Rim attachment angle = 23°

Tread diameter to end of last sidewall element = 72.5 cm

Tread diameter to center of belts = 69.5 cm

Rim diameter to first sidewall element = 41.6 cm

Tread longitudinal shell flexural rigidity for unit section width, $E_1 I = 4.1261\ N m^2$

For 1.11-mm shell thickness, $E_1 = 3.62 \times 10^{10}\ N/m^2$

Tread lateral shell flexural rigidity for a unit section width, $E_2 I = 2.259\ N m^2$

For 1.11-mm shell thickness, $E_2 = 1.98 \times 10^{10}\ N/m^2$

metry, and sidewall and shoulder stiffness. These are listed at the bottom of Table 8.

For the elements representing the tread, the shell stiffness was calculated with E_1 being along the tread in the longitudinal direction and E_2 being across the tread in the lateral direction. An equivalent shell thickness of 1.11 mm was used in the model since this was found to yield a reasonable hoop stiffness based on measured changes in circumference with inflation pressure.*

* Personal communication with I. Darnell, University of Michigan, 2000.

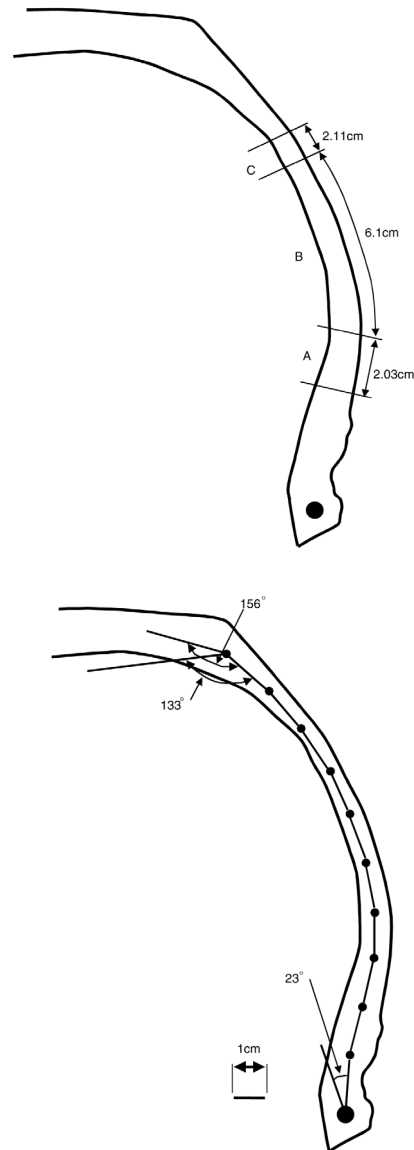
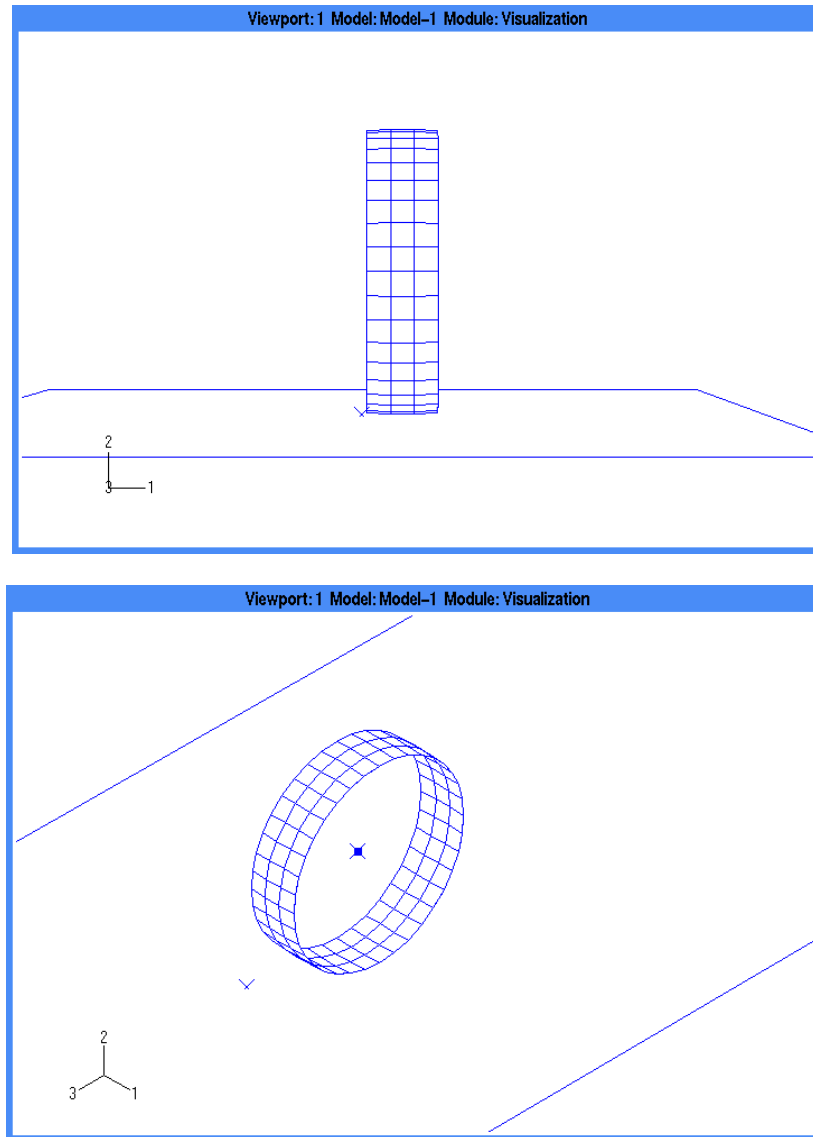


Figure 41. Tire geometric parameters for the sidewall model.



a. Coarse (3×36) mesh.

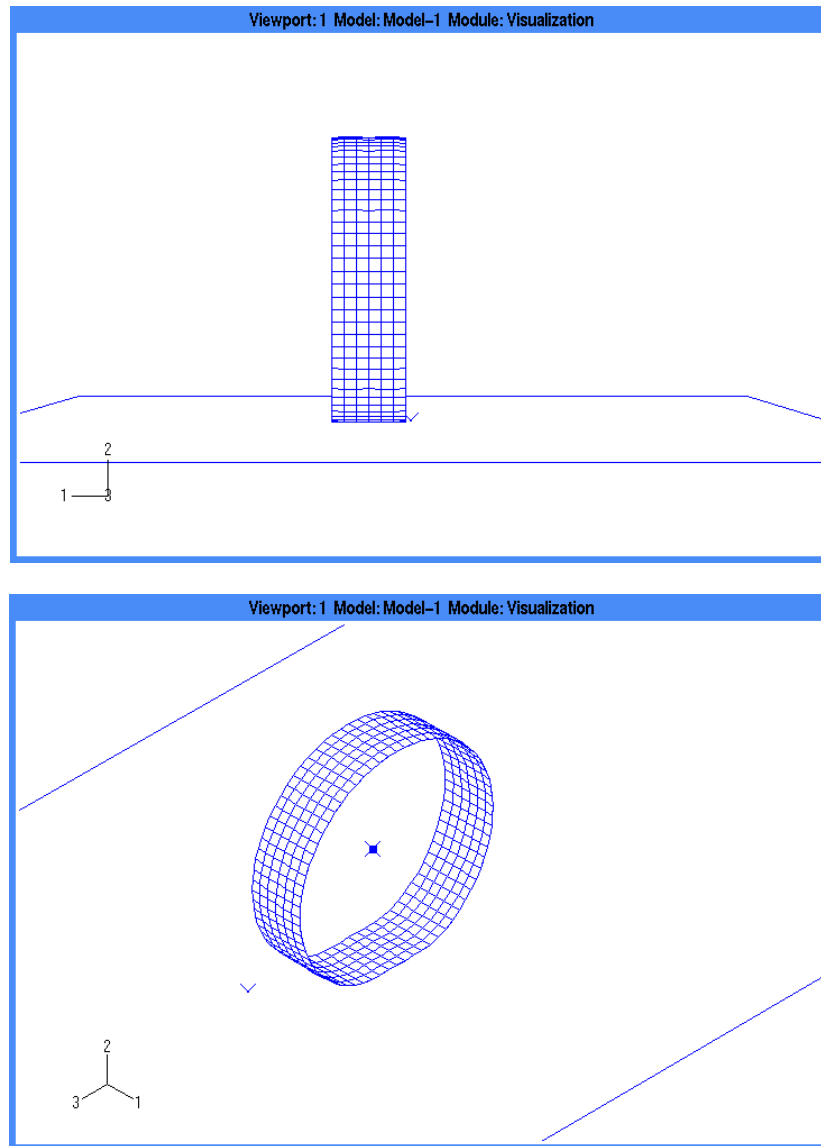
Figure 42. Shoop–Darnell tire model (user elements not shown).

The Shoop–Darnell model (the model of the test tire created with the Darnell methodology) was constructed using ABAQUS for a quasi-static simulation. This adequately simulates low-speed vehicle travel and is appropriate for 5 mph, which is the standard test speed for off-road traction and motion resistance testing. The tire model is first subjected to internal pressure (inflated), then lowered onto the surface and allowed to equilibrate with the applied vertical load before rolling. The Darnell methodology for the tire model was validated for the test tire on a hard surface and then used to simulate the three-dimensional contact between two deformable bodies on a homogeneous terrain, first using an elastic terrain model and

then a plasticity model for the terrain material. Two Shoop–Darnell mesh configurations were used in the analysis: a coarse and a fine mesh (Fig. 42). Since the sidewalls are modeled with user-defined elements, they do not appear on the standard finite element visualization.

Modal analysis tire model: Smooth tread

The smooth tread tire model is typical of the type of models used for tire vibration modal analysis. The carcass is composed of a single layer of four-node, reduced-integration shell elements (S4R) with material properties representing the composite behavior through the carcass thickness. The treadcap is con-



b. Fine (6×72) mesh.

Figure 42 (cont.). Shoop-Darnell tire model.

structed of linear, hybrid continuum elements (C3D8H), with constant pressure (simulating the nearly incompressible nature of rubber). The result is a reasonable approximation of both the structural behavior and the contact patch. The model is constructed using the cross section shown in Figure 43, repeated every three degrees around the axis of the hub (creating 120 cross sections). For most of the simulations the tire model was cut in half using a vertical symmetry plane along the longitudinal axis. The wheel mass is represented by one mass element and one rotary inertia element located at the wheel's centerpoint on the symmetry plane.

The analysis is done in three steps: inflating the tire to the desired pressure, vertically loading it based on the vehicle's weight, and rolling it along the road by translating its centerpoint while allowing free rotation about its axis. The creation and seating of the bead are accomplished by multi-point constraint and fixed displacement of the first four rings of nodes closest to the wheel rim. During the inflation and loading steps, no friction is included on the contact surface. Variations of the analysis include a static rolling step, a dynamic rolling step, and changes in the definition of the shell element local coordinate system.

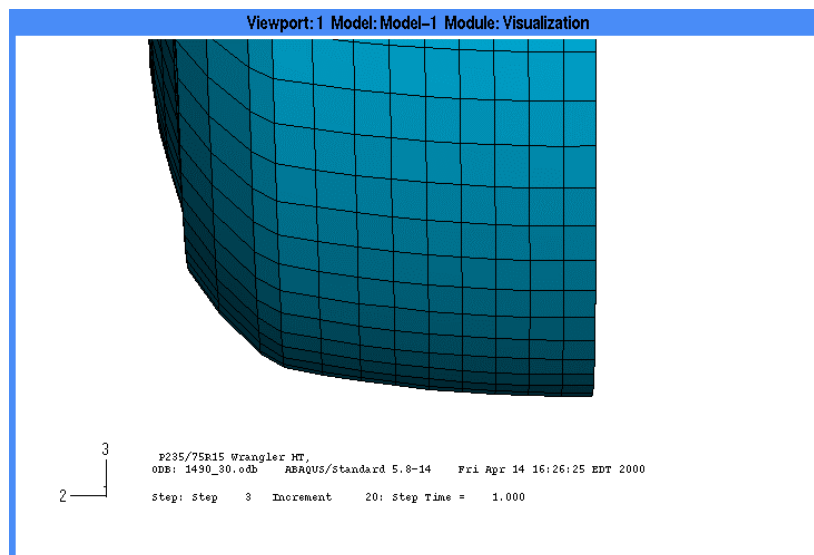
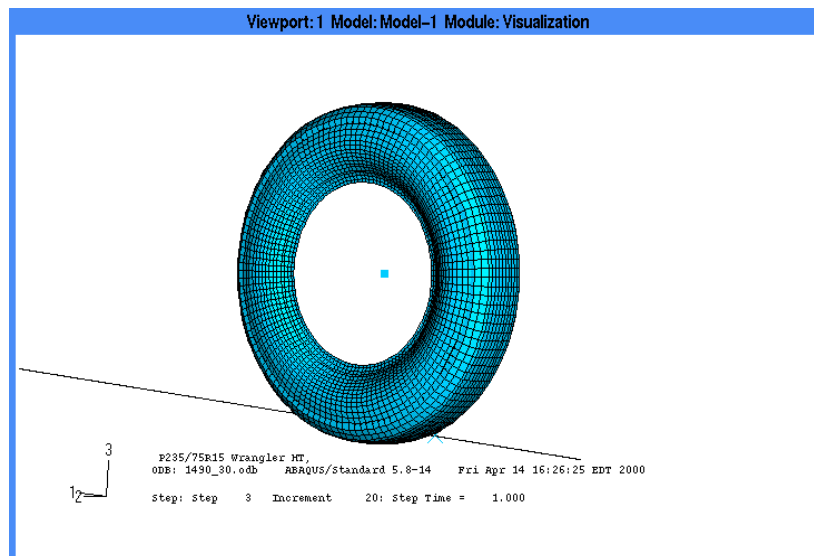
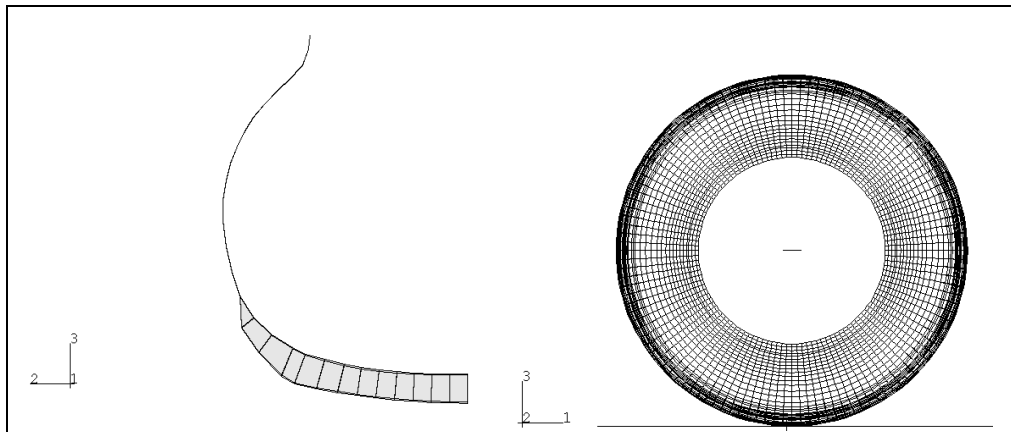


Figure 43. Modal analysis tire model with smooth tread.

Modal analysis tire model: Straight ribbed tread

The ribbed tread tire model is also a modal analysis tire model. Construction is similar to the smooth tread model, with the carcass composed of four-node reduced-integration shell elements and the treadcap constructed of linear, hybrid continuum elements with constant pressure. The major difference is the four grooves across the width of the tire created by omitting sections of the tread continuum elements (Fig. 44). The wheel is represented by one mass element and one rotary inertia element located at the centerpoint. Details for the smooth and ribbed tread models are given in Table 9.

The analysis is completed in eleven steps, comprising inflation, bead seating, lowering to the road surface, and vertical loading. The loading occurs in eight steps of alternating loose and tight convergence control. Inflation is handled similarly. The creation and seating of the bead are accomplished using multi-point constraints on the first five rings of nodes closest to the wheel rim. An additional step translates the

wheel's centerpoint while allowing the tire to freely rotate about its axis due to friction, simulating a towed wheel. The contact is frictionless during the loading process, and friction is added during the rolling step. Variations of the analysis include a static or dynamic analysis procedure during rolling and changes in the convergence controls.

The towing phase of the dynamic analysis is broken into two steps. The first is to accelerate the tire from rest to 1 m/s at a constant acceleration of 1 m/s^2 for one second (traversing 500 mm). The second step continues to roll the tire at a constant velocity of 1 m/s for two more seconds (2000 mm). For all cases the analyses converge for a while but eventually reach a point where the tire stops moving by taking increasingly smaller time steps due to convergence difficulties. The problem occurs when the shell is subjected to simultaneous distortion and rotation as the rotation angle approaches 360° . This is a bug in the ABAQUS shell element that will be corrected in future versions (Bug Report v58_2449).

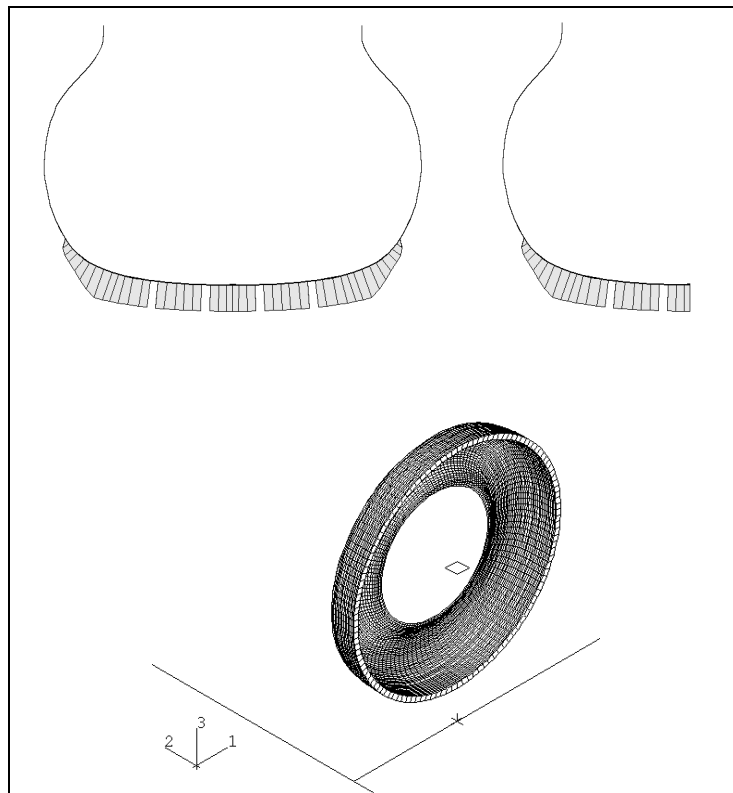


Figure 44. Modal analysis tire model with ribbed tread.

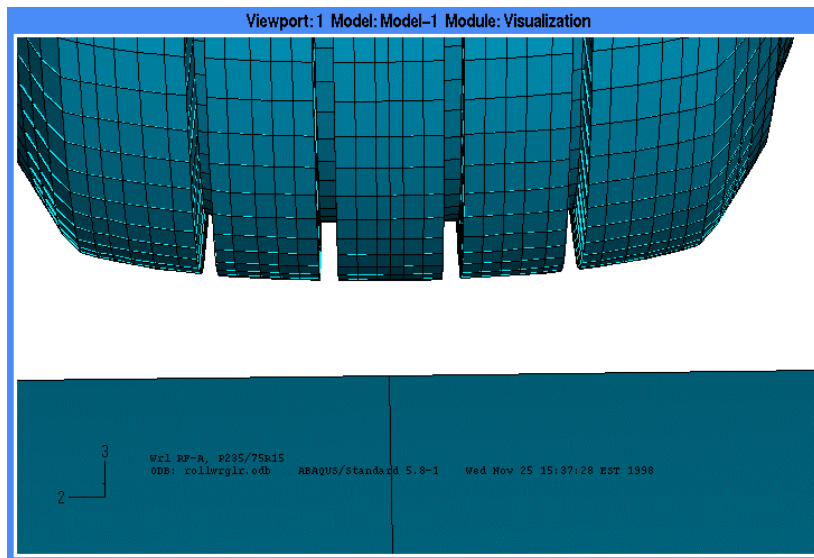
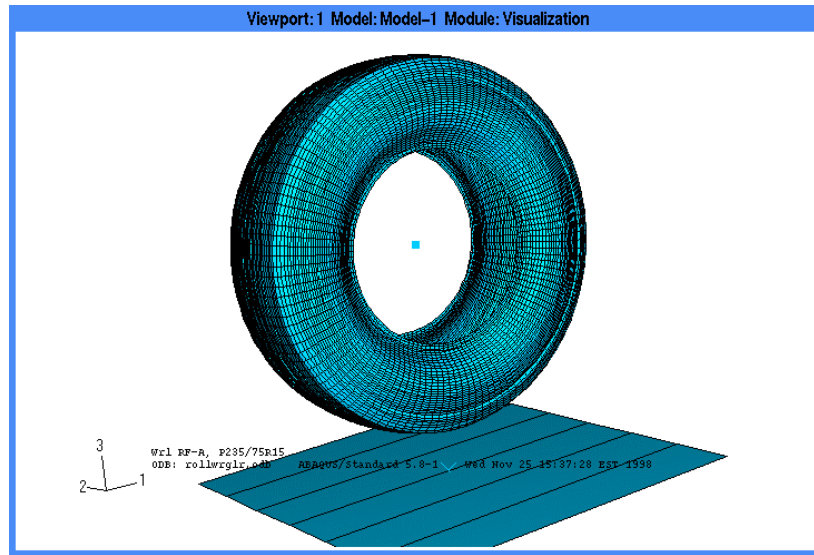


Figure 44 (cont.). Modal analysis tire model with ribbed tread.

Table 9. Features of the modal analysis models with smooth and straight ribbed tread.

	<i>Smooth tread Half carcass model</i>	<i>Straight ribbed tread Half carcass model</i>
Carcass elements (number and type)	3360 S4R	6240 S4R
Treadcap elements (number and type)	1440 C3D8H 120 C3D6H	2400 C3D8H 120 C3D6H
Tread rubber: neo-Hookean, C_{10}	1.109596	2.408340
Tread density (Ns^2/mm^4)	0.814575E-9	6.6255E-10
Tread gaps (width x depth, mm)	None	5.1 × 16.6 5.3 × 16.2
Total no. elements	6602	13562
Total model variables	32172	63396

Evaluation of tire models on a rigid surface

The tire models were applied to a rigid surface through a range of pressures and loads for comparison to measured deflections, contact patch areas, dimensions, and stresses.

Deflection

A complete data set for deflection was gathered for the Wrangler AT (Fig. 45) for use in comparisons with model results from the Shoop–Darnell model, the smooth tread model, and the ribbed tread model. Each model was loaded at a range of vertical loads (from 0 to 8000 N) at three tire inflation pressures:

241 kPa (35 psi), 179 kPa (26 psi), and 103 kPa (15 psi). The suggested inflation pressure for these tires is 241 kPa. Lower inflation pressures are sometimes used when driving in off-road and marginal road conditions (snow and soft soil) and for minimizing damage to unpaved travel surfaces. Therefore, the two lower inflation pressures were also evaluated. Performance at a range of inflation pressures is also of interest to industries using vehicles with Central Tire Inflation Systems (CTIS) (i.e. military, forestry, and agriculture).

A compilation of the data and model results for each inflation pressure is shown in Figure 46. The

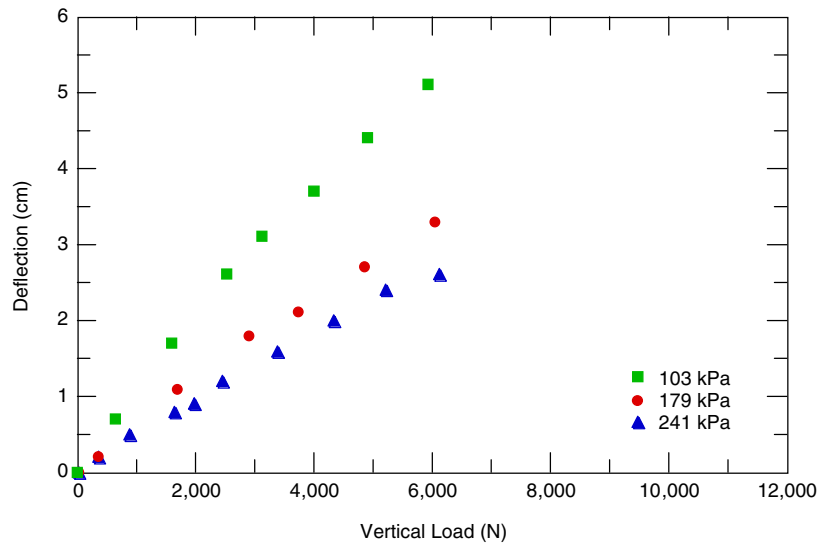


Figure 45. Measured deflection for three tire pressures.

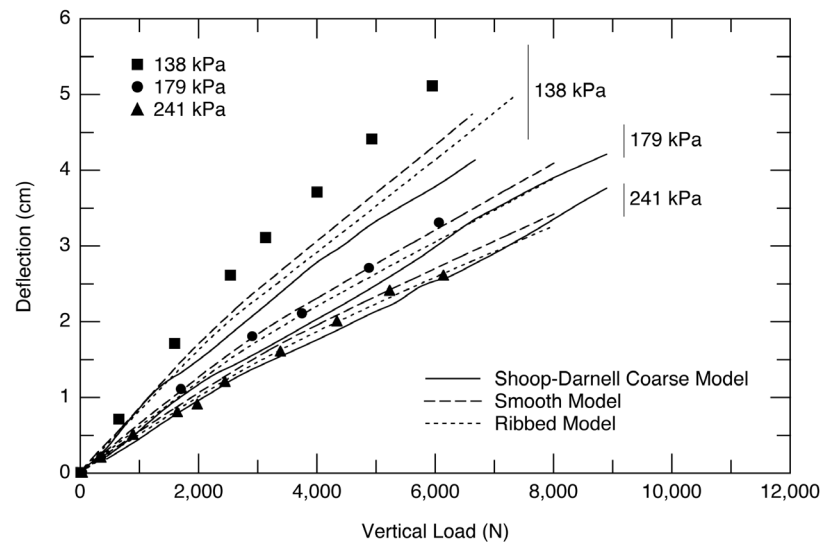


Figure 46. Comparison of measured and modeled deflection for the Shoop–Darnell, smooth tread, and ribbed tread models for three inflation pressures.

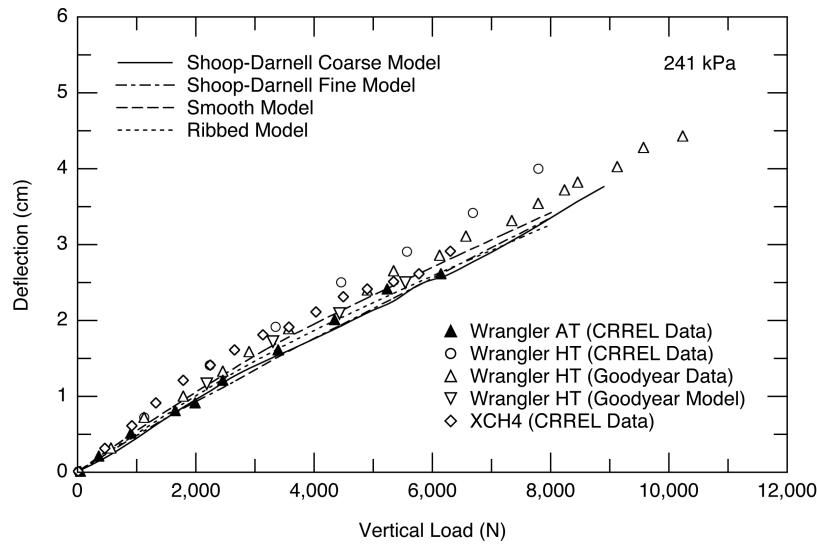


Figure 47. Comparison of all measured and modeled deflections at 241 kPa (35 psi) inflation pressure.

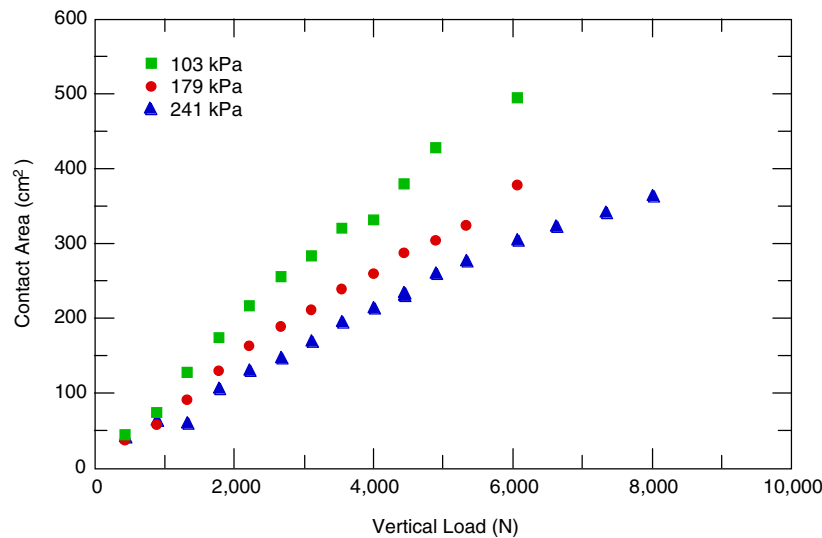


Figure 48. Measured contact areas at three inflation pressures.

model predictions follow the same general trend as the data for all tire pressures, with the largest difference occurring at the lower inflation pressure. This is understandable since undesirable tread and sidewall behavior can occur when tires are underinflated, and these pressures and behaviors are neither within the design range nor accurately accounted for in the models. On the other hand, the agreement between data and models at the standard inflation pressure is exceptionally good, as illustrated in more detail in Figure 47, showing all measured and modeled deflections at 241 kPa.

Contact area

Comparisons of contact area were done much the same as the deflection comparisons. The measured

contact areas for the three inflation pressures are given in Figure 48. All contact areas are based on the perimeter of the contact, without accounting for voids within the area due to tread design. Comparisons of the model results (the Shoop–Darnell model with both coarse and fine mesh, the smooth tread model, and the ribbed tread model) with measured data are shown in Figure 49.

In general, the agreement between the models and data is reasonable. Surprisingly the Darnell gives the best fit, but the model mesh is coarse, which makes the results erratic since the contact area changes abruptly as each shell element makes contact. The refined mesh on the Darnell model is only a slight improvement, and the results are worse at the higher loads where the contact nodes pop off the surface just

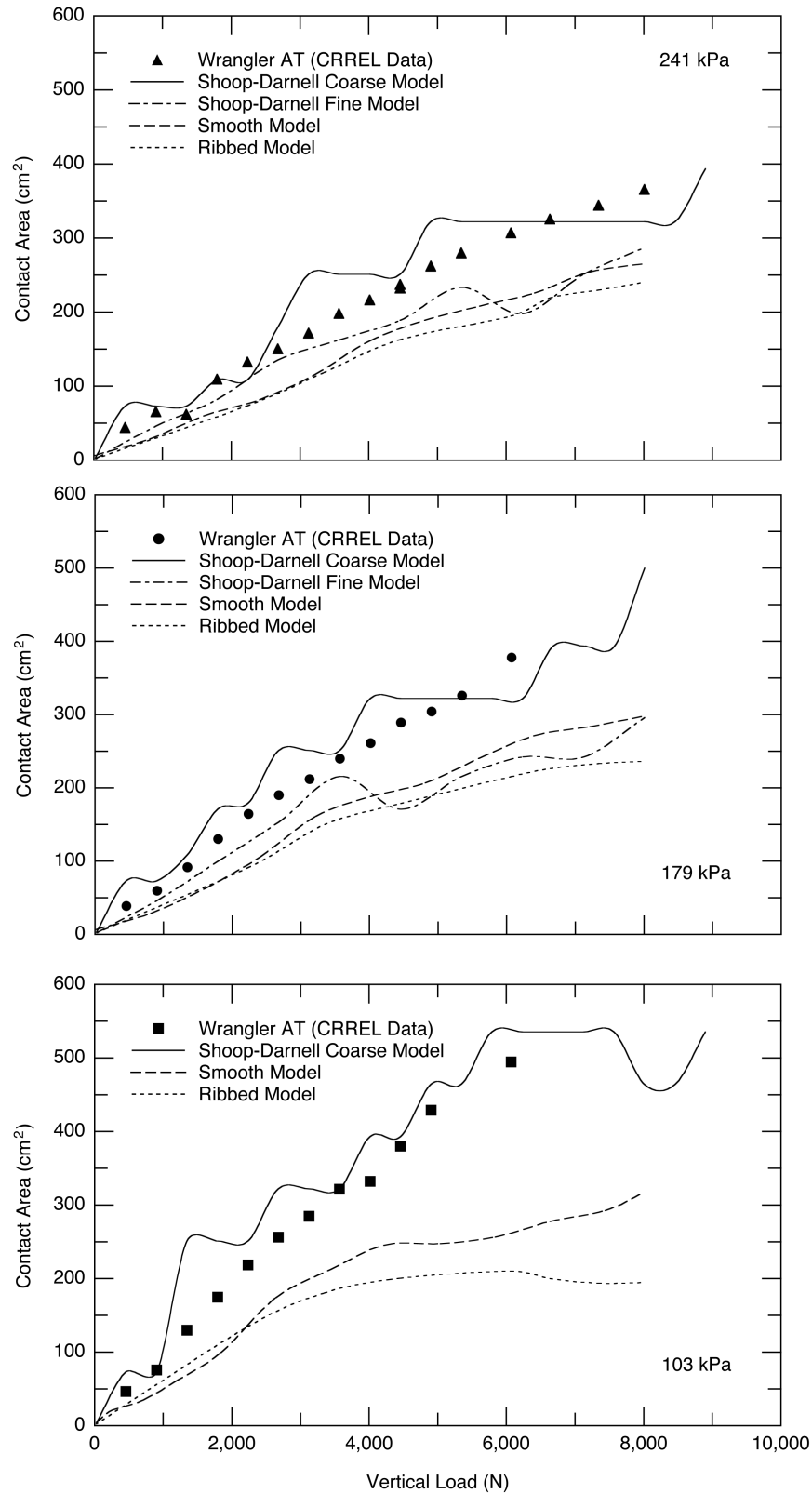


Figure 49. Comparison of measured and modeled contact areas at three inflation pressures.

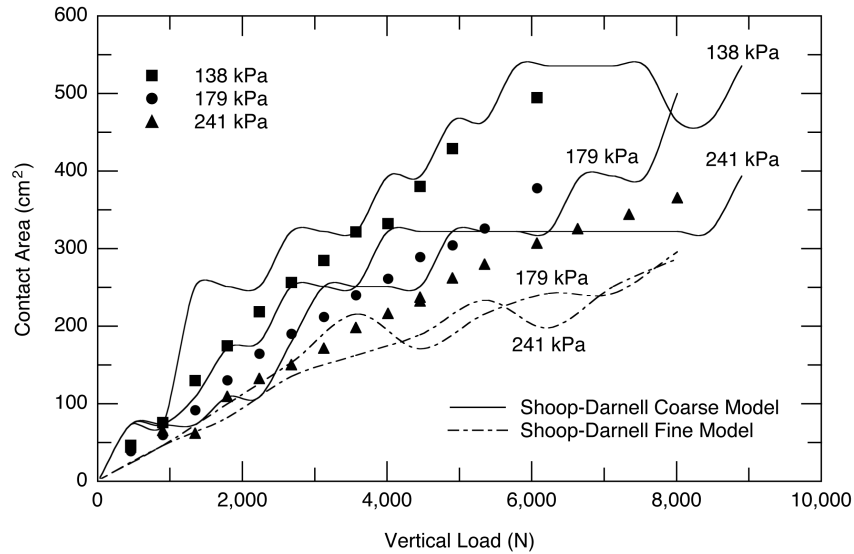


Figure 50. Comparison of Shoop-Darnell model results with measured contact areas (for coarse and fine meshes).

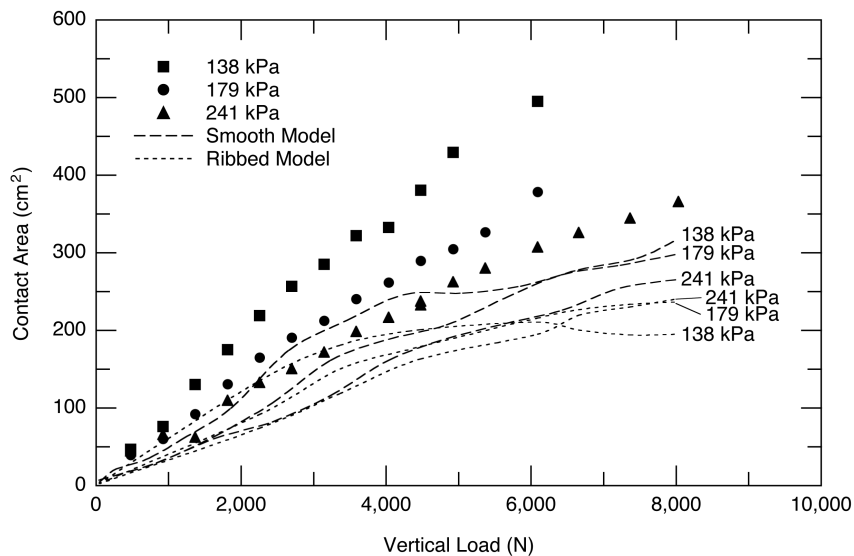


Figure 51. Comparison of the smooth and ribbed modal analysis tire models with measured contact areas.

inside of the tire shoulder due to buckling of the carcass (as discussed later). This behavior strongly affects the contact stress and area since adjacent nodes may alternate between high loads and no contact. Figure 50 compares the Shoop-Darnell models to the measured data.

Comparisons of the smooth and ribbed tread modal analysis models to measured data are shown in Figure 51. Both models provide contact areas less than the measured data at the high loads, indicating that the models are slightly stiff. The ribbed model

contact area is slightly less than the smooth model, even after being corrected for the tread voids.

Contact stress distribution

Contact stress measurements for the Wrangler HT were provided by Goodyear. For comparison, the modeled contact stresses were displayed at the same contour levels and color scheme, as shown in Figure 52. Both models and measurements show high stress values at the tire shoulder and, to a lesser extent, along the tire centerline. Agreement with the measured contact stress distribution is excellent.

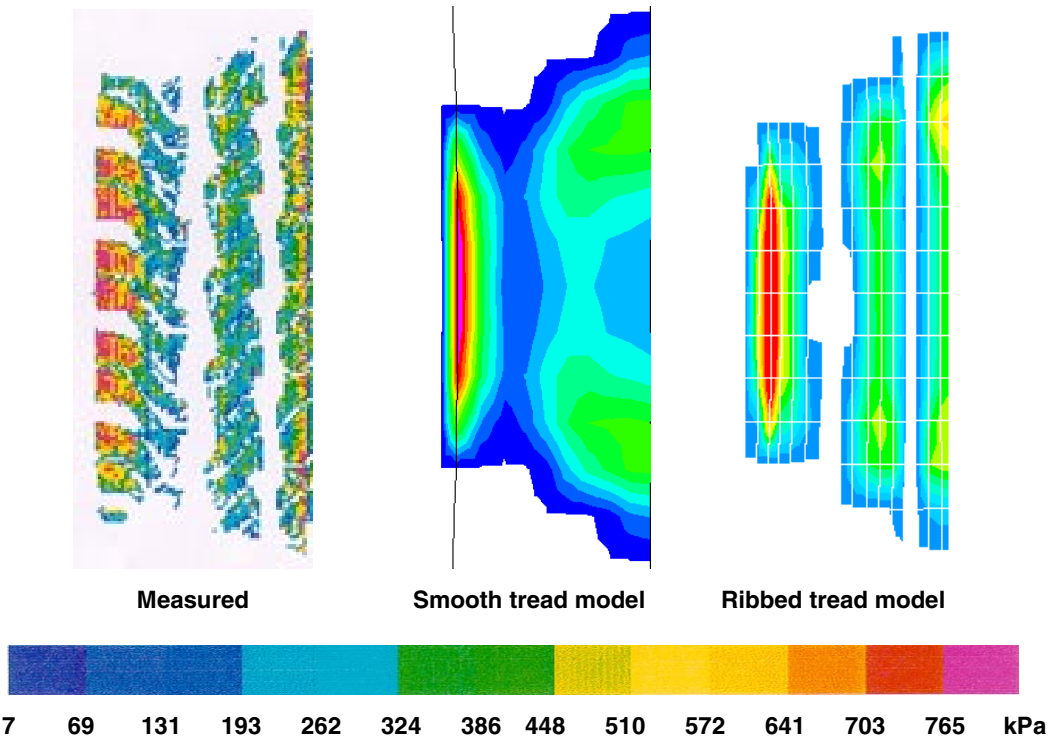


Figure 52. Measured and modeled contact stress distribution for half carcass on a hard surface (207 kPa inflation and 6627 N load).

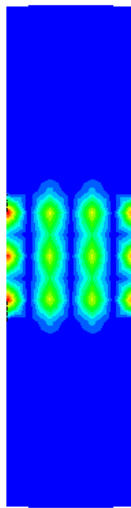


Figure 53. Irregular stress contours generated by the Shoop–Darnell model on a rigid surface (full carcass width).

During contact on a rigid surface, the Shoop–Darnell model suffered from buckling just inside the tire shoulder area, which strongly affected the contact stress. Although a finer mesh would normally smooth the contact stress contours, the buckling causes alternate nodes to lift off the surface, resulting in the stress pattern shown in Figure 53. Eventually, pro-

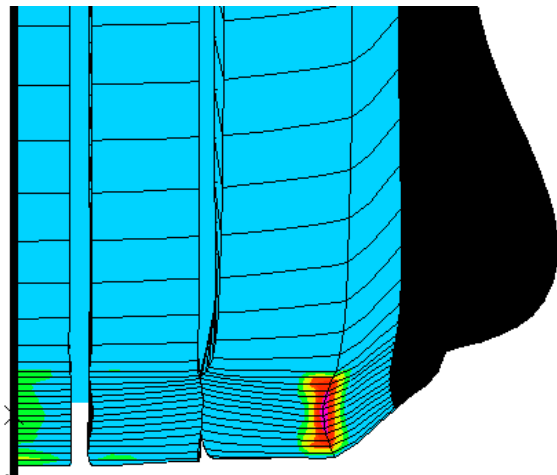


Figure 54. Close-up view of the contact for the ribbed tire model, showing buckling just inside the shoulder area (half tire carcass).

gressively finer meshes fail to converge [similar behavior was noted and explored by Alvarez Sanz (1999)]. The buckling behavior also occurs to a limited extent in the physical tire and in the modal analysis tire models (seen in the contours in Figure 52). The buckling is worse at low inflation pressures and high loads (Fig. 54). The impact is minor for the

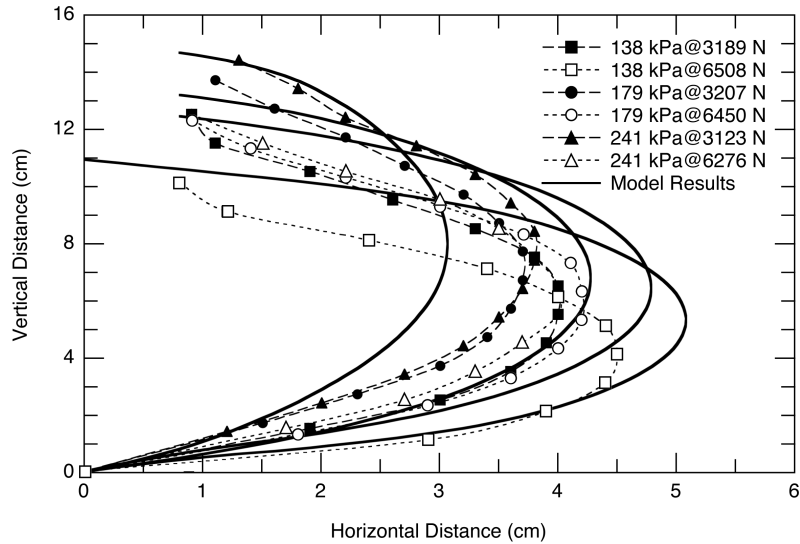


Figure 55. Measured and modeled sidewall profiles for the Shoop–Darnell tire model.

actual tires and the models where the rubber tread elements conform to the surface, softening the contact. For our purposes, this behavior disappears when the tire model is applied to a terrain surface, which softens the contact through terrain compliance.

Sidewall profile

Measurements of the deflected shape of the sidewall under various loads and inflation pressures were collected to check the calibration of the Shoop–Darnell tire sidewall model. Selected measurements of the profiles, along with comparisons to the modeled geometry, are given in Figure 55. The modeled sidewall geometry closely duplicates the measured geometry. The modeled sidewall is slightly longer than the measured profiles since the measurements did not include the sidewall portion covered by the wheel rim.

Hard-surface rolling resistance

Ideally forces generated from rolling the model should be comparable to the measured hard-surface rolling resistance. However, rolling resistance is largely due to viscoelastic behavior in the rubber compounds, and these models omit the viscoelastic material properties for increased efficiency. Therefore, the modeled hard-surface rolling resistance forces reflect only resistance due to interface shear. For an interface friction coefficient of 0.825, similar to asphalt pavement, the rolling forces modeled are less than 10 N at an inflation pressure of 241 kPa, while measured values are on the order of 25 N [at 241 kPa and low speed (8 kph)].

Run times

Model efficiency is of primary importance for use in rolling a tire on a deformable material, so the models were run with various options and using different computers in order to assess the effects on run time. The primary variables considered were the effect of the tread (smooth vs. ribbed), static or dynamic analysis, convergence controls, optimum use of symmetry, and computing system. The results of the many runs are included in the following discussions and qualitatively summarized in Table 10. Examples of some of the run times are given at the bottom of the table. Consideration was also given to how far the tire would roll in the model run. A roll distance of between one third and two revolutions, depending on the tire, is needed to remove abnormal stresses built up in the tire structure due to lowering it onto the surface. One revolution was considered the minimum requirement. All comparison simulations were done using the implicit solver.

Static vs. dynamic. The static models were run in a steady-state type of analysis. The same models were modified for a dynamic analysis where the inertia of the system is considered. In general, the static models roll over twenty times farther in less than twice the CPU time than the dynamic models. However, the dynamic models used less memory. Ultimately, a dynamic model is the desired choice to include mass, velocity, and acceleration effects and for operating the combined model using an explicit finite element code.

Full tire vs. half-tire. The full-tire version of the ribbed model is prohibitively expensive in terms of

Table 10. Qualitative summary of runtime analysis.

<i>Model parameters compared</i>	<i>Change in performance</i>
Static vs. dynamic analysis	Static models rolled 2 m vs. 0.08 m before convergence problems
Half tire carcass vs. full tire carcass	Half tire runs three times faster
Smooth vs. ribbed tread model	Smooth model runs four times faster
SGI Octane vs. Cray J932	Octane is two to three times faster
Tight vs. loose convergence controls	Loose controls run faster but tight controls let the tire roll further before convergence problems
Example run times	
Ribbed tread, full tire, tight convergence	Rolls 25 mm in 488 hr on J932
Ribbed tread, half tire, dynamic analysis	Rolls 46 mm in 252 hr on J932
Smooth tread, half tire, static analysis	Rolls 2 m in 22 hr on Octane
Shoop–Darnell model (full tire)	Roll 20 m in 11 min on Octane

run time. It takes almost three times as long as the half-tire model to go the same distance. No full-tire model has stopped due to non-convergence, but rather due to system errors or time limits. In the future, if side forces, cornering forces, or steering reactions are investigated, then a full-tire model will be required.

Smooth tread vs. ribbed tread. The model with the smooth tread has fewer nodes and elements, is less geometrically complex, and uses default convergence controls. It runs more than four times faster than the ribbed tread model during the static analysis and more than eleven times faster for the dynamic analysis. In most instances the accuracy of the smooth model is as good as or better than the ribbed model (i.e. the model results are closer to the experimental data). In the dynamic analyses the smooth tread model went almost twice as far as the ribbed tread model.

Cray J932 vs. SGI octane. The models are being run on an SGI Octane (Intrepid, 120 megaflop) and a Cray J932 (Chilkoot, 12 CPU at 2.4 gigaflop each, 200 total if optimized for this platform). Generally the same models took two to three times longer to run on the Cray J932 than on the SGI Octane. This is likely because HKS (the ABAQUS software developer) uses the SGI as a development platform, which results in increased efficiency on that equipment.

Convergence controls. For the static analysis ribbed tire model, the tire is maneuvered in several steps, with the convergence controls adjusted at each step to increase efficiency. The loose convergence controls will allow the model to run faster, but convergence stops after rolling only a short distance. For dynamic rolling the model using the default convergence controls runs faster, and the tire rolls three times farther, than when convergences controls are looser or tighter than default values.

COMBINED TIRE–TERRAIN MODEL

Modeling the tire–terrain contact interface

Contact

To merge the tire and terrain models, the interface between the two meshes must interact. This is accomplished by defining where contact is allowed, how the contact occurs, and how forces are transmitted. For two meshes to come into contact, a surface must be placed on each material. For a deformable tire on snow or soil, one surface covers the outside of the tire and another surface lies on the top of the terrain layer. The contact is defined by the proximity of the surfaces. When both material meshes are deformable, one surface is chosen as a “master” surface and the other as a “slave” surface. The more finely meshed surface is usually chosen as the slave since the nodes on the slave surface are not allowed to penetrate the master surface.

Contact can be enforced using either “penalty” or “kinematic” contact methods. Both methods were used. Penalty contact was implemented for pseudo-static analyses, where inertia forces were not considered. In penalty contact the penetration of the surfaces into each other is resisted by linear spring forces with values proportional to the distance of penetration. These forces pull the surfaces into an equilibrium position with no penetration. Kinematic contact was used in some of the dynamic simulations (using the explicit code). Kinematic contact considers the inertia forces of the material when calculating the forces relative to the surface positions. Although the overall model results were the same with both contact methods, the kinematic contact was slightly more representative of field observations of the snow deformation beneath the wheel (Haehnel 2000).

Friction

Forces parallel to the interface are transmitted based on a friction law. Friction is a complex phenomenon involving stress and strain distributions; heat transfer; hydrodynamic and elastohydrodynamic fluid flow; material structure; chemical interactions between surfaces, surface coatings, and lubricants; and phase change. Current models of friction are empirical or semi-empirical formulations in which several variables and combinations of variables are modified with coefficients and exponents based on experimental observations. These equations apply only to the system for which they were developed, though they may be used to estimate the behavior of similar systems. They are not applicable to other experimental configurations or test conditions and cannot be extrapolated outside of their bounds with any degree of confidence. Thus, an accurate model of friction is currently non-existent and is not likely to be developed in the immediate future. The only reasonable way to predict the behavior of most frictional systems today is to test them (Ludema 1996a, 1996b, Barber 1991).

The experimental measurement of tire-terrain friction (including pavement) is typically performed as a vehicle traction or braking test [a discussion of winter traction test methods is available in Shoop et al. (1994)]. Test data are generally reported as a traction (or friction) coefficient (a peak value or an averaged value over a specified range) or as a traction curve with respect to wheel slip. Traction coefficients and curve shapes are functions of both the tire and the surface. Curves of traction data with wheel slip can be implemented in ABAQUS or other finite element analysis codes by specifying friction as a function of relative velocity. Liu and Wong (1996) took this approach using a friction law of the following form and implementing it in a tire-terrain model using the general-purpose finite element program called MARC:

$$\tau = \mu \sigma (1 - e^{-j/k}) \quad (26)$$

where μ = friction coefficient
 τ = shear stress
 σ = normal stress
 j = relative slip distance between the wheel and the terrain
 k = constant having the same units as j .

This equation is of the type commonly used in conjunction with soil shear data. However, Liu and Wong were not convinced that this equation adequately described traction.

The simulation of driving and braking traction would be an important extension of this research. More-elaborate friction models could be generated based on the multitude of experimental traction data obtained by CRREL. However, this need for a traction curve *a priori* seems to negate the usefulness of the model for predicting traction (i.e. the traction input is needed to get a valid traction output). Thus, the current modeling effort focused on the tire forces developed due to deformation of the snow rather than due to the interaction at the interface (i.e. a model of rolling resistance rather than traction). Therefore, for this project the simple Coulomb friction model was used:

$$\mu = \tau / \sigma. \quad (27)$$

Rigid wheel in snow

Model construction

The snow-wheel model simulates one wheel of the CRREL Instrumented Vehicle moving through a range of shallow (20 cm) to deep (50 cm) fresh snow with a density of 200 kg/m³. The wheel is modeled as a rigid surface 0.74 m in diameter and 0.272 m wide (for a full wheel) with a 0.051-m radius of curvature on the tire shoulder. An unsprung mass of 636 kg is placed at the hub to simulate the weight of the vehicle and tire; the rotational inertia of the wheel was set to 2.15 kg m². The snow was modeled with eight-node continuum elements near the wheel and four-node infinite elements for the far-field snow cover. The Drucker-Prager cap material model with linear elasticity was used for the snow, and a linear elastic model was used for the infinite elements. Coulomb friction was applied at the tire-snow interface ($\mu = 0.3$). The deep snow was modeled using Adaptive Lagrangian-Eularian (ALE) meshing to accommodate the large displacements, so slide planes were not needed along the sides of the tire. The shallow snow model had 11,520 continuum elements and 1,418 infinite elements; the deep snow model had 14,400 continuum and 1,962 infinite elements. In all models the snow rested on a rigid surface. The shallow snow model is shown in Figure 56.

The rolling resistance test is simulated by first lowering the wheel into the snow by gravity, accelerating it to the desired speed, and then translating it at a constant velocity. The wheel is moved longitudinally by displacing the axle node. This simulates a towed wheel and duplicates the procedure of a rolling resistance test using the CRREL Instrumented Vehicle.

These models were configured for both implicit dynamic analysis and explicit dynamic analysis. The explicit models used ALE meshing, where the mesh automatically adjusts during the deformation by allowing mass transfer between elements. The final

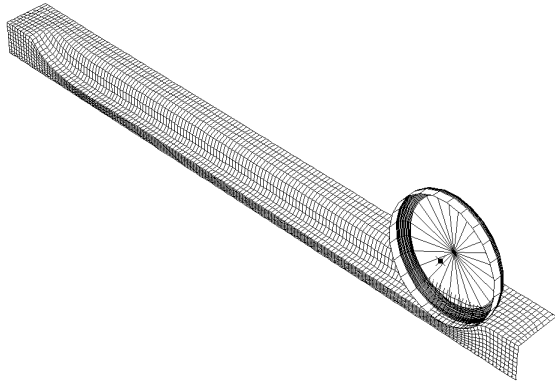


Figure 56. Model of a wheel rolling on 20 cm of fresh snow (infinite elements not shown).

mesh, therefore, does not directly reflect the deformation of each element, as in a standard finite element mesh, because the nodes and elements have moved relative to the snow mass. However, the final surface shape is correctly represented, and tracer nodes can be used to track the mass movement. The ALE meshing significantly reduces model run time (from over 48 hours to approximately 24 hours on an SGI Origin), eliminates severe mesh distortion, and smooths the resultant load response, but it does not affect the numerical results. Figure 57 shows the deformed mesh for the deep snow model with and without the ALE meshing.

The snow material properties were adjusted to match field measurements of sinkage and motion resistance. This was done primarily through changes to the cap hardening and consequent adjustments to the Drucker–Prager parameters. Since snow compaction is the primary mechanism contributing to motion resistance, the pressure–volume relationship for

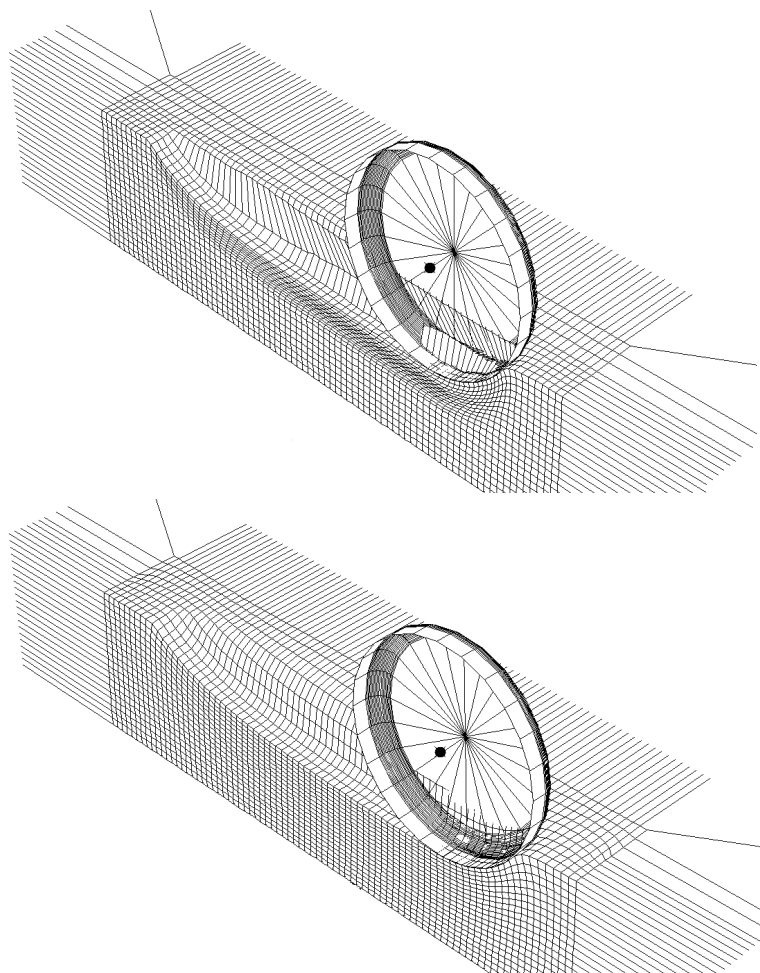


Figure 57. Comparison of standard mesh (top) and ALE mesh (bottom). (From Shoop et al. 1999.)

snow, reflected in the hardening table, has the greatest influence on resulting tire forces and sinkage. Changes to the acceleration, velocity, and friction coefficient have little effect on model results, partly because of the low velocities and accelerations involved in standard snow rolling resistance tests.

Motion resistance forces and sinkage

The tire–snow model was compared to field measurement of tire forces made with an instrumented vehicle. Model results were also compared to rolling resistance and sinkage predictions made from established algorithms for snow (as adopted by the NATO Reference Mobility Model).

Experimental measurements. Vehicle performance was measured using the CRREL Instrumented Vehicle (CIV), which is instrumented to measure vertical, longitudinal, and lateral forces at the tire–terrain interface; wheel speed at each wheel; true vehicle speed; and steering angles. The CIV is designed as a research tool to perform various mobility tests (traction, resistance, and maneuverability) using different tires, traction aids, and vehicle configurations (of braking and driving wheels) on a range of terrain surfaces including dry, wet, snow, ice, and freezing or thawing ground. The data obtained from these tests are used for model validation and for developing algorithms to predict vehicle performance on cold-weather terrain.

The vehicle, originally a 1977 American Motors Corporation Jeep Cherokee, is shown in Figure 58. Each wheel is instrumented with a three-component load cell (Fig. 59), designed and calibrated to respond to the forces at the terrain interface. The wheel speed is measured using a proximity sensor with a set of 100 measurement pegs set into the brake rotor. Wheel speed is compared to the true vehicle speed measured using a fifth wheel or a sonic speed sensor mounted



Figure 58. The CRREL Instrumented Vehicle (CIV).

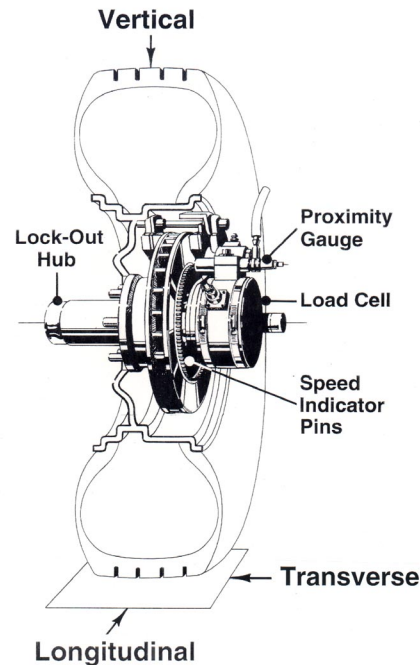


Figure 59. Configuration of speed sensors and axle-mounted load cells on the CIV (From Shoop et al. 1994.)

on the vehicle. The difference between the wheel speed v_w and the vehicle speed v_v is termed the differential interface velocity (DIV), also called the “slip speed” or “longitudinal slip velocity” (SAE 1992). This is often normalized by the speed of the vehicle and called slip i (ISTVS 1977):

$$i = \frac{v_w - v_v}{v_v} \times 100\% . \quad (28)$$

Using this convention, driving slip is positive and braking slip is negative.

Rolling resistance or motion resistance is the sum of the forces resisting vehicle motion. These are forces due to the internal friction of the moving parts of the vehicle, the air drag, the internal resistance of the tires due to flexing of the belts and plies and viscous properties of the rubber compounds, and the added resistance due to the deformation of the surface. The CIV measures motion resistance forces directly at the wheel, eliminating the forces acting on the vehicle body. Motion resistance is tested with the CIV by rolling the vehicle through snow at a constant speed. The vehicle is driven with the rear wheels only, and the front brakes are released so that the only forces on the front wheels are due to the tires and snow. The internal resistance of the tire is measured by rolling it on a hard surface. This value is subtracted from the snow motion resistance measure-

ment to obtain the resistance due only to the deformable snow (or other terrain). The experimental values of rolling resistance presented here are only the portion of the resistance due to the deformation of the terrain (snow).

CRREL has a large database of vehicle measurements in snow. For comparison to model data, most of the field measurements were taken from a study of wheeled and tracked vehicle performance in snow that was performed in Houghton, Michigan, in 1988 and 1989 and documented in Blaisdell et al. (1990) and Green and Blaisdell (1991). Motion resistance measurements formed a significant portion of this

study. Resistance in shallow snow was studied further in an experimental program in 1993, also in Houghton, Michigan, documented in Richmond (1995). The data from these studies are given in Table 11. The majority of these data were collected using Michelin XCH4 tires except where a different radius is noted. This database was used to develop a semi-empirical performance model for mobility on snow, which was incorporated into the NATO Reference Mobility Model (NRMM II) (Richmond et al. 1995, Ahlvin and Shoop 1995). Both the original data and the predictive algorithms were compared to the tire-snow finite element model.

Table 11. Measured sinkage and resistance in snow. All tires are the same (radius = 38 cm), except for the last four measurements.

<i>Snow depth (m)</i>	<i>Sinkage (m)</i>	<i>Resistance coefficient</i>	<i>Snow density (kg/m³)</i>
0.13	0.10	0.05	160
0.16	0.12	0.06	160
0.15	0.12	0.05	170
0.19	0.15	0.08	170
0.16	0.13	0.07	160
0.17	0.14	0.06	160
0.18	0.15	0.06	170
0.19	0.16	0.07	170
0.21	0.17	0.07	220
0.21	0.17	0.10	220
0.20	0.16	0.07	220
0.21	0.17	0.12	220
0.20	0.16	0.07	220
0.21	0.16	0.09	220
0.18	0.14	0.07	220
0.19	0.16	0.10	220
0.21	0.16	0.06	220
0.22	0.17	0.07	220
0.21	0.15	0.07	220
0.18	0.13	0.05	220
0.18	0.13	0.06	220
0.20	0.15	0.07	220
0.21	0.16	0.07	220
0.22	0.17	0.08	220
0.22	0.17	0.06	220
0.22	0.17	0.05	220
0.14	0.10	0.02	110
0.13	0.90	0.03	110
0.17	0.14	0.03	110
0.16	0.12	0.04	110
0.18	0.15	0.03	110
0.16	0.12	0.06	110
0.16	0.13	0.14	230
0.38	0.33	0.19	220
0.38	0.31	0.19	160
0.36	0.31	0.21	160
0.32 (r = 35 cm)	0.26	0.17	190
0.28 (r = 33 cm)	0.25	0.10	120
0.26 (r = 33 cm)	0.22	0.16	170
0.25 (r = 33 cm)	0.23	0.12	120

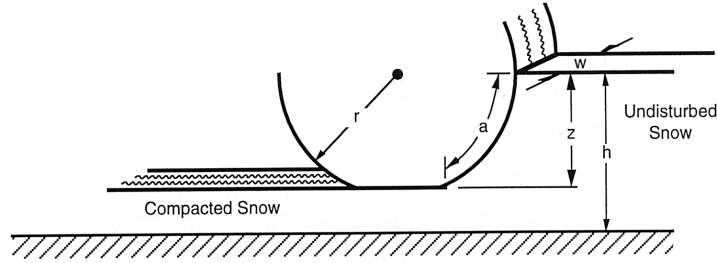


Figure 60. Parameters used to predict motion resistance using the NRMM algorithm. (From Richmond 1995.)

NRMM prediction of motion resistance in snow. The following method was proposed by CRREL for predicting the motion resistance in snow. It was adopted into the NATO Reference Mobility Model as part of the overall vehicle performance predictions scheme. Only the portions of the algorithms related to motion resistance in snow are stated here. Based on Richmond (1995), the motion resistance for the leading tire in shallow snow R_s is based on the vehicle sinkage z according to

$$R_s = 13.6041(\rho_0 w a)^{1.26} \quad (29)$$

$$a = r \arccos [(r-z)/r] \quad (30)$$

$$z = h \left(1 - \frac{\rho_0}{0.519 + 0.0023 p_{\max}} \right) \quad (31)$$

where R_s = motion resistance (leading tire only) (N)
 ρ_0 = initial snow density (kg/m^3)
 w = maximum tire width (m)
 a = arc length in contact with snow (m)
 r = tire radius (m)
 z = sinkage (m)
 h = snow depth (m)
 p_{\max} = maximum tire contact pressure (kPa).

These parameters are illustrated in Figure 60.

Very little data is available for wheeled vehicles in deep snow. However, based on numerous observations of snow vehicle movement, the following factors are applied to the shallow snow equations to estimate the additional motion resistance in deep snow. The factors represent an engineering estimate of the additional forces due to plowing of the vertical face of the wheel and undercarriage drag (Richmond et al. 1995). The deep snow modifiers would be applicable to wheels being dragged or towed through deep

snow, since a driven wheel would not likely have enough traction to overcome the large resistance and would become immobile.

$$\text{For } \rho_0 > 150 \text{ kg/m}^3 \text{ and } 2/3 r < z < r, \quad (32) \\ \text{Factor} = 1.5$$

$$\text{For } \rho_0 > 150 \text{ kg/m}^3 \text{ and } z > r, \quad (33) \\ \text{Factor} = 2.5.$$

Comparison of measurements, NRMM, and finite element results. In the FEA model the longitudinal reaction force at the wheel hub represents the motion resistance force on the wheel due to deformation of the snow and is directly comparable to the motion resistance measured with the CRREL Instrumented Vehicle. Similarly the vertical displacement of the hub node is equivalent to the sinkage of the wheel into the snow (since the wheel itself is not deforming in this simulation). Figure 61 shows the resistance coefficient (the longitudinal load divided by the vertical load on the hub) and vertical displacement for one of the snow model runs. For this model the vertical loading occurs from 0 to 1.5 s, the horizontal acceleration occurs from 1.5 to 2.0 s, and then constant speed translation is maintained from 2.5 to 5 s at a speed of 8 kph (5 mph). The sinkage and motion resistance values are chosen as the average of the values occurring during the constant speed portion of the simulation.

Comparisons of the measured and modeled sinkage and motion resistance are shown in Figure 62 as a function of snow depth. The model overestimates motion resistance, but the trends are consistent with the measured data and the model falls directly along the upper edge of the measurements, constituting a conservative prediction. The NRMM predictions of motion resistance are discontinuous based on the snow depth. For this tire, motion resistance for snow depths less than 25 cm are calculated using NRMM eq 29, for depths from 25 to 38 cm using eq 31, and for

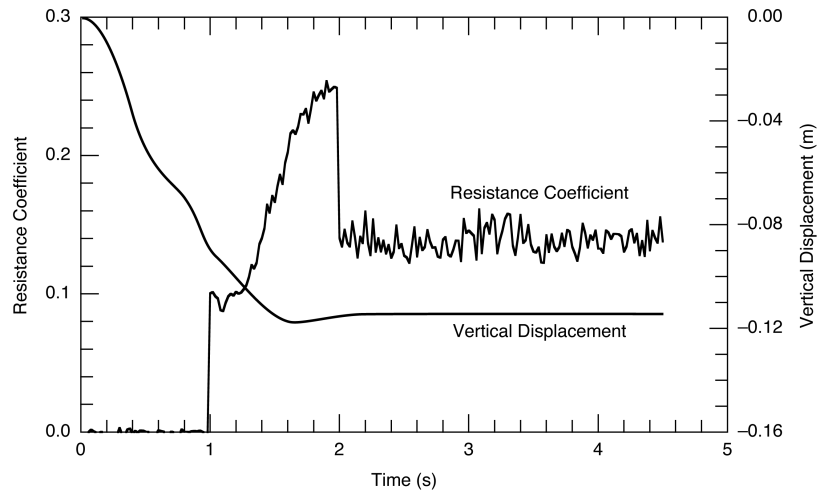


Figure 61. Modeled resistance force in coefficient form (longitudinal/vertical) and vertical displacement of the wheel hub for the FEM wheel rolling through 20-cm snow.

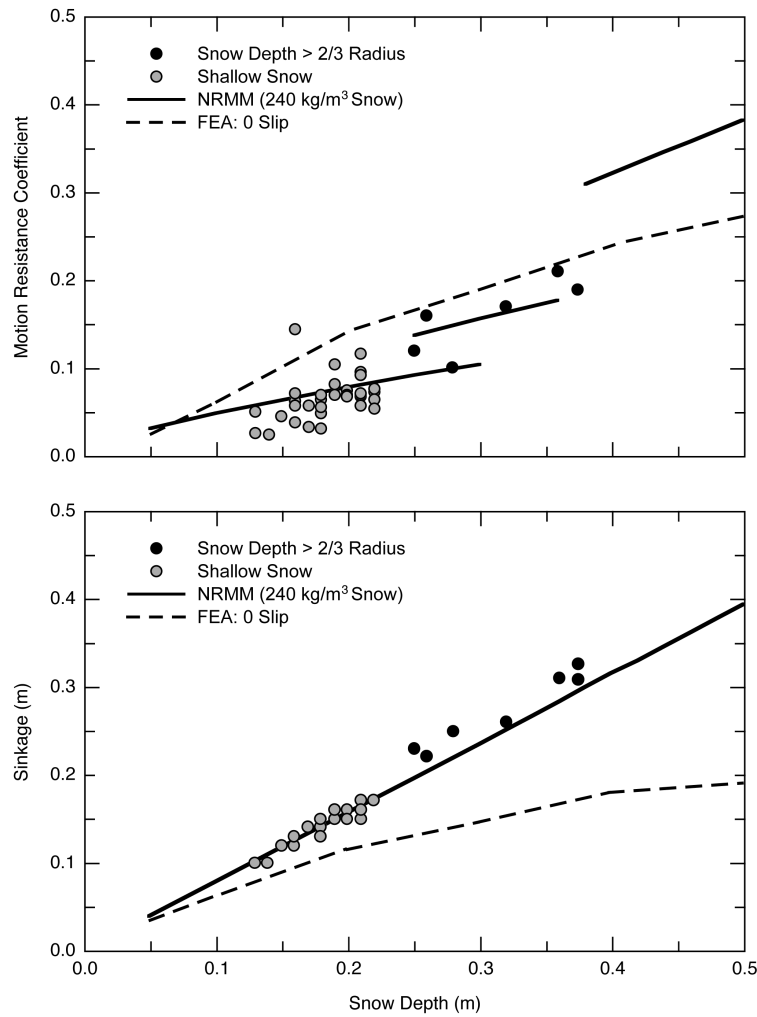


Figure 62. Finite element model, measured data, and NRMM predictions for sinkage and motion resistance in fresh snow.

snow depths greater than 38 cm using eq 32. The finite element model falls between the NRMM motion resistance prediction equations for deep snow, as does the measured data. The bottom part of Figure 62 shows the corresponding sinkage, which the finite element model (with zero slip) underestimates, particularly for the deeper snow.

The NRMM predictions are also a function of the initial snow density. Although the material model was designed to simulate 200-kg/m³ snow, NRMM predictions based on 240-kg/m³ snow yield an excellent match to the finite element resistance, as seen in the top of Figure 63. This would indicate that the FEA model is more representative of a slightly denser snow.

Figure 63 also shows model results for a wheel

with zero slip and with unrestricted slip. The NRMM deep snow resistance predictions are close to the finite element results for a free slipping wheel, as would be expected for a wheel being dragged through deep snow, while shallow snow results are best represented by the simulation with zero slip.

The bottom of Figure 63 shows the measured sinkage data falling between the zero slip and unrestricted slip models. Measured slip in shallow snow is near zero, but higher slip measurements are not uncommon as the snow gets deeper. Realistically the model should behave somewhere between these two extremes. This part of the physics of the interaction is not accurately reproduced in the model, partly because the tread, which is designed to resist slippage, is not yet accurately modeled.

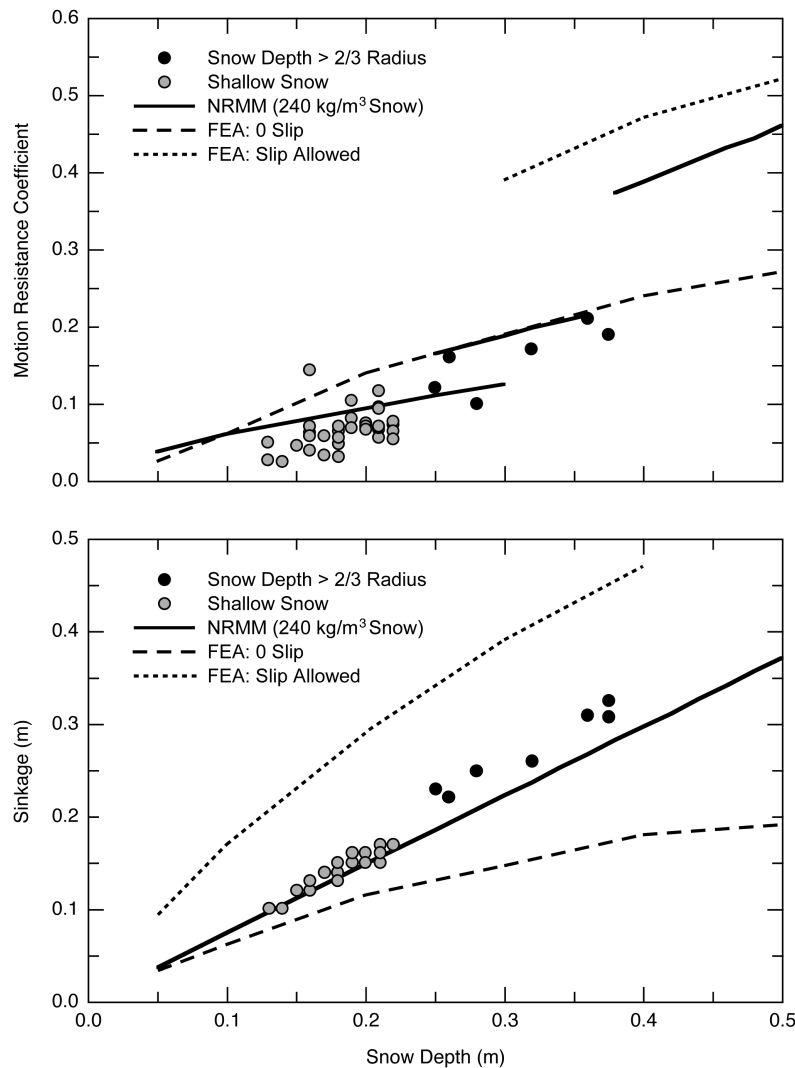


Figure 63. Finite element simulations at zero slip and at unlimited slip and NRMM motion resistance predictions for 240-kg/m³ snow.

Snow deformation beneath the wheel

Snow deformation under a vehicle can be measured by excavating a cross section of the snow as shown earlier in Figure 3. Additional detail can be obtained by marking the snow prior to deformation by backfilling a small-diameter, vertical hole with dark-colored chalk dust. The vehicle is then driven into the snow, and the changes in the lines can be seen when the cross section is excavated. This process is illustrated in Figure 64.

Once the snow cross section has been excavated, snow density can be measured by collecting and weighing samples of a known volume. This was done in several experiments (Richmond 1995). Modeled deformation of 20-cm, 200-kg/m³ snow was compared to measured snow deformation beneath the CIV in similar snow conditions. Because the model used ALE meshing, the displacement of the snow was documented by placing tracer particles in the model, spaced at the same distance as the markings in the field. Comparisons of the measured and modeled

snow deformation in cross sections in the direction of travel (longitudinal) and transverse to the direction of travel are shown in Figures 65 and 66. The deviatoric stress contours shown in the longitudinal cross section reveal the location where a new shearing surface begins to develop ahead of the advancing wheel. The failure arc, even for snow, clearly advances downward and away from the wheel, just as shown experimentally for sand in Figure 1. The deformation predicted in the model is slightly less than the observed deformation, partly because the model is for deeper (20 cm) and denser (200 kg/m³) snow than occurred in the field. The general shape of the displacement is the same, however.

The measured density and the modeled density are in good agreement, as shown in the transverse cross section in Figure 67. The modeled density directly beneath the wheel (460 kg/m³) is only 10% different from the measured density (510 kg/m³). Near the tread shoulder, the modeled density was 290–380 kg/m³, with measured values ranging from 280 to 300 kg/m³.

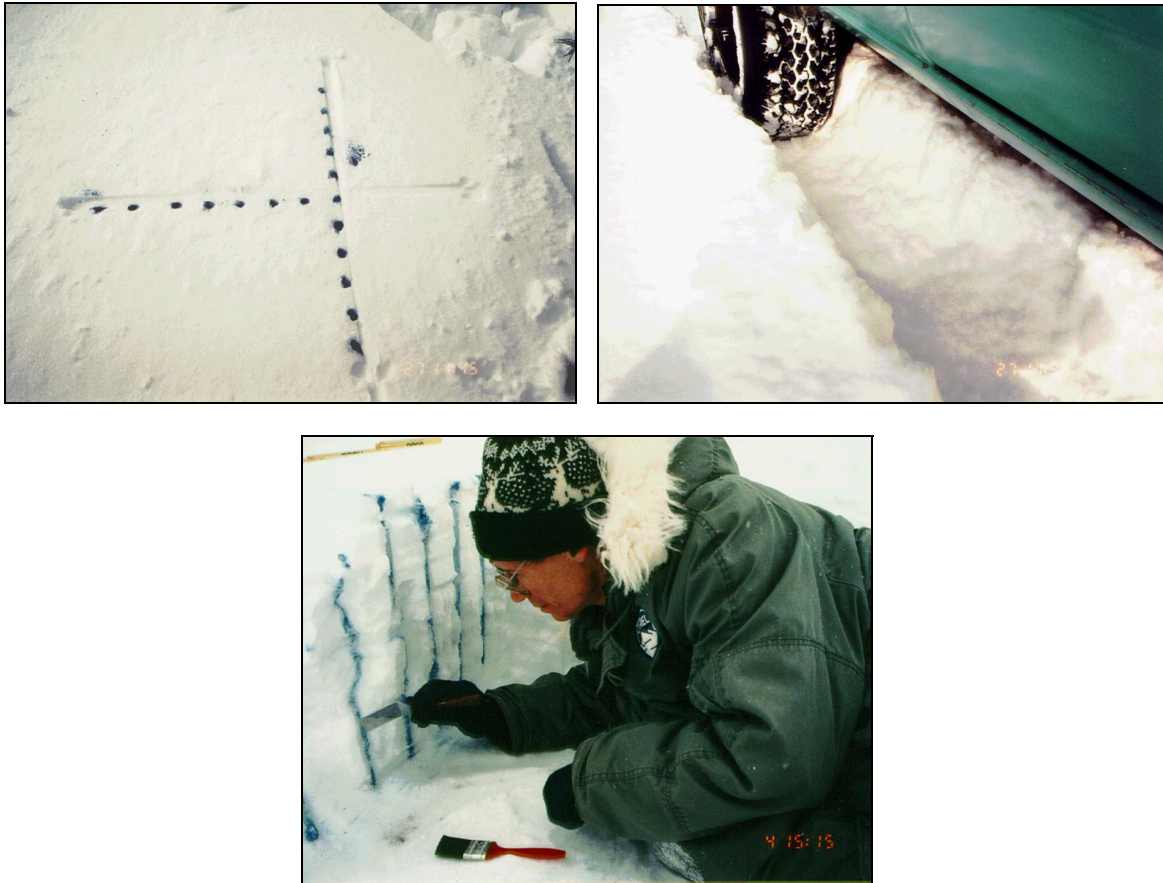


Figure 64. Marking the snow to observe snow deformation after vehicle passage.

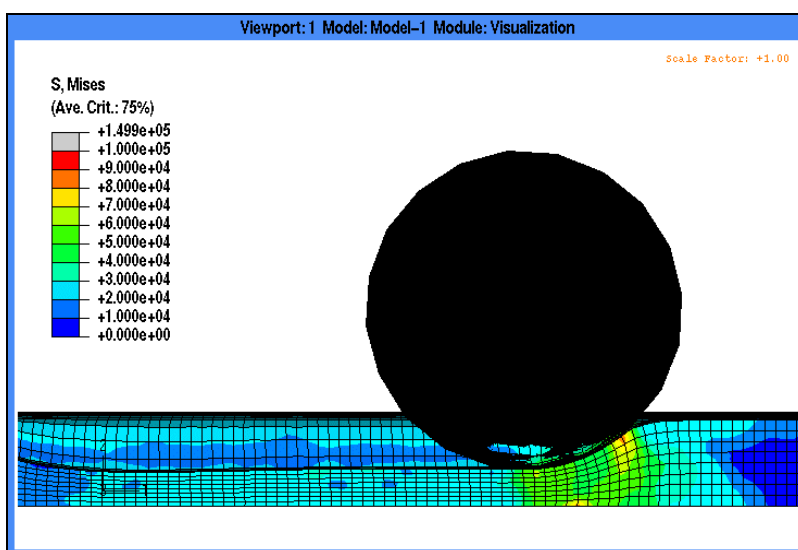
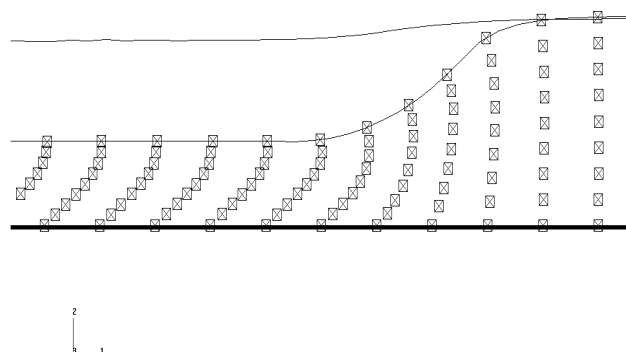


Figure 65. Comparison of measured displacement (14.5-cm snow) to modeled displacement and deviatoric stress (20-cm snow) in the longitudinal direction.

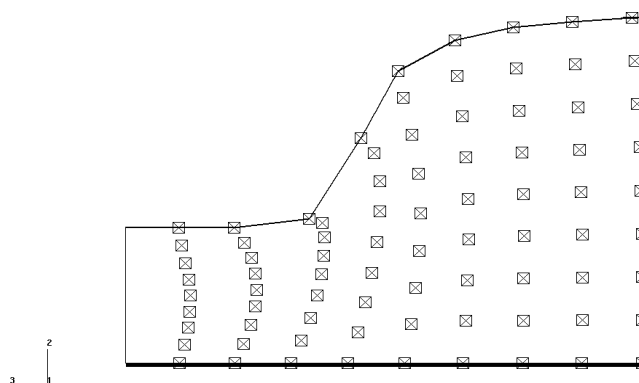


Figure 66. Comparison of measured (19-cm snow) and modeled (20-cm snow) displacement in a cross section transverse to the direction of travel.

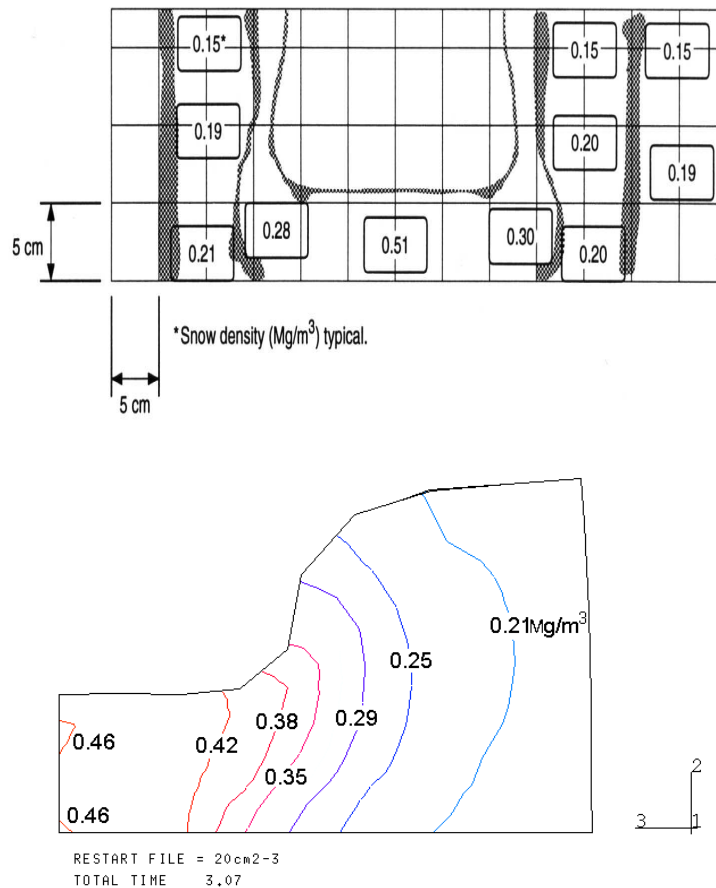


Figure 67. Comparison of measured (19-cm snow) and modeled (20-cm snow) densities in a cross section transverse to the direction of travel.

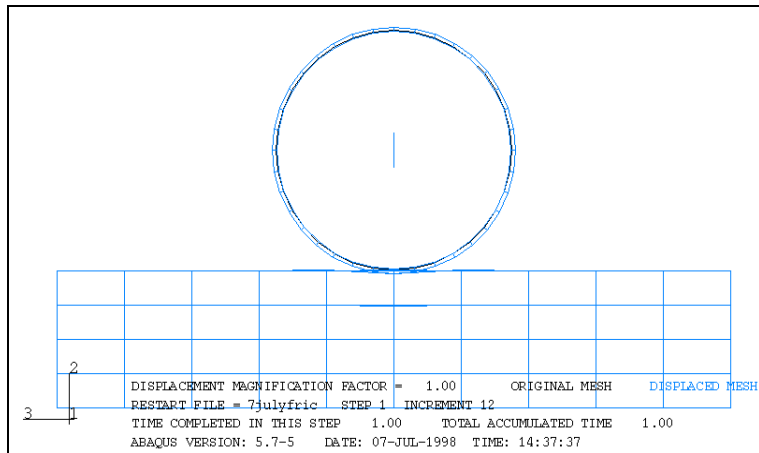
Deformable tire on soil

On harder terrain it is important to model the deformation of the tire in addition to the deformation of the terrain. Because of the large deformation and run times involved, it is important that the tire model be as efficient as possible while still maintaining an accurate contact patch. Thus, the tire model used for rolling on soil was based on the formulation proposed by Darnell et al. (1997).

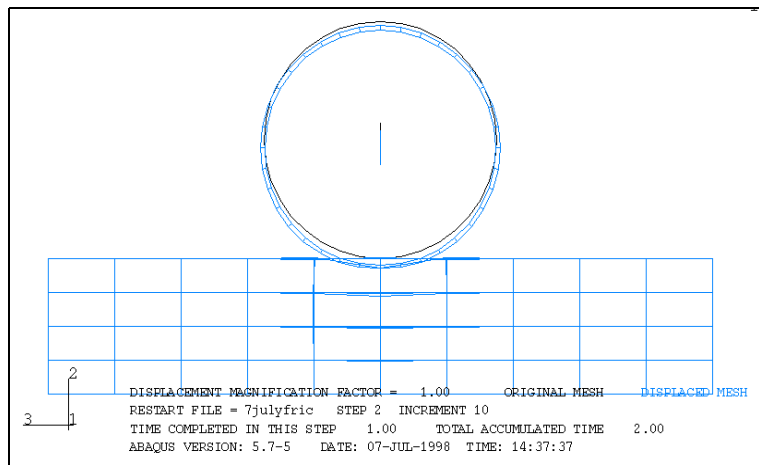
The Shoop–Darnell tire model was modified to roll across deformable material, such as soil. This tire was first placed on an elastic terrain material with the properties of compacted sand. The simulation was conducted in four steps: the tire was first inflated, then lowered into the soil, allowed to come to equilibrium, and then rolled to the left, as seen in Figure 68. Only the tread and soil elements are shown in the figure; the user-defined sidewall elements are not displayed. Figure 68d is an oblique view of the three-dimensional model showing the contact pressure.

The same tire was then rolled on a Drucker–Prager cap plasticity model representing the McCormick Ranch sand (discussed earlier). The results of this simulation are given in Figure 69, showing the maximum principal plastic strain and the principal stress directions. The maximum principal stress is compressive beneath and slightly forward of the tire. The minimum principal stress is tensile and is largest just below and to the sides of the tire, oriented away from the tire. The difference between these stresses indicates the magnitude of shear stress in the soil, which is largest beneath and directly in front of the tire. This corresponds to the general shear zones beneath a towed rigid wheel observed by Wong and Reece (1967), shown in Figure 1.

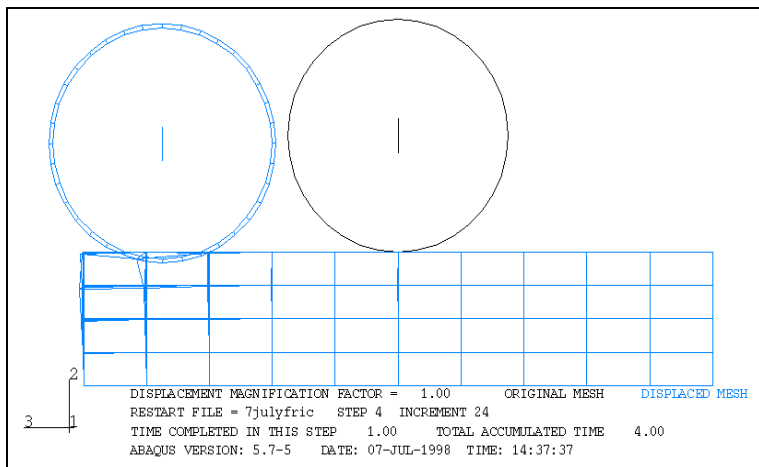
The tire-soil models are prototypes requiring refinement and development. They will eventually be compared to field measurements of tire forces, deflection, and contact area, including sinkage and deformation of the soil surface.



a. Tire inflated.

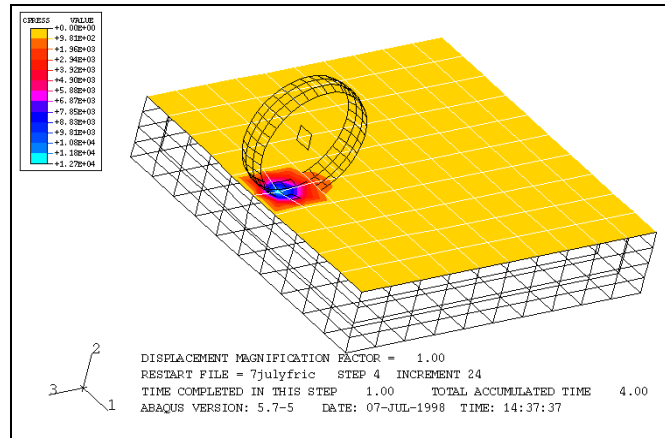


b. Tire lowered onto soil.



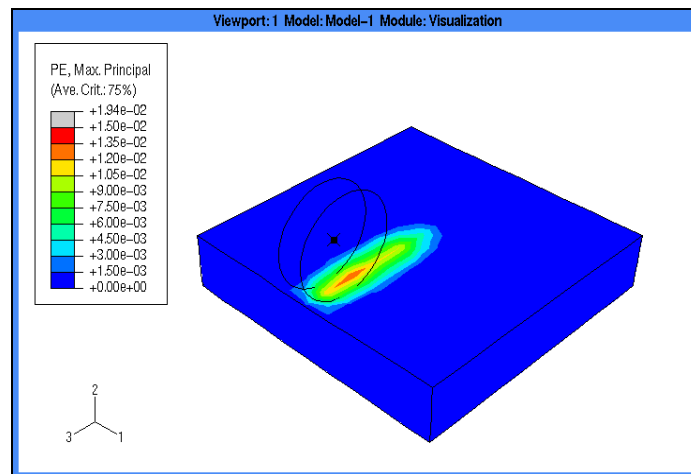
c. Tire rolled to the left.

Figure 68. Rolling tire on an elastic material (sand).

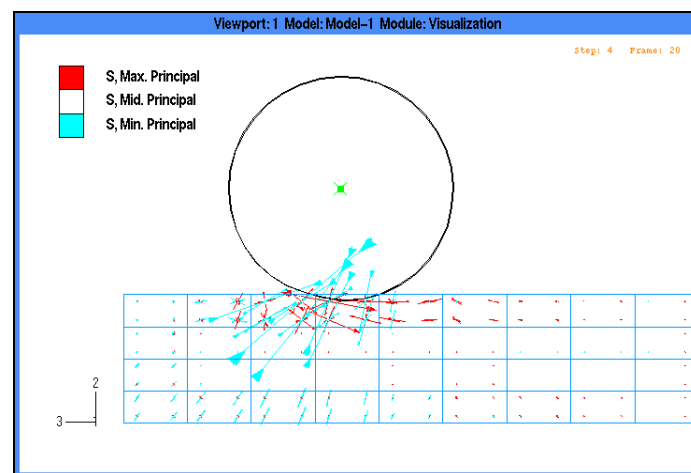


d. Contact pressure.

Figure 68 (cont.).



a. Plastic strain.



b. Principal stress directions as the tire rolls to the left.

Figure 69. Rolling Shoop–Darnell tire on a Drucker–Prager cap model of the McCormick Ranch sand.

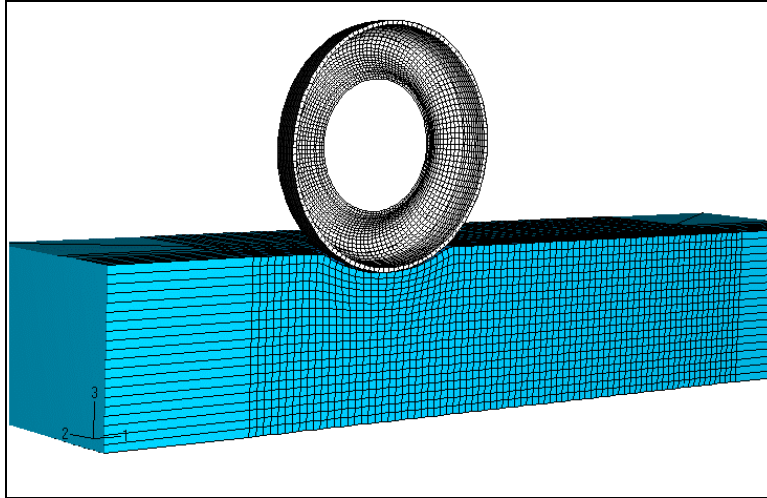


Figure 70. Deformed mesh of the modal analysis tire model in snow after 8 cm of sinkage in snow.



Figure 71. Close-up of a tire after sinking 8 cm into the snow at the beginning of roll. The tire shows very little deformation (the deflection is 3 mm), indicating that a rigid wheel may be a good approximation.

Deformable tire on snow

Simulations of the modal analysis tire on snow are in progress.* Although preliminary runs are very slow and have not progressed to completion, intermediate results are available. Figure 70 shows the simulation after the tire has been lowered onto the snow and begins to roll. The sinkage is approximately 8 cm, which is about the same as the modeled sinkage for the rigid wheel on 20-cm snow, as seen in Figure 61. Of significant note, however, is that the deformable tire has undergone very little deformation (the deflection is 3 mm, which is less than 2%), as

seen in Figure 71, revealing that the rigid wheel model for deep fresh snow may be a valid assumption (although these results are only preliminary).

CONCLUSIONS

Summary

The interaction between a tire and deformable terrain is a complicated dynamic process that involves the deformation of both the tire and the terrain in three dimensions. The tire is a complex structure made of many materials, and the terrain undergoes large deformations in an inelastic manner, so neither component is easily modeled. The objective of this

* Personal communication with K. Kestler, private consultant, 2000.

research was to produce a three-dimensional finite element model of tire–terrain interaction that can be used to explore the effects of tire and terrain variables on vehicle mobility. Such a model can be used for tire design and specification for off-road vehicles, for vehicle performance prediction, and for terrain damage prediction and reduction of the environmental impact of off-road travel.

The details of the tire–soil modeling problem are divided into three topic areas: 1) material models for the terrain material, 2) tire models for use on a deformable substrate, and 3) the combined tire–terrain model and the treatment of the interface. The terrain materials simulated in this study were fresh snow and compacted sandy soil. The two material models used were a modified Drucker–Prager cap plasticity model and a critical-state, crushable foam model. Both models were considered suitable for capturing the highly compressible behavior of fresh, natural snow (initial density of 200–250 kg/m³ at temperatures of –10° to –1°C). Model parameters were generated from field test data and from the literature, matching this snow type as closely as possible. The snow model was validated using plate sinkage test data for snow of similar age and density. The soil model represents sand similar to that used during vehicle mobility experiments at CRREL. The material was modeled using a Drucker–Prager cap plasticity model with input parameters from the literature.

To apply a tire model to deformable terrain, the model must be efficient yet accurately portray the tire structural behavior. Four tire models were evaluated for suitability to rolling on deformable terrain: 1) a rigid tire model, 2) a simplified tire model using methodology developed by Darnell at the University of Michigan for use in vehicle dynamics simulations, 3) a tire model of the type used for harmonic vibration modal analysis, with a smooth tread, and 4) a tire model similar to model 3 except with a straight ribbed (longitudinal) tread. All of the models were built to represent tires used in the experimental test program for comparison to measured tire behavior in terms of deflection, contact area, deflected sidewall profile, contact stress distribution, and rolling resistance forces on deformable terrain (snow and soil).

Three models of the combined tire and terrain were developed. The first is a rigid tire on fresh snow. The second is the Shoop–Darnell tire model rolling on a soil, and the last is the modal analysis tire on snow. Model results simulating a rigid tire rolling on snow were compared to tire forces measured using an instrumented vehicle. The measured snow deformation under the wheel was also compared to model results. The model exhibits good agreement with mo-

tion resistance forces but underestimates sinkage. The measured deformation patterns are duplicated in the model, but the modeled displacements are less than what is measured in the field. Model results were also compared to snow mobility predictions made using the largely empirical NATO Reference Mobility Model, with good agreement for forces but underestimation of sinkage. The amount of wheel slip had a major impact on the modeled sinkage.

Simulations of a tire rolling on soil and snow using the Shoop–Darnell tire and the modal analysis tire model are operational but have not been validated. Of significant note, however, is that a simulation using the modal analysis tire on fresh snow predicts very little tire deformation (3 mm, or less than 2% deflection). This suggests that the assumption of a rigid tire may be used for soft terrain such as deep, fresh snow without loss of model accuracy.

Significant findings

The following summarizes the significant achievements of this work:

1. A material model was developed for fresh snow and validated with plate sinkage tests in the lab and field. Good agreement of measured and modeled forces, displacements, and changes in material density were achieved.
2. Evaluations of several finite element tire models suitable for rolling on a deformable substrate indicate that the Darnell model yielded accurate results and was computationally efficient. The modal analysis type of tire model is also suitable but is more computationally intensive.
3. Combined tire–terrain models utilizing the Shoop–Darnell tire and the modal analysis tire model are operational but have not yet been validated. Preliminary results of the modal analysis tire model on snow show very little deformation in the tire, indicating that the rigid wheel simplification may be valid for soft terrain.
4. A model of a rigid wheel on fresh snow, validated experimentally, shows good agreement with measured motion resistance forces, snow displacement, and snow compaction and agrees with results predicted by the NATO Reference Mobility Model.
5. The rigid wheel on snow model does not capture the tread effects of the tire–terrain interaction (as tread patterns were not expressly modeled). For a free-rolling wheel, the amount of slip and sinkage is overpredicted. When the model wheel slip is set to zero, as is measured during shallow snow resistance tests in the field, sinkage is underpredicted. The most realistic results lie between these two

cases and can possibly be modeled with “rough” friction attributes. A full understanding of this effect will be critical for traction and braking studies.

Recommended applications and future research needs

Parametric design analysis

The primary applications of a tire–terrain model are 1) all-season and off-road performance prediction for tires, 2) tire design, optimizing geometry, materials, and tread patterns, and 3) specification of the correct tires based on expected operating conditions. Naturally, design use of the model could include a parametric analysis of the impact of tire and terrain parameters on tire performance. Such a study, evaluating the effects of tire geometry and loading on rolling resistance in snow, may now be undertaken using the results of this research.

Interface friction and interlocking of tread and terrain

The processes occurring at the interface of the tire and terrain are also of great interest. Advances in driving and braking traction mechanics through sophisticated study of interface friction, and the implementation of this in a numerical model, are of major significance because of their large impact on tire and vehicle performance and safety. Since the tread pattern was not modeled in this study, the details of the interface friction and frictional interlocking, which affected the resulting slip of the tire, were not specifically modeled. Issues include the interaction of terrain material and tread blocks and the impacts of a spinning tire on traction through frictional heating and mass shearing. Modeling challenges include coupling with other models, such as submodels of tread blocks, and discrete element or hydrodynamic models of terrain material. The practical application of this is readily apparent for tread design.

Deformation of terrain materials subjected to vehicle loading

Research is also needed in areas relating to the deformation of the materials beneath the wheel, such as:

1. Soil deformation under vehicles and implications for terrain damage through soil compaction, rut formation, root tearing, etc.
2. Washboard formation on secondary roads, including the effects of suspension parameters, vehicle speed, and road material.
3. Dynamic models of vehicles on pavements, including impacts on pavement structure and dete-

rioration, loading effects on soil water (pumping up through pavement layers and cracks), and the function of drainage materials, including geosynthetics.

4. The impact of temperature-dependent material properties, such as frictional heating and melting of snow, ice, or frozen ground.

Additional terrain material models

Future work should also include extending the material models to other terrain materials, such as wet, trafficked snow or slush, and soft, loose soils. Trafficked snow is typical of much of the snow on roads before clearing and therefore is of primary interest to snow maintenance operations, tire companies for improving design of snow tires, automotive companies for optimizing vehicle handling, and for the rolling resistance of the snow and its effect on fuel economy. The thawing soils material represents a critical case for roads subjected to freeze–thaw, where soil moisture is pulled to the surface during freezing (expanding soil pores or forming ice lenses), resulting in a wet and loose soil during seasonal, intermittent, or even daily thawing events. Some of the difficulties in modeling this unique material may be simulated using the more flexible Multi-Mechanical Model proposed by Peters* and Smith (2000) or through hydrodynamic modeling. Additional behaviors specific to the interaction of snow grains during loading and resulting sintering may be better approached using a discrete element model as proposed by Johnson and Hopkins.**

LITERATURE CITED

- Abele, G., and A. Gow** (1975) Compressibility characteristics of undisturbed snow. Research Report 336, U.S. Army Cold Regions Research and Engineering Laboratory, Hanover, NH.
- Ahlvin, R.B., and P.W. Haley** (1992) NATO reference mobility model edition II, NRMM II user's guide. WES Technical Report GL-92-19, U.S. Army Waterways Experiment Station, Vicksburg, MS.
- Ahlvin, R., and S.A. Shoop** (1995) Methodology for predicting for winter conditions in the NATO Reference Mobility Model. In *Proceedings, 5th North*

* Personal communication with J.F. Peters, GSL, ERDC, 1999.

** Personal communication with J. Johnson and M. Hopkins, CRREL, 2000.

American Conference of the ISTVS, Saskatoon, Saskatchewan, Canada, May 1995, p. 320–334.

Alger, R. (1988) Effect of snow characteristics on shear strength. Contract Report DACA89-88-K-004, Keweenaw Research Center, Michigan Technological University, Houghton, Michigan.

Alger, R., and M. Osborne (1989) Snow characterization field data collection results. Final Report ACA89-85-K-002, Keweenaw Research Center, Michigan Technological University, Houghton, Michigan.

Alkire, B.D. (1992) Seasonal soil strength by spectral analysis of surface waves, *Journal of Cold Regions Engineering*, **6**(1): 2–38.

Alvarez Sanz, M.B. (1999) A parametric study of a three-dimensional tire finite element model. Master's thesis, Department of Mechanical Engineering and Applied Mechanics, University of Michigan.

Aubel, T. (1993) FEM simulation of the interaction between elastic tyre and soft soil. In *Proceedings, 11th International Conference of the ISTVS, Lake Tahoe, Nevada*, vol. 2, p. S791–802.

Aubel, T. (1994) The interaction between the rolling tyres and the soft soil FEM simulation by VENUS and validation. In *Proceedings, 6th European Conference of the ISTVS, Vienna*, vol. 1, p. 169–188.

Bailey, A.D., and C.E. Johnson (1989) A soil compaction model for cylindrical stress states. *Transactions of the ASAE*, **32**(3): 822–825.

Barber, J.R. (1991) Is modeling in tribology a useful activity? In *Tribological Modeling for Mechanical Designers*, ASTM STP 1105.

Bekker, G. (1956) *Theory of Land Locomotion*. Ann Arbor, Mich.: The University of Michigan Press (2nd Edition, 1962).

Bekker, G. (1960) *Off-Road Locomotion*. Ann Arbor, Mich.: The University of Michigan Press

Bekker, G. (1969) *Introduction to Terrain-Vehicle Systems*. Ann Arbor, Mich.: The University of Michigan Press.

Blaisdell, G.L., P.W. Richmond, S.A. Shoop, C.E. Green, and R.G. Alger (1990) Wheels and tracks in snow: Validation study of the CRREL shallow snow mobility model. CRREL Report 90-9, U.S. Army Cold Regions Research and Engineering Laboratory, Hanover, NH.

Bowden, F.P. and D. Tabor (1964) *The Friction and Lubrication of Solids*. London: Oxford University Press.

Burke, A., and O.A. Olatunbosun (1997a) Static tyre/road interaction modelling. *Meccanica*, **32**(5): 473–479.

Burke, A., and O.A. Olatunbosun (1997b) New techniques in tyre modal analysis using

MSC/NASTRAN. *International Journal of Vehicle Design*, **18**(2): 203–212.

Burke, A., and O.A. Olatunbosun (1997c) Contact modelling of the tyre/road interface. *International Journal of Vehicle Design*, **18**(2): 194–202.

Chi, L., and S. Tessier (1995) Finite element analysis of soil compaction reduction with high flotation tires. In *Proceedings, 5th North American Conference of the ISTVS, Saskatoon, Saskatchewan, Canada*, p. 167–176.

Chiroux, R.C., W.A. Foster, Jr., C.E. Johnson, S.A. Shoop, and R.L. Raper (1997) Three-dimensional finite element analysis of soil interaction with a rigid wheel. In *Proceedings, 1997 ASAE Annual International Meeting, Minneapolis, Minnesota*. ASAE paper no. 971028, St. Joseph, Michigan.

Clark, S.K. (1981) *Mechanics of Pneumatic Tires*. U.S. Department of Transportation, National Highway Traffic Safety Administration.

Danielson, K.T., and A.K. Noor (1997) Finite elements developed in cylindrical coordinates for three-dimensional tire analysis. *Tire Science and Technology*, **25**(1): 2–28.

Darnell, I. (In progress) Efficient three-dimensional tire models. Ph.D. Dissertation, Department of Mechanical Engineering and Computational Mechanics, University of Michigan.

Darnell, I., G.M. Hulbert, and C.W. Mousseau (1997) An efficient three-dimensional tire model for vehicle dynamics simulations. *Mechanical Structures and Machinery*, **25**(1): 1–19.

DiMaggio, F.L., and I.S. Sandler (1971) Material model for granular soils. *Journal of Engineering Mechanics Division, ASCE*, **97**(EM3): 935–950.

DiMaggio, F.L., and I.S. Sandler (1976) Generalized cap model for geological materials. *Journal of Geotechnical Engineering Division, ASCE*, **102**(GT7): 683–699.

Fervers, C.W. (1994) FE simulations of tyre-profile effects on traction on soft soil. In *Proceedings, 6th European Conference of the ISTVS, Vienna, Austria*, p. 618–633.

Fervers, C.W. (1997) Effects of traction and slip, investigations with FEM. In *Proceedings, 7th European Conference of the ISTVS, Ferrara, Italy*, p. 117–124.

Fervers, C.W. (1999a) Phenomena of tyre-profile on different soils. In *Proceedings, 13th International Conference of the International Society of Terrain-Vehicle Systems, Munich, Germany*, p. 337–344.

Fervers, C.W. (1999b) Phenomena of air-filled tires and soft terrain. Investigations with FEM. Doctoral Thesis, University of Federal Armed Forces, Hamburg, Germany (in German).

- Foster, W.A., C.E. Johnson, R.L. Raper, and S.A. Shoop** (1995) Soil deformation and stress analysis under a rolling wheel. In *Proceedings, North American Conference of the ISTVS, Saskatoon, Saskatchewan, Canada*, p. 194–203.
- Fukue, M.** (1979) *Mechanical Performance of Snow under Loading*. Tokyo: Tokai University Press (based on author's thesis, McGill University, 1977).
- Gill, W.R., and G.E. Vanden Berg** (1967) *Soil Dynamics in Tillage and Traction*. Agriculture Handbook No. 316, Agricultural Research Service, USDA, U.S. Government Printing Office.
- Goodsell, D.** (1995) *Dictionary of Automotive Engineering*. Warrendale, Pennsylvania: Society of Automotive Engineers.
- Green, C.E., and G.L. Blaisdell** (1991) U.S. Army wheeled versus tracked vehicle mobility performance test program. Report no. 2: Mobility in shallow snow. Technical Report GL-91-7, U.S. Army Waterways Experiment Station, Vicksburg, MS.
- Haehnel, R.** (2000) Summary of model changes for a wheel rolling on a snow surface: FY2000. Unpublished memo.
- Harrison, W.L.** (1975) Vehicle performance over snow: Math-model validation study. U.S. Army Cold Regions Research and Engineering Laboratory, Technical Report 268.
- HKS (Hibbitt, Karlsson, and Sorensen, Inc.)** (1996) Analysis of geotechnical problems with ABAQUS. ABAQUS Course Notes, Pawtucket, Rhode Island.
- HKS (Hibbitt, Karlsson, and Sorensen, Inc.)** (1998) *ABAQUS Theory and User's Manuals*. Pawtucket, Rhode Island.
- Hu, Y.K., and P.F.J. Abeels** (1994) The deformation of agricultural tire on rigid surface by FEM. American Society of Agricultural Engineers International Summer Meeting, Kansas City, Missouri, June 19–22, 1993, ASAE Paper No. 941043.
- ISTVS (International Society of Terrain–Vehicle Systems)** (1977) ISTVS standards. *Journal of Terramechanics*, **14**(3): 153–182.
- Jaeger, J.C., and N.G.W. Cook** (1969) *Fundamentals of Rock Mechanics*. New York: John Wiley and Sons, Inc.
- Johnson, J., J. Brown, E. Gaffney, G. Blaisdell, and D. Solie** (1992) Shock response of snow. CRREL Report 92-12, U.S. Army Cold Regions Research and Engineering Laboratory, Hanover, NH.
- Karafiath, L.L., and E.A. Nowatzki** (1978) Soil mechanics for off-road vehicle engineering. In *Series on Rock and Soil Mechanics*. Clausthal, Germany: Trans Tech Publications, **2**(1974/77), no. 5.
- Kestler, M.A., S.A. Shoop, K.S. Henry, J.A. Stark, and R.T. Affleck** (1999) Rapid stabilization of thawing soils for enhanced vehicle mobility: A field demonstration project. CRREL Report 99-3, U.S. Army Cold Regions Research and Engineering Laboratory, Hanover, NH.
- Ladanyi, B.** (1997) Mechanical properties data base for ground freezing applications. *Ground Freezing* **97**, p. 43–52.
- Lade, P.V., and M.K. Kim** (1995) Single hardening constitutive model for soil, rock and concrete. *International Journal of Solids Structures*, **32**(14): 1963–1978.
- Liu, C.** (1994) Traction mechanisms of automobile tires on snow. Ph.D. dissertation, Vienna University of Technology, Vienna, Austria.
- Liu, C.H., and J.Y. Wong** (1996) Numerical simulations of tire-soil interaction based on critical state soil mechanics. *Journal of Terramechanics*, **33**(5): 209–222.
- Ludema, K.C.** (1996a) *Friction, Lubrication and Wear: A Textbook in Tribology*. New York: CRC Press.
- Ludema, K.C.** (1996b) Mechanism-based modeling of friction and wear. *Wear*, **200**(1-2): 1–7.
- Mazanti, B.B., and C.N. Holland** (1970a) Study of soil behavior under high pressure. Defense Technical Information Center, Contract Report, report 1, vol. 1. AD709315.
- Mazanti, B.B., and C.N. Holland** (1970b) Study of soil behavior under high pressure. Defense Technical Information Center, Contract Report, report 1, vol. 2. AD756124.
- Mellor, M.** (1975) A review of basic snow mechanics. In *Proceedings of the International Symposium on Snow Mechanics, Grindelwald, Switzerland, April 1–4, 1974*. IAHS-AISH Publication 114, p. 251–291.
- Meschke, G., C. Liu, and H.A. Mang** (1996) Large strain finite-element analysis of snow. *Journal of Engineering Mechanics*, July: 581–591.
- Mousseau, C.W., and G. M. Hulbert** (1996) An efficient tire model for the analysis of spindle forces produced by a tire impacting large obstacles. *Computer Methods in Applied Mechanics and Engineering*, **135**(1-2): 15–34.
- Mundl, R., G. Meschke, and W. Liederer** (1997) Friction mechanism of tread blocks on snow surfaces. *Tire Science and Technology*, **25**(4): 245–264.
- Pi, W.S.** (1988) Dynamic tire/soil contact surface interaction model for aircraft ground operations. *Journal of Aircraft*, **25**(11): 1038–1044.
- Padovan, J.** (1977) On standing waves in “tires.” *Tire Science and Technology*, **5**(2): 83–101.

- Padovan, J., and P. Padovan** (1993) Spinup wear in aircraft “tyres.” *Tire Science and Technology*, **21**(3): 138–162.
- Padovan, J. and P. Padovan** (1994a) Modelling wear at intermittently slipping high speed interfaces. *Computers and Structures*, **52**(4): 795–812.
- Padovan, J., and P. Padovan** (1994b) Modelling “tyre” performance during antilock braking. *Tire Science and Technology*, **22**(3): 182–204.
- Padovan, J., A. Kazempour, F. Tabaddor, and B. Brockman** (1992) Alternative formulations of rolling contact problems. *Finite Elements in Analysis and Design*, **11**(4): 275–284.
- Peters, J.F.** (1991) Computational aspects of endochronic plasticity. In *Proceedings, 7th International Conference on Computer Methods and Advances in Geomechanics*, Cairns, Australia.
- Pi, W.S.** (1988) Dynamic tire/soil contact surface interaction model for aircraft ground operations. *Journal of Aircraft*, **25**(11): 1038–1044.
- Richmond, P.W.** (1995) Motion resistance of wheeled vehicles in snow. CRREL Report 95-7, U.S. Army Cold Regions Research and Engineering Laboratory, Hanover, NH.
- Richmond, P.W., S.A. Shoop, and G.L. Blaisdell** (1995) Cold regions mobility models. CRREL Report 95-7, U.S. Army Cold Regions Research and Engineering Laboratory, Hanover, NH.
- SAE (Society of Automotive Engineers)** (1992) *SAE Glossary of Automotive Terms*. Warrendale, Pennsylvania: Society of Automotive Engineers.
- Saliba, J.E.** (1990) Elastic-viscoplastic finite-element program for modeling tire-soil interaction. *Journal of Aircraft*, **27**(4): 350–357.
- Schmid, I.C.** (1995) Interaction of vehicle and terrain: Results from 10 years research at IKK. *Journal of Terramechanics*, **32**(1): 3–26.
- Schofield, A.N., and C.P. Wroth** (1968) *Critical State Soil Mechanics*. London: McGraw-Hill.
- Scott, R.F.** (1985) Plasticity and constitutive relations in soil mechanics. *Journal of Geotechnical Engineering*, **11**(5): 563–605.
- Shapiro, L., J. Johnson, M. Sturm, and G. Blaisdell** (1997) Snow mechanics: Review of the state of knowledge and applications. CRREL Report 97-3, U.S. Army Cold Regions Research and Engineering Laboratory, Hanover, NH.
- Shen, J., and R.L. Kushwaha** (1998) *Soil-Machine Interactions*. New York: Marcel Dekker, Inc.
- Shoop, S.A.** (1990) Mechanisms controlling vehicle mobility on a thawing soil. In *Proceedings of the 10th International Conference of the International Society of Terrain Vehicle Systems, Kobe, Japan, August 1990*, vol. I, p. 301–312.
- Shoop, S.A.** (1993) Thawing soil strength measurements for predicting vehicle performance. *Journal of Terramechanics*, **30**(6): 405–418.
- Shoop, S., and R. Alger** (1998) Snow deformation beneath a vertically loaded plate. In *Proceedings, ASCE Cold Regions Specialty Conference, Duluth, Minnesota, September 1998*.
- Shoop, S., B. Young, R. Alger, and J. Davis** (1994) Winter traction testing. *Automotive Engineering*, **102**(1): 75-78, SAE paper 940110.
- Shoop, S.A., R. Haehnel, K. Kestler, K. Stebbings, and R. Alger** (1999) Finite element analysis of a wheel rolling in snow. In *Proceedings of the 10th International Conference on Cold Regions Engineering, Lincoln, New Hampshire, August, 1999*, p. 519–530.
- Smith, D.M.** (2000) Response of granular layers in flexible pavements subjected to aircraft loading. ERDC/GL TR-00-3, U.S. Army Corps of Engineers, Engineer Research and Development Center, Vicksburg, MS.
- Timoshenko, S.P., and J.N Goodier** (1970) *Theory of Elasticity*. New York: McGraw-Hill Book Company, Third Edition.
- Tordesillas, A.** (1996) A contact mechanics approach to the soil-tire interaction problem. In *Proceedings, Second North American Workshop on Modeling the Mechanics of Off-Road Mobility, Vicksburg, Mississippi*.
- Wong, J.Y.** (1989) *Terramechanics and Off-Road Vehicles*. New York: Elsevier.
- Wong, J.R., and A.R. Reece** (1966) Soil failure beneath rigid wheels. In *Proceedings, 2nd International Conference of the International Society for Terrain-Vehicle Systems*, p. 425–445.
- Wong, J.R., and A.R. Reece** (1967) Prediction of rigid wheel performance based on the analysis of soil-wheel stresses. *Journal of Terramechanics*, **4**(2): 7–25.
- Wood, D.M.** (1990) *Soil Behavior and Critical State Soil Mechanics*. New York: Cambridge University Press.
- Yong, R.N., and E.A. Fattah** (1976) Prediction of wheel-soil interaction and performance using finite element method. *Journal of Terramechanics*, **13**(4): 227–240.
- Yong, R.N., E.A. Fattah, and P. Boosinsuk** (1978) Analysis and prediction of tyre-soil interaction and performance using finite elements. *Journal of Terramechanics*, **15**(1): 43–63.
- Yong, R.N., E.Z. Fattah and N. Skiadas** (1984) *Vehicle Terrain Mechanics*. New York: Elsevier.

REPORT DOCUMENTATION PAGE				Form Approved OMB No. 0704-0188	
Public reporting burden for this collection of information is estimated to average 1 hour per response, including the time for reviewing instructions, searching existing data sources, gathering and maintaining the data needed, and completing and reviewing this collection of information. Send comments regarding this burden estimate or any other aspect of this collection of information, including suggestions for reducing this burden to Department of Defense, Washington Headquarters Services, Directorate for Information Operations and Reports (0704-0188), 1215 Jefferson Davis Highway, Suite 1204, Arlington, VA 22202-4302. Respondents should be aware that notwithstanding any other provision of law, no person shall be subject to any penalty for failing to comply with a collection of information if it does not display a currently valid OMB control number. PLEASE DO NOT RETURN YOUR FORM TO THE ABOVE ADDRESS.					
1. REPORT DATE (DD-MM-YY) November 2001		2. REPORT TYPE Technical Report		3. DATES COVERED (From - To)	
4. TITLE AND SUBTITLE Finite Element Modeling of Tire-Terrain Interaction				5a. CONTRACT NUMBER	
				5b. GRANT NUMBER	
				5c. PROGRAM ELEMENT NUMBER	
6. AUTHOR(S) Sally A. Shoop				5d. PROJECT NUMBER	
				5e. TASK NUMBER	
				5f. WORK UNIT NUMBER	
7. PERFORMING ORGANIZATION NAME(S) AND ADDRESS(ES) U.S. Army Engineer Research and Development Center Cold Regions Research and Engineering Laboratory 72 Lyme Road Hanover, NH 03755-1290				8. PERFORMING ORGANIZATION REPORT NUMBER ERDC/CRREL TR-01-16	
9. SPONSORING/MONITORING AGENCY NAME(S) AND ADDRESS(ES) Office of the Chief of Engineers Washington, D.C. 20314-1000				10. SPONSOR / MONITOR'S ACRONYM(S)	
				11. SPONSOR / MONITOR'S REPORT NUMBER(S)	
12. DISTRIBUTION / AVAILABILITY STATEMENT Approved for public release; distribution is unlimited. Available from NTIS, Springfield, Virginia 22161.					
13. SUPPLEMENTARY NOTES					
14. ABSTRACT The desire to incorporate theoretical mechanics into off-road vehicle performance prediction has generated great interest in applying numerical modeling techniques to simulate the interaction of the tire and terrain. Therefore, a full three-dimensional model simulating a tire rolling over deformable terrain was developed. Tires were simulated using a rigid wheel, a deformable tire simplified with user-defined sidewall elements, and modal analysis tire models. Model comparisons with measured, hard-surface tire deformation and contact stress showed very good agreement. The simplified tire model was much more computationally efficient but the modal analysis model yielded better contact stress distribution. Each of the tire models was then combined with rolling on deformable terrain. Fresh snow and compacted sand surfaces were modeled using critical-state plasticity models. The rigid wheel model was validated on snow using field measurements of tire forces and snow deformation and then compared to performance predictions using the NATO Reference Mobility Model. These comparisons indicate excellent agreement between the model and the measurements. Preliminary results of the modal analysis tire model on snow show very little deformation in the tire, indicating that the rigid wheel simplification may be a good approximation for soft terrain.					
15. SUBJECT TERMS Mobility Tires Tire modeling					
16. SECURITY CLASSIFICATION OF:			17. LIMITATION OF OF ABSTRACT	18. NUMBER OF PAGES	19a. NAME OF RESPONSIBLE PERSON
a. REPORT	b. ABSTRACT	c. THIS PAGE			19b. TELEPHONE NUMBER (include area code)
U	U	U	U	70	